AIX-MARSEILLE UNIVERSITÉ
UNIVERSITY OF SYDNEY
ECOLE DOCTORALE 352

INSTITUT FRESNEL/CLARTE

Thèse présentée pour obtenir le grade universitaire de docteur

Discipline: PHYSIQUE ET SCIENCES DE LA MATIERE
Spécialité: Optique, Photonique et Traitement d'Image

Kaizad RUSTOMJI

Controlling spontaneous emission and resonance energy transfer: An antenna analogy.

Contrôle de l'émission spontanée et transfert d'énergie par résonance : Antenne analogie.

Soutenue le 26/01/2018 devant le jury composé de:

Femius KOENDERINK	FOM Instituut AMOLF	Rapporteur
Jean-Jacques GREFFET	l'Institut d'Optique	Rapporteur
Julien DE ROSNY	Institut Langevin	Examinateur
C. Martijn DE STERKE	University of Sydney	Examinateur
Redha ABDEDDAIM	Institut Fresnel	Examinateur
Stefan ENOCH	Institut Fresnel	Directeur de thèse

Numéro national de thèse/suffixe local: 2017AIXM0001/001ED62

Résumé en Français

L'émission spontanée ou encore le transfert d'énergie par résonance de type Förster sont des processus généralement attribués aux atomes et aux molécules. On sait maintenant que dans le régime de couplage faible, la modification du taux d'émission spontanée, caractérisée par le facteur de Purcell, est analogue à la modification de l'impédance d'une antenne sub-longueur d'onde. Nous utilisons de telles analogies basées sur les impédances d'antennes pour étudier le facteur de Purcell et le transfert d'énergie de résonance théoriquement et expérimentalement, aux fréquences micro-ondes.

L'avantage de l'utilisation d'antennes est qu'elles permettent naturellement un contrôle précis de la localisation de l'émetteur et de l'orientation de son moment dipolaire. De ce point de vue, les expériences micro-ondes possèdent un atout important par rapport aux expériences optiques. De plus, pour les longueurs d'onde optiques, les expériences sont généralement réalisées en utilisant un ensemble de molécules fluorescentes, qui offrent un contrôle limité sur la position et l'orientation du moment dipolaire des émetteurs.

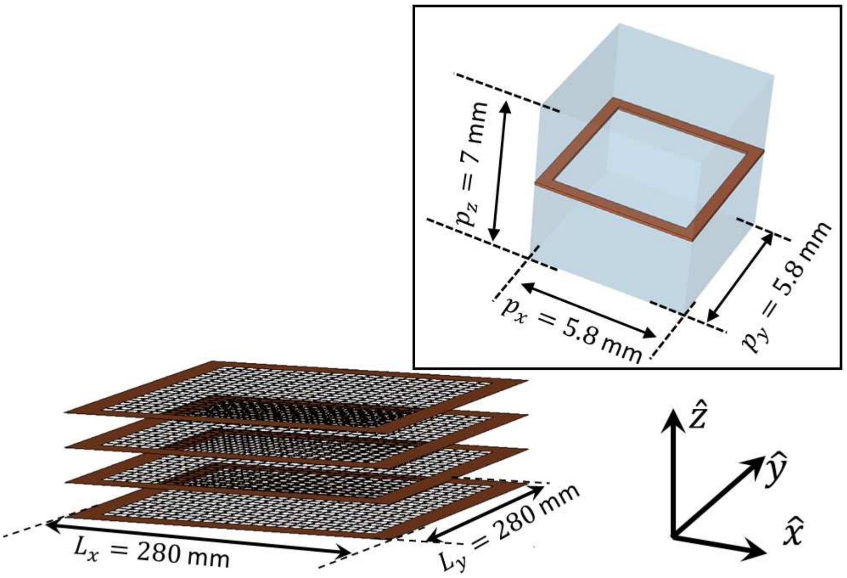

Figure A: Le métamatériau utilisé pour l'étude est composée de 4 couches de grilles de cuivre de 0,1 mm d'épaisseur dans le plan empilé dans la direction $\hat{z}$. (Encart) Cellule unitaire du métamatériau.

Dans la première partie de la thèse, nous nous concentrons sur l'émission spontanée et le facteur Purcell. Le taux d'émission spontanée est déterminé par la densité locale des états, qui peut à son tour être exprimée en utilisant la fonction de Green qui est une grandeur électromagnétique classique. L'impédance d'un dipôle ponctuel est proportionnelle à la fonction de Green à son origine, ainsi celle d'une antenne dipôle courte, permet d'accéder à l'étude de la modification de l'émission spontanée et donc du facteur de Purcell.

Nous appliquons la méthode de mesure de l'impédance d'antenne pour étudier le facteur Purcell électrique et magnétique dans un métamatériau hyperbolique, comme le montre la figure A, dans la gamme de fréquences micro-ondes 5-15 GHz. Le métamatériau, en raison de sa dispersion hyperbolique dans la polarisation TM $_z$, a une densité d'états locale importante qui conduit à une augmentation du facteur Purcell. Dans le même temps, l'absence de modes de propagation dans la polarisation TE $_z$ diminue le facteur Purcell. Nous démontrons expérimentalement qu'il est possible de mesurer ce facteur Purcell dépendant de la polarisation aux fréquences micro-ondes en utilisant des antennes dipôles. En mesurant le facteur de Purcell pour différentes orientations d'antennes, nous obtenons une compréhension du rôle des modes individuels de la structure et de leur contribution à la densité d'états. Nous montrons que la méthode de mesure d'impédance pour déterminer le facteur Purcell magnétique avec une antenne à boucle dipolaire magnétique doit être utilisée avec précaution. En effet, la méthode n'est pas fiable près de la fréquence anti-résonance de l'antenne, et peut conduire à une interprétation erronée des résultats.

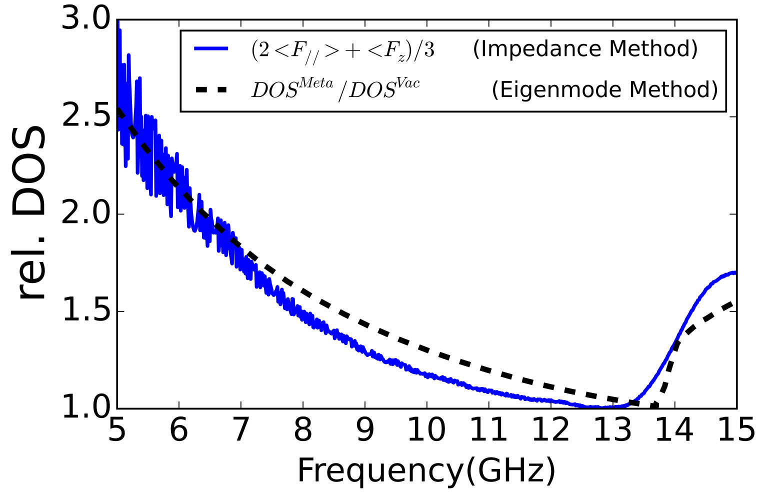

Figure B: Comparaison de $rel.DOS$ obtenu à partir de la méthode de mesure d'impédance (blue) et de $rel.DOS$ à partir des calculs de mode propre (en pointillés).

Afin de valider nos calculs et mesures, nous montrons également sur des résultats numériques que la moyenne spatiale du calcul de la densité locale d'états obtenue ainsi est identique au calcul de densité d'états pour une structure périodique (donc infinie) obtenue grâce au calcul des modes de Bloch à condition de filtrer les résonances de type Fabry-Perot (Fig. B).

Dans la seconde partie de la thèse, nous développons l'analogie d'impédance d'antenne pour étudier le transfert d'énergie de résonance. Le transfert d'énergie de résonance est le processus d'échange d'excitation d'un atome dans un état excité (donneur) à un atome dans un état fondamental (accepteur). Ce régime d'interaction est particulièrement intéressant lorsque la distance de séparation donneur-accepteur est inférieure à la longueur d'onde. À de telles distances, le transfert d'énergie est dû à des mécanismes non radiatifs à champ proche. Un tel transfert d'excitation gouverne des phénomènes importants tels que le transfert d'énergie par résonance de type Förster (FRET), responsable du transfert d'énergie entre molécules à des distances nanométriques.

Alors que les méthodes basées sur l'impédance d'antenne ont été développées précédemment pour la mesure du facteur Purcell, elles n'ont pas été appliquées pour étudier le transfert d'énergie par résonance. Nous développons donc dans un premier temps la théorie puis comparons les prédictions théoriques avec des expériences. En étudiant l'émission spontanée et la densité locale d'états, nous ne considérons par définition que l'effet des modes qui rayonnent vers le champ lointain (pour un système sans perte). Cependant, dans le transfert d'énergie de résonance, en fonction de la distance de séparation r_{DA} entre le dipôle donneur et accepteur, les modes champ proche, non radiatif, participent également à l'échange de l'énergie.

Nous mesurons le transfert d'énergie par résonance avec deux antennes de taille finie tout en faisant varier la distance de séparation r_{DA} entre les deux antennes. Les expériences sont réalisées dans l'orientation transversale et longitudinale des antennes à 1 GHz (Fig. C). La puissance transférée entre les antennes, s'échelonne comme r_{DA}^{-6} dans le champ proche, ce qui est caractéristique de FRET.

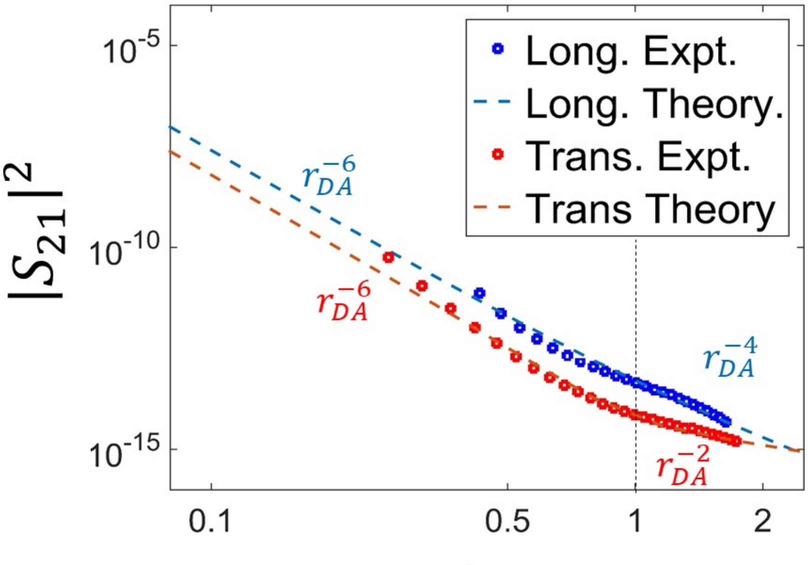

Figure C: Mesures (points) de $|S_{21}|^2$ en fonction de la séparation r_{DA} entre les antennes, par rapport à la fonction théorique Green (tirets) dans le vide. Pour l'orientation transversale (rouge) et l'orientation longitudinale (bleu) à la fréquence 1 GHz ($\lambda = 300$ mm).

Nous mesurons ensuite la modification du transfert d'énergie par résonance dans une cavité plane constituée de deux plaques parallèles métalliques (Fig. D). Dans ce cas, les positions relatives des antennes donneur et accepteur sont fixes, et les modes sont changés en faisant varier l'écart L entre les plaques de la cavité. Nous montrons que les résultats de mesure sont en bon accord avec ceux prédits par la théorie analytique et avec les simulations FDTD.

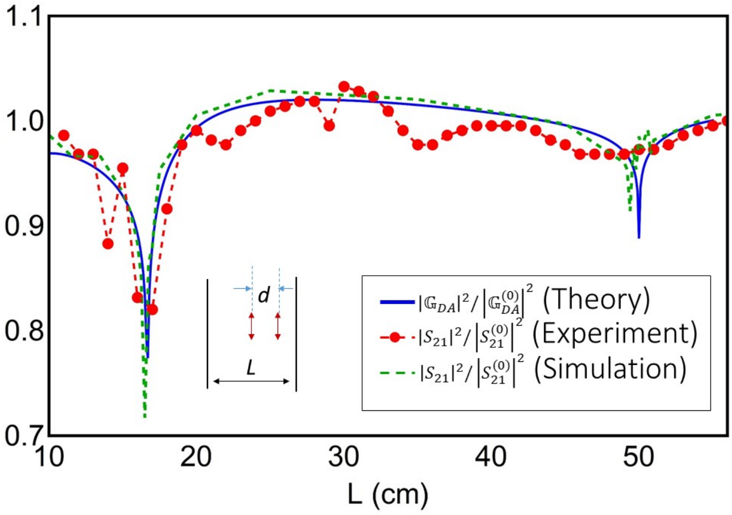

Figure D: Comparaison du taux de transfert d'énergie par résonance entre deux dipôles à l'intérieur d'un guide d'onde à plaques parallèles en fonction de la largeur de la cavité (L). (Bleu, solide) à partir de la fonction théorique de Green, (rouge) des mesures de l'impédance d'antenne et des simulations FDTD (vertes). La longueur de l'antenne est de 10 mm avec $lambda = 33,33$ cm, $d = 1,8$ cm.

Pour le transfert d'énergie par résonance, les mesures micro-ondes présentent un avantage fondamental par rapport aux techniques de mesure optique. Dans les expériences FRET à des longueurs d'onde optiques faites avec des molécules fluorescentes, l'énergie transférée du donneur à l'accepteur est déterminée par des mesures indirectes de changements d'intensité ou de durée de vie des molécules fluorescentes. Aucune des techniques aux longueurs d'onde optiques ne peut mesurer directement le transfert d'énergie car le FRET est un processus « sombre » faisant intervenir le champ proche, médié par des photons virtuels. En revanche, dans les expériences micro-ondes comme les antennes sont alimentées par des câbles coaxiaux, une mesure directe du transfert d'énergie est possible.

Nous montrons, le facteur le plus crucial dans les expériences de transfert d'énergie de résonance avec des antennes est leur taille. Comme la puissance transférée entre les dipôles s'échelonne comme r_{DA}^{-6} dans le champ proche, il est essentiel que les longueurs d'antenne soient de dimension fortement sous-longueur d'onde, pour éviter les effets de longueur finie. Cependant, diminuer la taille des antennes diminue la quantité de puissance qu'elles peuvent émettre et absorber. Par conséquent, il est important de choisir judicieusement une longueur d'antenne appropriée qui concilie la demande pour le niveau de précision souhaité avec la capacité de mesure des expériences.

Cette thèse présente un cadre simple pour caractériser l'influence de l'environnement électromagnétique sur l'émission spontanée et le transfert d'énergie de résonance, avec des antennes. Il contribuera à développer une compréhension cohérente de l'effet de l'environnement électromagnétique sur les processus induits par les interactions dipolaires atome-champ.

Résumé

L'émission spontanée est due à l'interaction entre un atome et un champ électromagnétique. Ainsi, cet effet n'est pas une caractéristique intrinsèque des atomes et l'émission spontanée est fortement dépendante de l'environnement électromagnétique dans lequel ils évoluent. Par conséquent, en contrôlant la densité locale d'états électromagnétiques (LDOS), il est possible d'augmenter ou de diminuer le taux d'émission spontanée. Le facteur de Purcell mesure l'augmentation ou la diminution du taux d'émission spontanée. Le but de cette thèse est d'analyser l'effet des modes électromagnétiques sur le ce facteur. Le plus souvent, la mesure du facteur Purcell se fait via la variation des taux de décroissance des atomes ou des molécules fluorescentes. Récemment, il a été démontré que dans un régime de couplage faible, le facteur Purcell est analogue à la modification de l'impédance d'entrée d'une antenne radiofréquence. Cette démonstration a permis d'étendre la quantification du facteur de Purcell au domaine des hyperfréquences.

Dans cette thèse, nous avons utilisé cette approche de mesure de l'impédance d'antenne afin de déterminer le facteur de Purcell électrique et magnétique dans un métamatériau fonctionnant entre 5-15 GHz. Le métamatériau, en raison de sa dispersion hyperbolique en polarisation transverse magnétique a une densité d'états locale importante qui se traduit par une augmentation du facteur Purcell. En même temps, l'absence de modes de propagation dans la polarisation transverse électrique annule le facteur Purcell. Nous avons démontré expérimentalement, il est possible d'étudier cette dépendance en polarisation en utilisant de simples antennes radiofréquences.

Dans la deuxième partie de la thèse, j'ai étendu ce modèle à la caractérisation de la modification du transfert d'énergie dans les interactions dipôle-dipôle (DDI) par l'environnement électromagnétique. Le transfert d'énergie par résonance (Förster resonance energy transfer, FRET) est le processus d'échange d'excitation entre un atome dans un état excité (donneur) et un atome dans un état fondamental (accepteur). Ces interactions sont particulièrement intéressantes lorsque la distance séparant le donneur et l'accepteur est inférieure à la longueur d'onde. À de telles distances, le transfert d'énergie est dû à des mécanismes non radiatifs en champ proche. Un tel transfert d'excitation gouverne des phénomènes importants tels que le transfert d'énergie par résonance, responsable du transfert d'énergie entre les molécules à des distances nanométriques (nm).

Dans le manuscrit, je montre que pour l'émission spontanée, on peut formuler un transfert d'énergie classique avec des antennes radiofréquences. Le transfert d'énergie par résonance peut être ainsi étudié à travers l'impédance mutuelle (Z_{21}) de deux circuits linéaires couplés à des antennes de dimensions sub-longueur d'onde. Je développe ainsi des analogies classiques afin de caractériser l'influence des modes électromagnétiques sur les processus par DDI tel que le FRET en termes d'impédance mutuelle (Z_{21}) d'un réseau micro-ondes à deux ports. Je présente ensuite les mesures du transfert d'énergie de résonance dans le vide à la fréquence 1 GHz où la dépendance caractéristique du FRET comme r_{DA}^{-6} est rapportée, r_{DA} étant la distance de séparation donneur-accepteur. Je présente aussi des résultats expérimentaux montrant le changement de transfert d'énergie de résonance à l'intérieur d'un guide d'onde à plaques parallèles et je le compare avec les modèles théoriques. Ainsi, ce travail contribue à développer une compréhension cohérente de l'effet de l'environnement électromagnétique sur processus induits par les interactions dipolaires atome-champ.

Abstract

Spontaneous emission arises due to the interaction of the atom with the electromagnetic field. Hence, it is not completely intrinsic to the atom, but also depends on its electromagnetic environment. By controlling the local density of states (LDOS) it is possible to enhance or decrease the rate of spontaneous emission. The figure of merit for enhancement or decrease in the spontaneous emission rate is the Purcell factor. In this thesis we analyze the effect of the electromagnetic modes on the Purcell factor. Conventional experiments to measure the Purcell factor involve characterizing the change in decay rates of atoms or fluorescent molecules. Recent research has shown that in the weak-coupling regime, Purcell factor is analogous to the modification of antenna impedance. The ability to probe the Purcell factor with antennas, expands the scope of measurements from optical frequencies to microwave frequencies.

In this thesis we have used this antenna impedance approach to measure the electric and magnetic Purcell factor for a fishnet metamaterial structure designed for operation in the microwave frequency range 5-15 GHz. The metamaterial, due to its hyperbolic dispersion in the TM_z polarization, has a large local density of states which enhances the Purcell factor. At the same time, lack of propagating modes in the TE_z polarization suppresses the Purcell factor. We demonstrate experimentally, that it is possible to resolve this polarization dependent Purcell factor at microwave frequencies using antennas.

In the second part of the thesis, we focus on how the electromagnetic modes modify resonance energy transfer mediated by dipole-dipole interactions (DDI). Resonance energy transfer is the process of exchange of excitation from an atom in an excited state (donor) to an atom in a ground state (acceptor). Of particular interest is the regime when the donor-acceptor separation distance is subwavelength. At such distances the energy transfer is due to near-field, non-radiative mechanisms. Such transfer of excitation governs important phenomena such as Förster resonance energy transfer (FRET), responsible for energy transfer between molecules at nanometer distances.

We show that, as for spontaneous emission, a classical analogue to resonance energy transfer with antennas can be formulated. We demonstrate that resonance energy transfer can be studied through the mutual impedance (Z_{21}) of two linear circuits coupled with subwavelength antennas. We develop classical analogues to characterize the influence of electromagnetic modes on processes mediated by DDI like FRET in terms of the mutual impedance (Z_{21}) of a two-port microwave network. I measure resonance energy transfer in vacuum at the frequency 1 GHz where the characteristic FRET like r_{DA}^{-6} dependence is reported, r_{DA} being the donor-acceptor separation distance. We measure the change in resonance energy transfer inside a parallel plate waveguide and compare with theoretical predictions. This work will contribute towards developing a coherent understanding the effect of the electromagnetic environment on processes mediated by dipolar atom-field interactions.

Acknowledgements

First of all I would like to thank my supervisors, Stefan Enoch, Redha Abdeddaim, Martijn de Sterke, and Boris Kuhlmey for their constant encouragement and guidance over the course of my PhD. I thank them for teaching me various concepts about metamaterials, microwave experiments, terahertz experiments, and local density of states which would have otherwise been inaccessible to me. I have also greatly benefitted from collaborating with Alessio Stefani, Marc Dubois, Sébastien Guenneau, Gérard Tayeb, Jérome Wenger, and John Sipe. It has been a pleasure working with all of you.

I have enjoyed interactions, scientific and non-scientific, with several colleagues, both at Institut Fresnel and University of Sydney. Special thanks to my friend, colleague, and officemate Rémi Colom. Finally, I would like to thank my family for their unwavering support in all my endeavours.

This research was conducted within the context of the International Associated Laboratory "ALPhFA: Associated Laboratory for Photonics between France and Australia". This work was carried out thanks to the support of the A*MIDEX project (n° ANR-11-IDEX-0001-02) funded by the Investissements d'Avenir French Government program, managed by the French National Research Agency (ANR). This work was supported by the Australian Research Council (CUDOS Centre of Excellence CE110001018).

Contents

Acknowledgements **7**

1 Introduction **17**

1.1 Spontaneous emission 18

1.1.1 Applications of engineering LDOS 21

1.1.2 Classical analogue to modification of spontaneous emission 22

1.2 Resonance energy transfer. 24

1.2.1 Förster resonance energy transfer 25

1.2.2 Applications of FRET 28

1.2.3 Classical analogue to resonance energy transfer 29

1.2.4 Advantages of studying resonance energy transfer with antennas . 30

1.3 Hyperbolic metamaterials 31

1.3.1 Introduction to hyperbolic metamaterials 31

1.3.2 LDOS in hyperbolic metamaterials 33

1.4 Thesis outline 34

2 Spontaneous emission **37**

2.1 Maxwell's equations 38

2.2 Green function for electromagnetic wave equation 39

2.3 Orthogonal modes and Green function 40

2.4 Quantum mechanical theory of spontaneous emission. 41

2.4.1 Local density of states and Green function 43

2.5 Purcell factor 45

2.6 Classical theory of radiation 46

2.7 Antenna impedance and Purcell factor. 47

2.7.1 Impedance of a subwavelength dipole antenna. 49

2.8 Equivalent circuit model for Purcell effect. 51
2.9 Electric and magnetic Purcell factor. 52
2.10 Theory of microwave measurements. 53
  2.10.1 One port network 53
  2.10.2 Antenna as a one-port network. 55
  2.10.3 Two port network 55
  2.10.4 Scattering parameters (S-parameters) 57
2.11 Example: Purcell factor near a conducting interface 58

3 Purcell factor in a microwave fishnet hyperbolic metamaterial 63
3.1 Microwave fishnet metamaterial structure 64
3.2 Numerical modelling for density of states calculation 66
3.3 Density of states calculation from iso-frequency surfaces 68
3.4 Experiments 70
  3.4.1 Measurement of the Purcell factor with antenna impedance . . . 70
3.5 Results and discussion 73
  3.5.1 Purcell factor for magnetic dipole oriented along $\hat{z}$ 73
  3.5.2 Purcell factor for electric dipole oriented along $\hat{y}$ 75
  3.5.3 Purcell factor for electric dipole oriented along $\hat{z}$ 77
  3.5.4 Comparison of the DOS from eigenmode calculations and impedance of antennas 78

4 Resonance energy transfer 81
4.1 Quantum electrodynamical formulation of resonance energy transfer . . 82
4.2 Classical dipole-dipole interaction. 84
4.3 Antenna model for resonance energy transfer 86
4.4 Resonance energy transfer measurement at microwave frequencies 90
  4.4.1 Difference from antenna based Purcell factor measurements 90

5 Resonance energy transfer measurements at microwave frequencies 93
5.1 Resonance energy transfer in vacuum 93
  5.1.1 Experiments 93
  5.1.2 Finite dipole antenna length 94
5.2 Resonance energy transfer in parallel plate cavity 98

6 Conclusion 103

A LDOS in a parallel plate cavity. 107

B Strong coupling. 109

C Mimicking electromagnetic wave coupling in tokamak plasma with fishnet metamaterials 111

List of Figures

1.1 Number of atoms in the excited state, also exiting the cavity in their excited state, inside and outside the cut-off regime of a parallel plate waveguide. (Source: Hulet et al [9]) 20

1.2 Power emitted by dipole antenna in a parallel plate cavity (dots) compared with the LDOS (solid) at 1 GHz as a function of the separation between plates. (Source: Dowling [27]) 23

1.3 Schematic of resonance energy transfer in a donor acceptor system. Left: classical; right: quantum mechanical manifestation. (Source: Novotny and Hecht [5]). 25

1.4 Iso-frequency surfaces for two close frequencies in a hyperbolic metamaterial (blue) compared with iso-frequency surfaces of an isotropic medium (red). 33

2.1 (a) Schematic of a dipole antenna, (b) equivalent circuit of dipole antenna attached to a coaxial cable of impedance Z_w. 48

2.2 Schematic of a subwavelength dipole antenna with a load impedance Z_L. 49

2.3 (a) Schematic of a dipole antenna near an object, (b) equivalent circuit model of harmonic dipole in presence of an object. 51

2.4 Schematic of a one port network. 54

2.5 Schematic of a two port network in current and voltage representation. . 56

2.6 Two port network in S-parameter representation. 57

2.7 Modification of lifetimes of fluorescent molecules near a conducting mirror. (Source: Drexhage [7]) 59

2.8 Purcell factor near a conducting plate at microwave frequencies for perpendicular (red) and parallel (blue) orientations of the antenna. (Source: Krasnok et al, [33]) 60

3.1 Fishnet metamaterial structure used for study is composed of 4 layers of 0.1 mm thick copper grids in the plane stacked in $\hat{z}$ direction. (Inset) Unit cell of the metamaterial structure. 64

3.2 Band diagram of the metamaterial unit cell in (Fig. 3.1) along the path $\Gamma(k_x = 0, k_z = 0) - X(k_x = \pi/p_x, k_z = 0) - K(k_x = \pi/p_x, k_z = \pi/p_z) - M(k_x = 0, k_z = \pi/p_z) - \Gamma(k_x = 0, k_z = 0)$. 67

3.3 Isofrequency surfaces for the unit cell in (Fig. 3.1) (a), (b), (c) show isofrequency surfaces for modes 1, 2 and 3 respectively as marked in Fig. 3.2. The topology of isofrequency surfaces for mode 1 (a) is hyperbolic and leads to a high density of states. Mode 2 (b), mode 3 (c) begin at 13.6 GHz, at the plasma frequency ω_p. The Brillouin zone sectioned by the plane $k_y = 0$. 68

3.4 Illustration of the method used to compute the density of states. The isofrequency surface, $\omega(k_x, k_y, k_z)$ is divided into N triangles; the gradient $\vec{\nabla}\omega_k$ is computed at the centroids of the triangular patches and used in (Eq. 3.3) to compute the density of states. 69

3.5 Density of states computed with the iso-frequency surfaces for mode 1 (blue), mode 2 (red) and mode 3 (green) as shown in (Fig. 3.3) and compared with the theoretical density of states for vacuum (dashed). The first mode due to hyperbolic isofrequency surfaces has higher DOS than vacuum. 70

3.6 Input and output time signals from FDTD simulations for an electric dipole along $\hat{z}$ placed at the center of the structure. The first reflection in the output signal occurs around 0.9 ns which corresponds to the time taken by the wave to reflect back from the boundary of the structure. 72

3.7 The Purcell factor for an electric dipole along $\hat{z}$ computed from the time signals in Fig. 3.7. Solid curves are calculated from time signals up to 30 ns; dashed curves give the corresponding results after time windowing to eliminate the effect of the reflections from the boundaries. 72

3.8 Real (red) and imaginary (blue) parts of scattering coefficient S_{11} from simulations (solid) and measurements (dashed), (a) in free space, (b) in metamaterial with magnetic loop dipole antenna oriented along $\hat{z}$. 73

3.9 Measurement and simulation of magnetic Purcell factor for a magnetic dipole oriented along $\hat{z}$, inside the metamaterial structure. 74

3.10 Comparison of FDTD simulations (blue) and theoretical calculations (black, dashed) of input impedance $\mathrm{Re}(Z_{in})$ of a magnetic dipole antenna in vacuum with outer radius $b = 3$ mm and wire radius $a = 1$ mm. 75

3.11 Real (red) and imaginary (blue) parts of scattering coefficient S_{11} from simulations (solid) and measurements (dashed), (a) in free space, (b) in metamaterial with electric dipole antenna oriented along $\hat{y}$. 75

3.12 Measurement and simulation of electric Purcell factor for an electric dipole oriented along $\hat{y}$, inside the metamaterial structure. 76

3.13 Real (red) and imaginary (blue) parts of scattering coefficient S_{11} from simulations (solid) and measurements (dashed), (a) in free space, (b) in metamaterial with electric dipole antenna oriented along $\hat{z}$. 77

3.14 Measurement and simulation of electric Purcell factor for an electric dipole oriented along $\hat{z}$, inside the metamaterial structure. 78

3.15 Comparison of the $rel.DOS$ obtained from impedance method (blue) and $rel.DOS$ from eigenmode calculations (dashed) as shown in (Fig. 3.5). . . 79

4.1 Resonance energy transfer between a classical dipole donor acceptor pair. 84

4.2 The two port network demonstrating a donor and an acceptor system . . 86

4.3 Dipole dipole interaction with subwavelength antennas. 88

4.4 Setup for measurement of energy transfer between two dipoles at microwave frequencies with antennas. 90

5.1 Schematic of resonance energy transfer experimental setup, illustrating the transverse and longitudinal orientation of dipole antennas. 94

5.2 Comparison of finite antenna lengths for resonance energy transfer. . . . 94

5.3 Experimental setup for resonance energy transfer measurement in free space, showing the copper dipole antennas attached to coaxial cables, in the transverse orientation. 96

5.4 Measurements (dotted) of $|S_{21}|^2$ as a function of separation r_{DA} between the antennas, compared with theoretical Green function (dashed) in vacuum. For transverse orientation (red) and longitudinal orientation (blue) at frequency 1 GHz (λ=300 mm). 97
5.5 Schematic of setup to measure the influence of electromagnetic modes on resonance energy transfer. 99
5.6 Comparison of resonance energy transfer rate between two dipoles inside a parallel plate waveguide as a function of the cavity width (L) as shown in Fig. 5.5. (Blue, solid) from theoretical Green function, (red) from antenna measurements, and (green) FDTD simulations. The antenna length is 10 mm with $\lambda = 33.33$ cm, $d = 1.8$ cm, and $x = 0.1$ cm. 100

A.1 The spontaneous emission in a parallel plate waveguide as seen in Fig. (5.5) normalised to vacuum as a function of the distance between the plates L. The emitter is located at the center of the waveguide oriented along $\hat{x}$ at $z = L/2$. The wavelength is taken to be $\lambda = 33.33$ cm. 107

B.1 Phase of scattering coefficient S_{11} for the magnetic loop antenna used for Purcell factor measurements in Sec. 3.5.1. In vacuum (orange) and in the metamaterial (blue). 110

Chapter 1

Introduction

This thesis is about examining how the electromagnetic environment influences two processes, spontaneous emission and resonance energy transfer. Spontaneous emission is responsible for the majority of radiation we experience in day-to-day life. It is responsible for the light from the sun, the heat from a fire, and the display of a screen. Spontaneous emission is the process through which an atom in a high energy excited state, spontaneously de-excites to a lower energy ground state while emitting a photon. The energy of the emitted photon is determined by the separation between the two energy levels.

While in spontaneous emission the energy is emitted into the environment, in resonance energy transfer the energy is transferred from one atom to another. Resonance energy transfer is the exchange of excitation between two atoms or molecules. During the process the excited state atom (donor), transfers its energy to the atom that is initially in the ground state (acceptor). The donor atom relaxes to its ground state, while the acceptor gains energy into its excited state.

For a long time it was assumed that spontaneous emission is an inherent property of the emitter. It was discovered later that although some aspects of spontaneous emission depend upon the emitter, spontaneous emission is also modified by the environment in which the emitter is located [1]. Similarly, it is now understood that resonance energy transfer is also affected by the environment of the participating donor-acceptor pair [2].

Instead of focusing directly on quantum mechanical emitters such as atoms or fluorescent molecules, we shall use classical analogues to spontaneous emission and resonance energy transfer to characterize the effect of the environment. In the semi-classical approximation, the effect on the spontaneous emission rate of an atom is similar to the effect on the power radiated by a classical dipoles (infinitesimally small, harmonically oscillating dipole). Similarly the effect on the resonance energy transfer is similar to the effect on the power transferred between two classical dipoles. This analogy is developed further and allows measurements of the influence on spontaneous emission and resonance energy transfer using finite dipole antennas at microwave frequencies.

The aim of this chapter is to introduce the concept of modifying the spontaneous emission and resonance energy transfer. We shall summarize the key historical developments and the current research efforts. The rest of the chapter is divided into four parts. Starting in Sec. 1.1, we briefly summarize the concept of modification of spontaneous emission and local density of states. We shall review the seminal experiments and current efforts to modify spontaneous emission. We then outline the classical analogy to spontaneous emission and local density of states with finite sized antennas, where we emphasize the advantages of the classical approach. Next in Sec. 1.2 we introduce resonance energy transfer. Particular emphasis is given to the near-field transfer and its relevance to Förster resonance energy transfer. We sketch the key concepts in resonance energy transfer and motivate the development of its equivalent semi-classical analogue. In the third part Sec. 1.3 we shift the focus to hyperbolic metamaterials. The field of metamaterials has completely transformed the way we think about electromagnetism. It has opened up new and interesting ways to manipulate electromagnetic waves. Hyperbolic metamaterials are a class of metamaterials that have offered new possibilities to control the rate of spontaneous emission in recent times. We present the essential theory behind hyperbolic metamaterials and contrast their properties with conventional materials. We demonstrate how hyperbolic metamaterials enhance the spontaneous emission rates. These concepts will be useful for later chapters when we make measurements in such a metamaterial. Finally, in Sec. 1.4 we end with an outline of the rest of the thesis.

1.1 Spontaneous emission

The spontaneous emission rate (γ) of an atom, is influenced by the local electromagnetic environment of the atom. Calculation of spontaneous emission rate of an atom, denoted by a two level quantum mechanical system requires a full quantum electrodynamical (QED) treatment as first pointed out by Wigner and Weiskopf [3]. The concept of local density of states (LDOS) was introduced [4] to characterize the influence of the environment on the decay rate. The spontaneous emission rate of an atom located at $\mathbf{r}_0$ is [5]

$$\gamma = \frac{\pi\omega_0}{3\hbar\varepsilon_0}|\boldsymbol{\mu}|^2\rho(\mathbf{r}_0,\omega_0) \tag{1.1}$$

where ω_0 is the transition frequency, ε_0 is the permittivity of free space, $\hbar$ is the Planck constant, and $\boldsymbol{\mu} = |\boldsymbol{\mu}|\hat{n}_\mu$ is the transition dipole moment matrix element between the two levels pointing in direction $\hat{n}_\mu$. In Eq. (1.1) $\rho(\mathbf{r}_0,\omega_0)$ is the local density of states (LDOS), the factor of 3 in the denominator of Eq. (1.1) is due to the orientational averaging of the dipole moment [6]. In Eq. (1.1) the presence of other energy levels is neglected and the atom field coupling is assumed to be electric dipolar in nature, which is justified because the size of the atom is much smaller than the wavelength of emission. In this work we limit ourselves to the weak coupling regime, it is assumed that the dipole moment $\boldsymbol{\mu}$ and transition frequency ω_0 is unaffected by the environment. In this approximation, the influence of the environment on decay rate is contained entirely in the LDOS. Thus, spontaneous emission rate is partly an intrinsic quantity, the dipole moment $\boldsymbol{\mu}$, transition frequency ω_0 are intrinsic to the type of the emitter, while the LDOS $\rho(\mathbf{r}_0,\omega_0)$ depends upon the environment.

For the particular case of vacuum the local density of states is given by [5]

$$\rho_0 = \frac{\omega_0^2}{\pi^2 c^3}, \tag{1.2}$$

where c is the speed of light in vacuum. Substituting Eq. (1.2) in Eq. (1.1) we obtain the well known decay rate for an atom in vacuum,

$$\gamma_0 = \frac{\omega_0^3|\boldsymbol{\mu}|^2}{3\pi\varepsilon_0\hbar c^3}. \tag{1.3}$$

The concept that electromagnetic environment can modify spontaneous emission was first proposed by Purcell [1]. The figure of merit which is the ratio of the rate of spontaneous emission in the electromagnetic medium (γ) to that in vacuum (γ_0) is the Purcell factor (F). Purcell showed that when an atom is placed inside a single mode cavity, with a mode frequency which is resonant with the transition frequency of the atom, the rate of spontaneous emission of the atom is modified and the Purcell factor is

$$F \equiv \frac{\gamma}{\gamma_0} = \frac{3Q\lambda^3}{4\pi^2 V} \tag{1.4}$$

where Q is the quality factor of the cavity mode, λ is the wavelength, and V is the mode volume.

The first experimental observation of decay rate modification in fluorescence molecules was reported by Drexhage [7, 8]. By precisely controlling the separation between the fluorescent dye molecules and of the silver mirror using a dielectric spacer layer, Drexhage was able to characterize the influence on the decay rate. Another seminal experiment which elucidates role of LDOS on spontaneous emission was performed by Hulet et al [9]. If an atom is placed inside a cavity such that the cavity dimensions are small compared to the wavelength of emission λ, then spontaneous emission is inhibited. For example, this is the case if an atom is inside a parallel plate cavity such that the wavelength of emission of atom λ is larger than the cut-off, that is, $\lambda/2d > 1$, d being the separation between the plates. In the cut-off regime of the waveguide, the density of states vanishes, and so does the LDOS that is, $\rho = 0$. Thus, the spontaneous emission of atoms is inhibited, due to the lack of available modes for the emitted photon couple into.

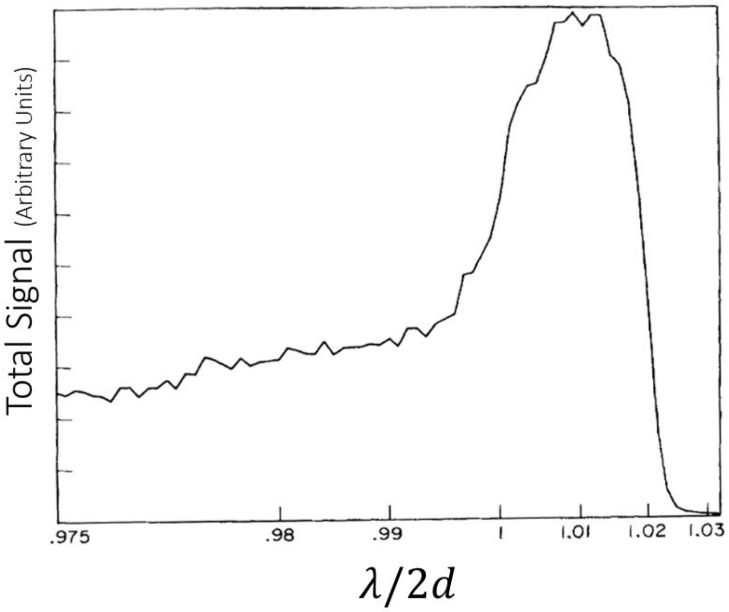

Figure 1.1: Number of atoms in the excited state, also exiting the cavity in their excited state, inside and outside the cut-off regime of a parallel plate waveguide. (Source: Hulet et al [9])

In Hulet's experiment [9], (Fig. 1.1) Cesium atoms in an excited state were passed through a parallel plate cavity with spacing d such that the wavelength emission of the atom is close to the cut-off, $d \approx \lambda/2$. Then, by applying a corresponding low frequency electric field, the transition frequency λ of the atoms was changed through the Stark effect. Exiting the cavity, the number of atoms in the excited state and the ground state were ascertained inside $(\lambda/2d > 1)$ and outside $(\lambda/2d < 1)$ the cut-off regime of the waveguide. In Fig. 1.1 the vertical axes is related to the number of atoms in the excited state exiting the cavity. The number of atoms in the excited state is higher in the cut-off region $(\lambda/2d > 1)$ as the LDOS $\rho = 0$, and spontaneous emission is suppressed. This experiment clearly indicates how the electromagnetic modes and LDOS can be used to control spontaneous emission.

With the evolution of photonics and advances in fabrication techniques which now enable us to pattern materials at scales smaller than the optical wavelengths, the Purcell factor has now been studied in a variety of structures. Modifying spontaneous emission has been studied in spherical resonators [10], nano-antennas [11, 12], and photonic crystals. [13–16]. While photonic crystals can effectively control the Purcell factor, a drawback generally associated with photonic crystals is the narrow operational bandwidth. An intriguing proposal to overcome narrow operational bandwidth and achieve broadband enhancement of the Purcell factor is to use hyperbolic metamaterials (HMM) [17]. Hyperbolic metamaterials and their salient features which make it amenable to engineering the Purcell factor are discussed in greater detail in Sec. 1.3. Later, in Chapter 3 we shall also provide measurement results for the Purcell factor in a microwave hyperbolic metamaterial.

1.1.1 Applications of engineering LDOS

Modifying decay rates has applications in improving the performance of a variety of devices. Here we briefly describe three areas: light emitting diodes, single photon emitters, and thermophotovoltaics where the ability to enhance the Purcell factor may potentially prove decisive in future.

Light emitting diodes

Achieving a high Purcell factor initially attracted interest for improving the efficiency of light emitting diodes (LED), leading to an investigation into increasing the Purcell factor for LEDs by using micro-cavities [18] and plasmonic coatings [19]. Metal based plasmonic systems have a broadband response, but Ohmic losses in the metals curtail the gains in enhancement of emission rates [20]. An application of this approach is the ability to achieve high modulation frequencies in telecommunication systems. While conventional LED sources can be modulated in the range 25-50 GHz, by enhancing the Purcell factor using nano-cubes [21] modulation frequencies up to 90 GHz have been achieved. Faster LEDs can drastically reduce the latency in data transfer at short ranges, for example between two processors.

Single photon sources

Single photon sources are required for integrated optics and quantum computation. The challenge is to achieve a source with high modulation speed, capable of coupling into a single mode, with high efficiency. Gap plasmonic antennas have been successful in reducing the lifetimes of emitters from the order of ~ 100 ps to ~ 10 ps [22]. Other proposals include coupling single quantum dots to photonic crystal waveguides [23] and micro-cavities [24]. In photonic crystals, as in other structured materials, the LDOS is highly sensitive to the location, hence precise positioning of quantum dots is a technical challenge [25].

1.1.2 Classical analogue to modification of spontaneous emission

Although a full treatment of spontaneous emission requires the use of a QED formulation, within the semi-classical approximation [26], the spontaneous emission rate γ of an atom is linearly related to the power emitted by a classical dipole P as $\gamma = P/\hbar\omega_0$. Later in Chap. 2 we discuss in greater detail, that if an atom is replaced with a classical dipole, the power emitted by the classical dipole would be modified in the same way as the spontaneous emission rate of an atom. The Purcell factor (Eq. (1.4)) can thus be expressed classically with dipoles, as $F = P/P_0$ where P_0 is the power emitted by the dipole in vacuum. The theory of emission by classical dipoles does not require QED or the concept of vacuum fluctuations, thus simplifying the problem considerably while preserving the essential underlying mechanism.

The first experimental proof of concept results (Fig. 1.2) were reported by Dowling [27] in 1991. He showed that the power at 1 GHz emitted by a classical dipole antenna placed inside a parallel plate cavity depends on the ratio λ/L, L being the separation between the plates, in direct analogy with the work of Hulet [9] (Fig. 1.1). Both

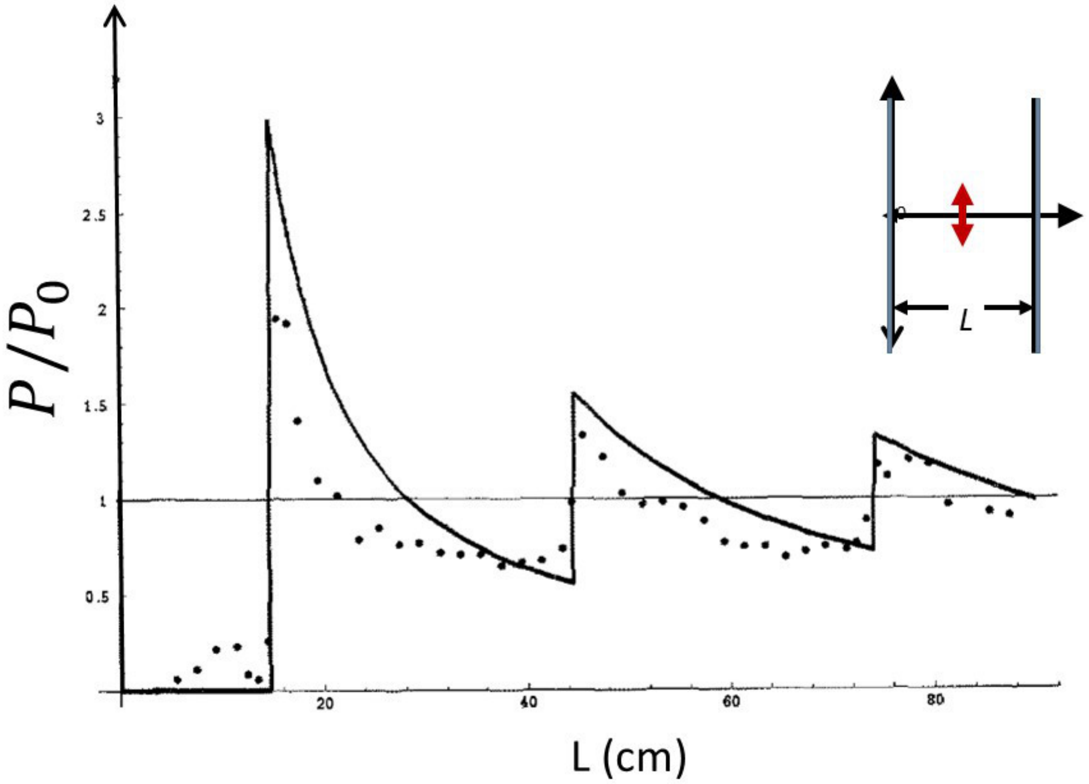

Figure 1.2: Power emitted by dipole antenna in a parallel plate cavity (dots) compared with the LDOS (solid) at 1 GHz as a function of the separation between plates. (Source: Dowling [27])

experiments aim to probe the LDOS across the cut-off regime in a parallel plate cavity. The measurement of the power emitted by a dipole antenna is in excellent agreement with the theoretical LDOS calculated inside the cavity. In Fig. 1.2 which applies to a frequency 1 GHz, the cut-off regime of parallel plate waveguide is below $L < \lambda/2 = 15$ cm. Below the cut-off there are no modes and LDOS is zero thus the dipole cannot emit. The conclusion is similar to Hulet's experiment where below the cutoff, the atom could not decay to the ground state, increasing its lifetime.

The experiments in Fig. 1.2 were performed at $\lambda = 30$ cm, and while quantum mechanical effects can occur at such microwave wavelengths, with its study being a popular field of research [28–30]. In conventional radio-frequency engineering such effects can be safely ignored, hence the modification of emission of the antenna in Fig. 1.2 is a truly classical effect [27, 31].

The area gained renewed attention following the work of Greffet [32] who established the link between the impedance of an antenna to the LDOS and the Purcell factor. Impedance is a well studied quantity in antenna theory, and it allows the concept of

LDOS to be extended from optical frequencies to microwave frequencies and beyond. Following the development of circuit models [33], the Purcell factor was measured near a conducting interface at microwave frequencies, similar to Drexhage's experiment.

Studying the LDOS at longer wavelengths has advantages which go beyond the obvious ease of experimentation, fabrication, and accurate positioning of emitters. The most striking advantage is that antennas have a naturally defined and controllable dipole moment. Even in the seminal experiments of Drexhage [7], an orientational average of the dipole moments of the collection of fluorescent molecules had to be performed, so as to compare the experimental results with theory. However with antennas the orientational dependence of the Purcell factor is naturally resolved [33]. Another advantage is the ability to measure the magnetic Purcell factor. The strongest atomic transitions are electric dipolar in nature but magnetic dipolar transitions also exist, though they are much weaker. The modification of decay rates where the atom field coupling is magnetic dipolar, and the magnetic Purcell factor, have not been studied extensively. The magnetic Purcell factor can be straightforwardly measured with antennas [34] by replacing an electric dipole antenna with a magnetic loop antenna. These experiments of magnetic Purcell factor have been performed in microwaves. The modification magnetic Purcell factor with nanophotonic structures is now attracting more attention [35].

In this section we discussed the role of environment on spontaneous emission. In the next section we turn our attention to another important process: resonance energy transfer. Resonance energy transfer is the process of transfer of excitation from an atom in an excited state to an atom in a ground state. We shall discuss how the environment influences resonance energy transfer between two atoms and its corresponding classical analogue.

1.2 Resonance energy transfer.

In the second part of the thesis we analyze the effect of the environment on the resonance energy transfer between two atoms. Resonance energy transfer (Fig. 1.3) is the exchange of excitation between two atoms or molecules. In the initial state the system comprises of two atoms, each denoted by individual two level systems, one of which is in the excited state while the other is in the ground state. During the process of resonance energy transfer the excited state atom (donor), transfers its energy to the atom in the ground state (acceptor). The donor atom relaxes to its ground state, while the acceptor gains energy into its excited state [5].

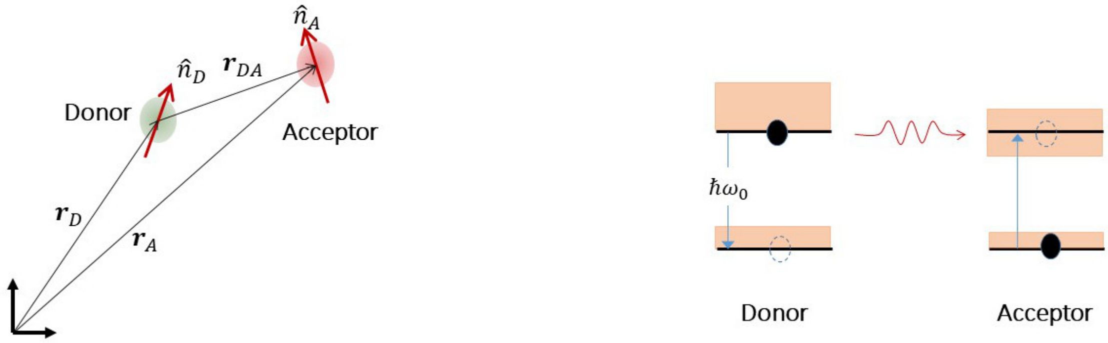

Figure 1.3: Schematic of resonance energy transfer in a donor acceptor system. Left: classical; right: quantum mechanical manifestation. (Source: Novotny and Hecht [5]).

Resonance energy transfer was first observed in a mixture of mercury and thallium vapor. Even when the mixture was only excited at the transition frequency of mercury, emission was reported from thallium [36]. It was initially thought that energy was transferred from mercury atoms to thallium atoms due to mechanical collisions between atoms, but calculations showed that energy was being transferred at distances greater than collision radii of atoms. Subsequent experiments [37] showed that the intensity of emission increased with decreasing difference of the transition frequencies of the participating donor acceptor atoms. Demonstrating that resonance of the energy levels between the donor and acceptor plays a significant role in energy transfer.

1.2.1 Förster resonance energy transfer

One of the early quantitative descriptions to explain transfer of excitation between atoms at distances beyond the collision radii (assuming atoms to be hard spheres with a fixed radius) was given by J. Perrin [38, 39]. He assumed that semi-classically the energy transfer between two atoms was like energy transfer between two classical point dipoles in the near field ($k_0 r_{DA} < 1$, where $k_0 = 2\pi/\lambda$, and λ is the wavelength) and, considered the particular case where the resonance frequency of the donor and acceptor were almost identical. Subsequently, a quantum mechanical theory was formulated by F. Perrin [40–42] which also took into account the spectral broadening of the energy levels.

Förster's breakthrough was to express the energy transfer in terms of the overlap of the emission and absorption cross sections of the molecules, which allowed comparison with experiments. Förster's theory was able to correctly deduce the r_{DA}^{-6} dependence of energy transfer rate, r_{DA} being the distance between donor and acceptor. The energy transfer when the donor and acceptor separation is subwavelength is due to a near field, non-radiative mechanism which is referred to as Förster resonance energy transfer (FRET).

Once the donor molecule is in its excited state, it can decay through several competing radiative and non-radiative mechanisms. The presence of the acceptor molecule in close proximity provides an additional pathway for the donor to de-excite. Hence, the donor fluorescence lifetime is decreased compared to the case without the acceptor ($\tau_{DA} \leq \tau_D$). The decay rate is inversely proportional to the lifetime of the emitter. The difference in the decay rates of the donor with and without the acceptor is the FRET rate [5] $\gamma_F = \gamma_{DA} - \gamma_D$. The other useful quantity is the FRET efficiency η_F defined as [5]

$$\eta_F = 1 - \frac{\tau_{DA}}{\tau_D}. \tag{1.5}$$

If $\eta_F = 1$ all energy lost by donor is absorbed by acceptor. On the other hand if $\eta_F = 0$ no energy is transferred from donor to acceptor, but lost through other channels, for example radiation. As the energy transfer in the near field scales as r_{DA}^{-6} it is convenient to define a distance called Förster radius R_0, such that when $r_{DA} = R_0$ the FRET efficiency η_F is 0.5,

$$\eta_F = \frac{R_0^6}{r_{DA}^6 + R_0^6}. \tag{1.6}$$

In a homogeneous medium with refractive index n, the Förster radius can be expressed as [43]

$$R_0^6 = \left(\frac{9000\ (\ln 10)}{128\pi^5 N_A}\right) n^{-4} Q_D \kappa^2 M \tag{1.7}$$

where N_A is the Avogadro number, Q_D is the quantum yield of the donor, κ^2 accounts for the relative orientations of the donor and acceptor dipole moments, and the overlap integral

$$M = \int \sigma_D(\lambda) \cdot \sigma_A(\lambda) \cdot \lambda^4 \mathrm{d}\lambda \Big/ \int \sigma_D(\lambda) \mathrm{d}\lambda\ . \tag{1.8}$$

$\sigma_D(\lambda)$ is the fluorescence emission of the donor, $\sigma_A(\lambda)$ is the absorption of acceptor, and λ is the wavelength.

The fast scaling of FRET with distance (r_{DA}^{-6}) cause FRET effects in optical (400 nm$<$ $\lambda < 700$ nm) experiments to be significant only at distances up to $r_{DA} \sim 10$ nm [43]. In FRET experiments, the greatest challenge is the precise positioning of the donor-acceptor molecules at nanometer scale. Development of better dyes and optical instrumentation [44] have increased the sensitivity of experiments. For controlling donor acceptor distance, it is now possible to attach dyes based on Green fluorescent proteins at specific locations in protein molecules [45]. Another approach which has been gaining popularity is to attach donor-acceptor molecules at predetermined sites on a DNA molecule [46]. Over small scales the DNA molecule is rigid in nature and thus the donor acceptor pair are held in place with known, accurate spacing.

There are two commonly used techniques to measure FRET. First, intensity measurements: In early experiments, comparison of intensities of the donor was the preferred method [47, 48]. It involves measuring the donor intensity when donor-acceptor are both present and comparing it with the case when only the donor is present: The challenge here is to get a good reference measurement. The concentrations of both solutions have to be equal, which can be challenging. Second, lifetime measurements: With the development of fast and sensitive detectors based on charged coupled devices (CCD), it is now easier to measure directly the change in lifetime of the dyes. Lifetime measurements have the advantage over intensity measurements that they are concentration independent [44].

With the development of pulsed lasers the technique of fluorescence lifetime imaging microscopy (FLIM) [49] has emerged. An ultra short excitation pulse of the order of the lifetime of the donor is used to excite the dye molecules. A time resolved fluorescence intensity measurement can then be used to obtain the decay rate of the donor. FRET-FLIM techniques require the use of confocal microscopy which in turn requires complex optics. An innovative way to bypass the limitation is to use photobleaching [50] to measure the FRET rate. Photobleaching-based FRET experiments can be performed on conventional wide-field microscopy setups. Photobleaching is the process in which the donor molecule in the excited state goes through an irreversible photochemical change which makes the molecule unable to fluoresce. The rate of photobleaching is proportional to the time the molecule spends in its excited state. FRET causes the lifetime of the donor in the excited state to decrease, as the FRET rate increases, the donor spends less time in the excited state and the rate of photobleaching reduces. Thus the amount of photobleaching can be used to deduce the FRET rate. In this approach a continuous laser is used and the intensity of the donor is measured over a time which is typically of the order of ~ 1 s. Compared with nanosecond scale lifetime measurements, 1 s measurements do not require sophisticated detectors.

The LDOS is related to the influence of the environment on the decay rate of the emitters, the relation of LDOS to the FRET rate has been a controversial topic in literature. With the early experiments, reporting that LDOS is directly correlated to FRET rate [51, 52]. While others found no correlation between LDOS and the FRET rate [53]. In order to precisely control the separations, in Ref. [54] experiments were performed by attaching donor and acceptor molecules at different locations on a DNA molecule, and found that FRET rate is independent of LDOS. A subsequent theory was also developed [2], showing that the rate of energy transfer depends on the LDOS, but averaged over a wide frequency range, from zero frequency to ultraviolet frequencies. However, the average of LDOS, over a large frequency range, for most environments, is unchanged. Hence, the FRET rate does not depend on the LDOS.

1.2.2 Applications of FRET

Resonance energy transfer mediated by dipole-dipole interactions is a well studied problem by physicists, chemists, and biologists. Though an old problem, its importance has steadily grown with time. Like spontaneous emission, where the electromagnetic modes influence the rate of decay, the electromagnetic modes can also modify the resonance energy transfer between two molecules. There have been recent studies to modify FRET using nano-antennas [55], cavities [2], and hyperbolic metamaterials [56, 57].

Photosynthesis

Perhaps the most vital phenomena which involves FRET is photosynthesis in plants. In photosynthesis, light is absorbed by certain dyes (chromophores) and the energy needs to be rapidly transported to photosynthetic reaction sites. Oppenheimer [58] pointed out that this process is highly efficient and cannot be due to emission and re-absorption of the photon. It is now understood that FRET plays a vital role in the energy transport mechanism in photosynthesis [59, 60].

Photovoltaics

An application of FRET is in development of efficient light harvesting devices for solar energy. The near-field, non-radiative transfer of energy across short distances using FRET has been applied to solar cells [61]. Donor-acceptor dye based solar cells [62–65] are more efficient than conventional organo-metallic dye based system.

Metrology

One of the first proposed applications for FRET was its use as a spectroscopic ruler at the nanometer scale [66]. Although, the range of FRET is not significant for distances larger than 10 nm, its extreme sensitivity to donor-acceptor distance at that length scale makes it a viable choice to measure nm scale distances. The technique has been successfully applied in mapping the structure of proteins [67]. Apart from the distance, the relative orientation of the dipole moments of the donor and acceptor also have to be accounted for [68]. Since the orientation of the dipole moment of molecules is harder to control than distances, FRET is better for measuring change in distance between donor and acceptor, rather than absolute distances [46, 69].

1.2.3 Classical analogue to resonance energy transfer

As the atom-field coupling is dipolar in nature it is not surprising that in the semi classical approximation the rate of resonance energy transfer from the donor to the acceptor $\Gamma_{D\to A}$ is related to the power transferred between two classical dipoles $P_{D\to A}$ as [5]

$$\Gamma_{D\to A} = \frac{P_{D\to A}}{\hbar\omega} \tag{1.9}$$

In this thesis the aim is to characterize the influence of the environment on resonance energy transfer. Later in Chap. 4 we show that influence of the environment on resonance energy transfer between two atoms is equivalent to the influence on the energy transfer between two classical dipoles. We demonstrate that this concept can be developed to perform measurements with finite sized antennas to characterize the influence of electromagnetic modes on resonance energy transfer at microwave frequencies.

Unlike spontaneous emission where antenna based methods have become a popular tool to measure the Purcell factor at longer wavelengths, antenna based circuit models have not been explored in great detail for FRET like energy transfer. In Chapter 4 we work out the theory underlying the antenna based formalism to study resonance energy transfer. We present experiments for resonance energy transfer in vacuum at microwave frequencies with antennas, where in the near field regime the characteristic r_{DA}^{-6} dependence is measured. We then measure the modification in resonance energy transfer in a parallel plate cavity and compare it with theoretical results in the literature. It is the first time an antenna based formalism has been applied to study FRET at microwaves.

1.2.4 Advantages of studying resonance energy transfer with antennas

FRET experiments in optics as described previously (Sec. 1.2.1), are intricate as they require accurate attachment of molecules at nanometer scale distances. In addition, lifetime measurements need pulsed lasers and sophisticated detectors. Interestingly, even with all the sophisticated and innovative ways to characterize FRET, none of the optical measurement techniques can measure directly the energy transferred from the donor to the acceptor. This is because FRET is a dark-process, mediated by virtual photons. All techniques mentioned depend on measuring the changes in intensities and lifetimes, and are basically indirect ways of obtaining the FRET energy transfer. However, unlike optical measurements, at microwave frequencies it is possible to measure the power transfer from donor to acceptor antennas directly with conventional techniques. This is the main motivation behind the development of antenna models to study resonance energy transfer at longer wavelengths. At the same time, increasing the wavelength can simplify experiments while preserving the physics, thus making it easier to investigate the role of the environment on resonance energy transfer.

In this section we described the essential concepts of resonance energy transfer. We now introduce hyperbolic metamaterials. Hyperbolic metamaterials have attracted a lot of attention because of their ability to influence the decay rates of emitters. Later in Chap. 3 we shall also be studying the Purcell factor in a microwave hyperbolic metamaterial.

1.3 Hyperbolic metamaterials

1.3.1 Introduction to hyperbolic metamaterials

Hyperbolic metamaterials are a class of metamaterials that acquire their name from their dispersion relations, which are hyperbolic in nature. These materials have an indefinite anisotropic permittivity tensor [70]. They were studied by Narimanov and coworkers [17, 71] to engineer photonic density of states. They have been shown to enhance the LDOS [72], resonance energy transfer [56], and they can be used to engineer blackbody radiation[73]. Wire media based hyperbolic metamaterials have also been used for imaging because of their ability to resolve beyond the diffraction limit [74, 75]. During the course of the PhD, the candidate also worked on developing hyperbolic metamaterials, to mimic electromagnetic response of tokamak plasmas. The work can be found in Appendix. C, though it will not be discussed further in this manuscript. In this section we shall introduce the theory behind the LDOS and Purcell factor in hyperbolic metamaterials, and discuss the advantages and limitations of using hyperbolic metamaterials to enhance local density of states.

Consider a material with a uniaxial anisotropic permittivity such that the permittivity in the xy plane is negative $\mathrm{Re}\{\varepsilon_{//}\} < 0$ and permittivity along $\hat{z}$ is positive, $\mathrm{Re}\{\varepsilon_z\} > 0$. In literature these are referred to as type II hyperbolic metamaterial [76]. A similar treatment can also be developed for type I hyperbolic metamaterials for which $\mathrm{Re}\{\varepsilon_{//}\} > 0$ and $\mathrm{Re}\{\varepsilon_z\} < 0$. The diagonal permittivity tensor is expressed as

$$[\bar{\varepsilon}] = \begin{bmatrix} \varepsilon_{//} & 0 & 0 \\ 0 & \varepsilon_{//} & 0 \\ 0 & 0 & \varepsilon_z \end{bmatrix} \tag{1.10}$$

For a material with such a uniaxial anisotropic permittivity tensor, the propagating electromagnetic waves in the structure can be split into transverse electric (TE$_\mathrm{z}$) polarization for which the electric field $\mathbf{E}$ lies completely in the $x-y$ plane ($E_z = 0$) and transverse magnetic (TM$_\mathrm{z}$) polarization where the magnetic field $\mathbf{H}$ lies completely in the $x-y$ plane ($H_z = 0$). The dispersion relations between the wave-vector $\mathbf{k} = (k_x, k_y, k_z)^T$ and frequency ω, for such a uniaxial anisotropic media were derived in Ref. [77]. The dispersion relations in such a hyperbolic medium for the TE$_z$ and TM$_z$ polarizations are [72, 76]

$$\mathrm{TE_z}: \qquad \frac{k_x^2 + k_y^2 + k_z^2}{\varepsilon_{//}} = \frac{\omega^2}{c^2}, \tag{1.11}$$

$$\mathrm{TM_z}: \qquad \frac{k_x^2+k_y^2}{\varepsilon_{zz}} - \frac{k_z^2}{\mid \varepsilon_{//} \mid} = \frac{\omega^2}{c^2}. \tag{1.12}$$

For the TM_z polarization, the isofrequency dispersion is hyperbolic which is the reason why such materials are called hyperbolic metamaterials.

Fabrication

The indefinite permittivity tensor of the hyperbolic metamaterial ($\mathrm{Re}\{\varepsilon_{//}\} \cdot \mathrm{Re}\{\varepsilon_z\} < 0$) implies that a hyperbolic metamaterial behaves like a metal in one direction and as a dielectric material in the other direction. The two common ways to realise the required dielectric response are by using a) wire medium and b) alternating metal dielectric layers.

a) Wire medium

It is possible to achieve an indefinite effective permittivity required for hyperbolic metamaterials by embedding an array of thin metallic wires with subwavelength periodicity in a dielectric matrix. Wire medium based metamaterials for optical wavelengths are usually fabricated by growing gold or silver wires in a porous alumina template [78, 79]. For bulk fabrication of metamaterials working at longer wavelengths, fibre drawing techniques have also been developed [80]. These wire-based metamaterials find extensive use in sub-diffraction imaging [81–85]. Wire media have been extensively studied at optical [83], terahertz [74] and microwave frequencies [84] as imaging devices. At long wavelengths wire media act as type I hyperbolic metamaterial. Wire media has strong spatial dispersion [85] which curtails their hyperbolic behavior, but is useful for imaging applications.

b) Metal dielectric layers

The second popular approach for fabricating metamaterials with effective hyperbolic permittivity tensors is to deposit alternating metal and dielectric layers [71, 86]. While layered metamaterials can exhibit both type I and type II characteristics depending upon the frequency of operation, it is easier to obtain type II behavior [76]. Layered media also pose a fabrication challenge as it can be difficult to deposit a large number of thin layers.

1.3.2 LDOS in hyperbolic metamaterials

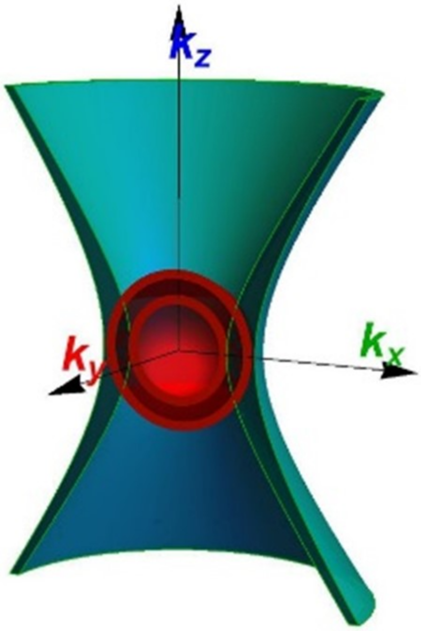

Figure 1.4: Iso-frequency surfaces for two close frequencies in a hyperbolic metamaterial (blue) compared with iso-frequency surfaces of an isotropic medium (red).

The most noticeable consequence of the hyperbolic dispersion relations is that the medium can support propagation of waves with large wavevectors. This is why they are sometimes referred to as indefinite materials [70]. In vacuum, such waves cannot propagate and decay exponentially. In principle hyperbolic metamaterials can support infinitely large propagation vectors due to the open form of the isofrequency surface obtained from the hyperbolic dispersion relation, but in practise is limited due to losses.

If an emitter is placed inside or close to a hyperbolic metamaterial, the decay rate of the emitter is determined by the density of available electromagnetic states. The density of states, represents the volume enclosed between two isofrequency surfaces formed by frequencies ω and $\omega + \mathrm{d}\omega$. In sharp contrast to an ellipsoid or sphere, a hyperbola is an open structure. Hence, in principle, the density of states which is the volume between two isofrequency surfaces can diverge. In practice however, the DOS is finite due to and due to finite dimensions of the constituents.

The photonic density of states has been studied experimentally in hyperbolic metamaterials [87, 88]. When fluorescent molecules or quantum dots are placed in vicinity of a hyperbolic metamaterial, radiation from the emitters couple into the modes with the highest density of states. In a hyperbolic metamaterial the large density of states decreases the lifetime of the emitters. It is important to discern the radiative and non-radiative contribution to the decay rate, as non-radiative dissipation into heat in metals is significant at optical frequencies [89].

In addition to optical frequencies, LDOS and the Purcell factor have been extensively studied in hyperbolic metamaterials at microwave frequencies using the analogy between the impedance of an antenna and the LDOS [32]. However most of the studies for LDOS at microwaves have been focused on enhancement of the Purcell factor for wire medium (Type I) based metamaterials [90, 91]. The Purcell factor in a Type II hyperbolic metamaterial has been relatively unexplored compared to Type I metamaterials at microwaves. A Type II hyperbolic metamaterial exhibits dramatically different Purcell factor depending upon the polarization (transverse electric (TE) or transverse magnetic (TM)) of the mode the emitter emits into. The novel aspect of this work is that we exploit the fact that antennas can be oriented accordingly inside a Type II hyperbolic metamaterial structure, to select the polarization of the mode they emit into. This enables us, for the first time to resolve the contribution of the individual modes to the Purcell factor, and compare that with the Purcell factor obtained from band-structure calculations [92].

1.4 Thesis outline

The rest of the thesis is organized as follows:

In Chapter 2, we summarize the theory in literature for modification of spontaneous emission and the Purcell factor. The relationship between LDOS and the classical Green function is established. The semi-classical analogue of spontaneous emission using dipoles as emitters is discussed. The classical treatment of the Purcell factor is developed for measurements with using finite length antennas. For a sub-wavelength antenna it is demonstrated that a measurement of the real part of the input impedance of the antenna gives the Purcell factor. The ability to measure the Purcell factor from antennas, extends the frequency range of measurement of the Purcell factor from optical to microwave frequencies.

In Chapter 3 we study the Purcell factor in periodic fishnet metamaterial designed to operate at microwave frequencies. Numerical computations of density of states of the periodic unit cell of the metamaterial are carried out. The electric and magnetic Purcell factor are measured with antennas in the metamaterial structure. The Purcell factor was obtained by measuring the change in the impedance of an antenna in the frequency range 5-15 GHz. Measurements were compared with finite difference time domain simulations of the Purcell factor.

In Chapter 4 we develop the theory for measurement of resonance energy transfer using antennas. It is the first time antenna based formalism has been applied to study resonance energy transfer at microwave frequencies. Briefly summarizing the QED results, the role of the Green function in resonance energy transfer is highlighted. The classical antenna based analogue to resonance energy transfer is then established. We derive that if a two-port network is linearly coupled with subwavelength antennas, then the mutual impedance is proportional to the Green function. The mutual impedance can be measured using conventional microwave measurement techniques which makes it possible to study resonance energy transfer at longer wavelengths.

In Chapter 5 we present measurement results for resonance energy transfer vacuum where we measure the characteristic r_{DA}^{-6} dependence of power transferred as well as the orientational dependence. To elucidate the effect of modes on the resonance energy transfer, we then perform measurements in cavities. We compare the measurements with analytical results in literature for resonance energy transfer. Finally, the conclusions of the work are presented in Chapter 6.

Chapter 2

Spontaneous emission

The aim of the chapter is to describe the theoretical framework to study the influence of the electromagnetic environment on the spontaneous emission rate of a two level quantum mechanical system. Emphasis is placed upon the role of the Green function and its relation to the local density of states (LDOS). Next we study the influence of the electromagnetic environment on the power emitted by a classical point dipole. In the semi-classical approximation, the influence of the electromagnetic modes on the rate of spontaneous emission is the same as that on the power radiated by a classical dipole. Usually the LDOS and spontaneous emission rates are studied through measurements of changes in decay rates of fluorescent molecules [7, 93]. The classical treatment, while simplifying the problem, preserves the underlying physics. We go on to show that the impedance of a classical dipole antenna is a classical analogue to LDOS. For sub-wavelength, finite-sized antennas, the input impedance and hence the LDOS can be measured experimentally at longer wavelengths. This chapter lays the theoretical groundwork for experimental studies in the rest of the thesis.

Starting with the Maxwell equations in Sec. 2.1, the Green function formalism to solve the wave equation is developed in Sec. 2.2. The modal approach is presented in Sec. 2.3 and its relation to the Green function is established. The quantum mechanical approach for spontaneous emission in the Wigner-Weiskopf approximation is developed in Sec. 2.4 where the influence of the electromagnetic modes on the decay rate is characterized. The Purcell factor is introduced in Sec. 2.5. The influence of the environment on the radiation by classical dipole studied in Sec. 2.6. Antennas are introduced in Sec. 2.7 and a classical analogue to the Purcell factor is derived from the antenna impedance. An equivalent lumped circuit based model for the Purcell factor is also discussed (Sec. 2.8). Extension of the concept to the magnetic Purcell factor is discussed in Sec. 2.9. In Sec. 2.10 the basics of microwave measurements are discussed and simple one-port and two-port microwave networks are analyzed. In Sec. 2.11, as a demonstration of the effectiveness of the formalism developed, we take the example of the Purcell factor near a perfectly conducting interface, where measurements of the Purcell factor in literature at optical frequencies with fluorescent molecules are compared with microwave measurements with antennas.

2.1 Maxwell's equations

All classical electromagnetic phenomena can be described by the Maxwell equations [94]. In a region without free charges ($\rho_e = 0$) the Maxwell equations are

$$\nabla \times \mathbf{E}(\mathbf{r};\omega) = i\omega\mathbf{B}(\mathbf{r};\omega), \tag{2.1}$$

$$\nabla \times \mathbf{H}(\mathbf{r};\omega) = -i\omega\mathbf{D}(\mathbf{r};\omega) + \mathbf{j}, \tag{2.2}$$

$$\nabla \cdot \mathbf{D}(\mathbf{r};\omega) = 0, \tag{2.3}$$

$$\nabla \cdot \mathbf{B}(\mathbf{r};\omega) = 0, \tag{2.4}$$

where $\mathbf{E}$ is the electric field, $\mathbf{H}$ is the magnetic field, $\mathbf{D}$ is the electric displacement, $\mathbf{B}$ is the magnetic induction, $\mathbf{j}$ is the current density. The fields are assumed to have a $e^{-i\omega t}$ time dependence of the form

$$\mathbf{E}(\mathbf{r},t) = \mathrm{Re}\{\mathbf{E}(\mathbf{r})e^{-i\omega t}\} \tag{2.5}$$

where ω is the angular frequency. In a linear, non-magnetic medium with a relative permittivity $\varepsilon(\mathbf{r},\omega)$ the constitutive relations between the electric field $\mathbf{E}$, magnetic field $\mathbf{H}$, electric displacement $\mathbf{D}$, and magnetic induction $\mathbf{B}$ are given by

$$\begin{aligned} \mathbf{D} &= \varepsilon_0\varepsilon(\mathbf{r},\omega)\mathbf{E}, \\ \mathbf{B} &= \mu_0\mathbf{H}, \end{aligned} \tag{2.6}$$

where ε_0 and μ_0 denote permittivity of free space and permeability of free space respectively. By applying the curl operator ($\nabla\times$) on both sides of Eq. (2.1) and using Eq. (2.2) a wave equation can be derived

$$\nabla \times \nabla \times \mathbf{E}(\mathbf{r};\omega) - \varepsilon(\mathbf{r},\omega)\left(\frac{\omega^2}{c^2}\right)\mathbf{E}(\mathbf{r};\omega) = i\omega\mu_0\mathbf{j}. \tag{2.7}$$

where $c = (\mu_0\varepsilon_0)^{-1/2}$ is the speed of light in vacuum. Through an analogous procedure, the wave equation for the magnetic field **H** can also be derived. Two common approaches to solving the wave equation Eq. (2.7) are the Green function method and expansion in orthogonal eigenmodes. Both approaches will be presented next and the relation between the two will be established.

2.2 Green function for electromagnetic wave equation

The Green function is a tensor which denotes the fundamental solution of the wave equation (Eq. (2.7)) at the location $\mathbf{r}$, with a point dipole source located at $\mathbf{r}'$. In cartesian coordinates, the Green function $\overset{\leftrightarrow}{\mathbf{G}}(\mathbf{r},\mathbf{r}';\omega)$ cab be represented by a 3×3 matrix of the form

$$\overset{\leftrightarrow}{\mathbf{G}}(\mathbf{r},\mathbf{r}';\omega) = \begin{bmatrix} G_{xx} & G_{xy} & G_{xz} \\ G_{yx} & G_{yy} & G_{yz} \\ G_{zx} & G_{zy} & G_{zz} \end{bmatrix}. \tag{2.8}$$

The Green function $\overset{\leftrightarrow}{\mathbf{G}}(\mathbf{r},\mathbf{r}';\omega)$ is the solution of

$$\nabla \times \nabla \times \overset{\leftrightarrow}{\mathbf{G}}(\mathbf{r},\mathbf{r}';\omega) - \frac{\omega^2}{c^2}\varepsilon(\mathbf{r})\overset{\leftrightarrow}{\mathbf{G}}(\mathbf{r},\mathbf{r}';\omega) = \overset{\longleftrightarrow}{\mathbf{I}}\,\delta(\mathbf{r}-\mathbf{r}') \tag{2.9}$$

satisfying outgoing Sommerfeld's radiation condition in the limit $k_0|\mathbf{r}-\mathbf{r}'| \to \infty$, where $k_0 = \omega/c$, and $\overset{\longleftrightarrow}{\mathbf{I}}$ is the identity tensor. Eq. (2.9) is general in nature and valid for any arbitrary, homogeneous or inhomogeneous, open or closed systems, with or without losses. Depending upon the requirements, analytical or numerical techniques can be applied to obtain the Green function [95]. Once the Green function is obtained, the fields due to any arbitrary current distribution $\mathbf{j}(\mathbf{r}')$ can be expressed through the Green function by integrating over the volume of the source current distribution

$$\mathbf{E}(\mathbf{r};\omega) = i\omega\mu_0 \int \mathrm{d}\mathbf{r}'\overset{\leftrightarrow}{\mathbf{G}}(\mathbf{r},\mathbf{r}';\omega)\cdot\mathbf{j}(\mathbf{r}'). \tag{2.10}$$

For an (electric-) dipole source denoted by its dipole moment $\mathbf{p}$, the current density is

$$\mathbf{j} = -i\omega\mathbf{p}\delta(\mathbf{r}-\mathbf{r}'), \tag{2.11}$$

$\delta(\mathbf{r}-\mathbf{r}')$ denotes the three-dimensional Dirac delta function. For a time harmonic, point electric dipolar source $\mathbf{p}$, Eq. (2.10), is simplified to

$$\mathbf{E}(\mathbf{r};\omega) = \mu_0\omega^2\overset{\leftrightarrow}{\mathbf{G}}(\mathbf{r},\mathbf{r}';\omega)\cdot\mathbf{p}. \tag{2.12}$$

Physically this means in any environment, the electric field of a dipole source by the product of the Green function and the dipole moment.

2.3 Orthogonal modes and Green function

Another approach to solving the wave equation Eq. (2.7) is by expanding the field using eigenmodes. In a non-dispersive, non-absorbing medium in a closed cavity of volume V, it is possible to express any electromagnetic field distribution of a system as a superposition of discrete orthogonal eigenmodes $\mathbf{u}_\mathbf{k}(\mathbf{r}, \omega_\mathbf{k})$, with $\omega_\mathbf{k}$ being the eigenfrequency of the mode. These modes which form a complete orthonormal basis are solutions of the source free (homogeneous) wave equation,

$$\nabla \times \nabla \times \mathbf{u}_\mathbf{k}(\mathbf{r}, \omega_\mathbf{k}) - \varepsilon(\mathbf{r}) \frac{\omega_\mathbf{k}^2}{c^2} \mathbf{u}_\mathbf{k}(\mathbf{r}, \omega_\mathbf{k}) = 0 \tag{2.13}$$

and satisfy the orthonormality condition,

$$\int \mathbf{u}_\mathbf{k}^*(\mathbf{r}, \omega_\mathbf{k}) \varepsilon(\mathbf{r}) \cdot \mathbf{u}_\mathbf{k}(\mathbf{r}, \omega_{\mathbf{k}'}) \mathrm{d}^3\mathbf{r} = \delta_{\mathbf{k}\mathbf{k}'}. \tag{2.14}$$

Here we limit ourselves to closed systems following Ref. [96]. For open systems the modal representation has been developed in Ref. [97]. It is assumed that the permittivity $\varepsilon(\mathbf{r})$ is real, and does not depend upon ω. The electric field can then expressed as a superposition of the modes as

$$\mathbf{E}(\mathbf{r}; \omega) = \sum_\mathbf{k} c_\mathbf{k} \mathbf{u}_\mathbf{k}(\mathbf{r}, \omega_\mathbf{k}) \tag{2.15}$$

where the coefficients $c_\mathbf{k}$ are determined from the initial and boundary conditions. The spectrum of modes $\mathbf{u}_\mathbf{k}$ is assumed to be discrete. For a continuous spectrum, the summation in Eq. (2.15) has to be replaced by an integral.

The Green function as described in Sec. 2.2 and the modal representation are alternative formalisms of representing the solution of the same wave equation. The Green function itself can be expanded as a superposition of the modes $\mathbf{u}_\mathbf{k}$

$$\overset{\leftrightarrow}{\mathbf{G}}(\mathbf{r}, \mathbf{r}'; \omega) = \sum_\mathbf{k} \mathbf{A}_\mathbf{k}(\mathbf{r}', \omega) \mathbf{u}_\mathbf{k}(\mathbf{r}, \omega_{\mathbf{k}'}) \tag{2.16}$$

with coefficients $\mathbf{A}_\mathbf{k}(\mathbf{r}', \omega)$ to be determined. Substituting Eq. (2.16) into Eq. (2.9)

$$\sum_\mathbf{k} \mathbf{A}_\mathbf{k}(\mathbf{r}', \omega)(\omega_\mathbf{k}^2 - \omega^2) \varepsilon(\mathbf{r}) \mathbf{u}_\mathbf{k}(\mathbf{r}) = c^2 \delta(\mathbf{r} - \mathbf{r}') \overset{\leftrightarrow}{\mathbf{I}}. \tag{2.17}$$

Multiplying on both sides of Eq. (2.17), by $\mathbf{u}_\mathbf{k}^*(\mathbf{r})$, using the orthonormality condition of the modes in Eq. (2.14), and integrating over the entire region $\mathbf{r}$

$$(\omega_\mathbf{k}^2 - \omega^2) \mathbf{A}_\mathbf{k}(\mathbf{r}', \omega) = c^2 \mathbf{u}_\mathbf{k}^*(\mathbf{r}'). \tag{2.18}$$

Using the mathematical identity [98]

$$\lim_{\eta\to 0^+}\frac{1}{x+\mathrm{i}\eta}=\mathrm{P}\left[\frac{1}{x}\right]-\mathrm{i}\pi\delta(x), \tag{2.19}$$

where P represents the principal value, the coefficients $\mathbf{A}_\mathbf{k}(\mathbf{r}',\omega)$ can now be expressed as

$$\mathbf{A}_\mathbf{k}(\mathbf{r}',\omega)=c^2\mathbf{u}^*_\mathbf{k}(\mathbf{r}')\left\{\mathrm{P}\left[\frac{1}{\omega^2_\mathbf{k}-\omega^2}\right]+\frac{i\pi}{2\omega_\mathbf{k}}\delta(\omega-\omega_\mathbf{k})-\frac{i\pi}{2\omega_\mathbf{k}}\delta(\omega+\omega_\mathbf{k})\right\}. \tag{2.20}$$

The contribution from the third term on the right hand side of Eq. (2.20) is neglected as only positive frequencies are considered. Substituting Eq. (2.20) into Eq. (2.16) the relationship between the Green function formalism and the eigenmodes formalism is established,

$$\overset{\leftrightarrow}{\mathbf{G}}(\mathbf{r},\mathbf{r}';\omega)=c^2\sum_\mathbf{k}\mathbf{u}^*_\mathbf{k}(\mathbf{r}',\omega_\mathbf{k})\mathbf{u}_\mathbf{k}(\mathbf{r},\omega_\mathbf{k})\left\{\mathrm{P}\left[\frac{1}{\omega^2_\mathbf{k}-\omega^2}\right]+\frac{i\pi}{2\omega_\mathbf{k}}\delta(\omega-\omega_\mathbf{k})\right\}, \tag{2.21}$$

which is usually simplified to

$$\overset{\leftrightarrow}{\mathbf{G}}(\mathbf{r},\mathbf{r}';\omega)=\sum_\mathbf{k}\frac{\mathbf{u}^*_\mathbf{k}(\mathbf{r}',\omega_\mathbf{k})\mathbf{u}_\mathbf{k}(\mathbf{r},\omega_\mathbf{k})}{(\omega^2_\mathbf{k}-\omega^2)/c^2} \tag{2.22}$$

where $\mathbf{u}^*_\mathbf{k}(\mathbf{r}',\omega_\mathbf{k})\mathbf{u}_\mathbf{k}(\mathbf{r},\omega_\mathbf{k})$ represents the direct product. Eq. (2.22) is important because it allows us to express the Green function in terms of the modes of the structure.

2.4 Quantum mechanical theory of spontaneous emission.

Spontaneous emission is a quantum mechanical process, through which an atom spontaneously decays from its excited state to the ground state while emitting a photon. Here, the aim is to study the dependence of the rate of spontaneous emission (γ) on the electromagnetic environment of the atom. The atom is described by a two level quantum mechanical system with the ground state $|g\rangle$ and the excited state $|e\rangle$ with energy difference $(E_e-E_g)=\hbar\omega_0$ where, ω_0 is the transition frequency and $\hbar$ is Planck's constant. Only two levels are considered and the effect of the other energy levels is neglected.

The Jaynes-Cummings Hamiltonian [99] of the *atom + field* system describes the interaction of the atom with the electromagnetic field. For a two level atom, in the rotating wave approximation, the atom field interaction is described by the minimal coupling Hamiltonian [6, 100, 101]

$$\hat{\mathcal{H}} = \hat{\mathcal{H}}_{Atom} + \hat{\mathcal{H}}_{Field} + \hat{\mathcal{H}}_{int} \tag{2.23}$$

where $\hat{\mathcal{H}}_{Atom} + \hat{\mathcal{H}}_{Field}$ is the unperturbed Hamiltonian of the *atom + field*, and the interaction Hamiltonian is $\hat{\mathcal{H}}_{int}$. Only the weak coupling regime between the emitter and the environment is considered, implying that the matrix elements of the interaction Hamiltonian $\hat{\mathcal{H}}_{int}$ are small compared to those of the unperturbed Hamiltonian. In the (electric-) dipole approximation $\hat{\mathcal{H}}_{int} = -\hat{\boldsymbol{\mu}} \cdot \hat{\mathbf{E}}$. The electric field operator $\hat{\mathbf{E}}$ and the dipole moment operator $\hat{\boldsymbol{\mu}}$ are

$$\hat{\mathbf{E}} = \sum_{\mathbf{k}} \sqrt{\frac{\hbar\omega_{\mathbf{k}}}{2\varepsilon_0}} \left[\mathbf{u}_{\mathbf{k}}(\mathbf{r})\hat{a}_{\mathbf{k}}(t) + \mathbf{u}^*_{\mathbf{k}}(\mathbf{r})\hat{a}^\dagger_{\mathbf{k}}(t) \right], \tag{2.24}$$

$$\hat{\boldsymbol{\mu}} = \boldsymbol{\mu}\Big[\, |e\rangle\langle g| + |g\rangle\langle e| \,\Big]. \tag{2.25}$$

The summation is over all modes $\mathbf{u}_{\mathbf{k}}$ of the system as in Eqs. (2.13), (2.14). $\boldsymbol{\mu}$ is the transition dipole moment, $\mathbf{r}$ is the location of the emitter, $\hat{a}_{\mathbf{k}}(\hat{a}^\dagger_{\mathbf{k}})$ is the single photon annihilation(creation) operator of the mode $\mathbf{k}$ with mode frequency $\omega_{\mathbf{k}}$. In the rotating wave approximation that is, neglecting the effect of other transitions and of counter rotating terms, the full Hamiltonian is

$$\hat{\mathcal{H}} = \Big(E_g|g\rangle\langle g| + E_e|e\rangle\langle e|\Big) + \sum_{\mathbf{k}} \hbar\omega_{\mathbf{k}} \left(\hat{a}^\dagger_{\mathbf{k}}\hat{a}_{\mathbf{k}} + \frac{1}{2}\right) + \hbar \sum_{\mathbf{k}} \Big(g_{\mathbf{k}}(\mathbf{r})\hat{a}^\dagger_{\mathbf{k}}|g\rangle\langle e| + g^*_{\mathbf{k}}(\mathbf{r})|e\rangle\langle g|\hat{a}_{\mathbf{k}}\Big). \tag{2.26}$$

with the dipolar atom-field coupling constant

$$g_{\mathbf{k}} = -i\frac{\omega_0}{\hbar}\sqrt{\frac{\hbar}{2\varepsilon_0\omega_{\mathbf{k}}}}\boldsymbol{\mu} \cdot \mathbf{u_k}^*(\mathbf{r}). \tag{2.27}$$

which depends upon the eigenmodes $\mathbf{u}_{\mathbf{k}}$ of the cavity, that is, on the environment.

We consider in the initial state the atom is its excited state with no photons present, in the final state the atom decays to its ground state while emitting a photon into mode $\mathbf{u}_{\mathbf{k}}$. The initial state $|i\rangle$ and final state $|f\rangle$ of the atom and field are thus defined as

$$|i\rangle = |e, \{0\}\rangle \;=\; |e\rangle|\{0\}\rangle \tag{2.28}$$

$$|f\rangle = |g, \{1_{\omega_{\mathbf{k}'}}\}\rangle \;=\; |g\rangle|\{1_{\omega_{\mathbf{k}'}}\}\rangle \tag{2.29}$$

respectively, $|\{0\}\rangle$ is the zero-photon state, and $|\{1_{\omega_{\mathbf{k}'}}\}\rangle$ is the one-photon state associated with the mode $\mathbf{k}'$. The Hamiltonian in Eq. (2.26) along with the Schrödinger wave equation

$$i\hbar\frac{d}{dt}|\psi\rangle = \hat{\mathcal{H}}|\psi\rangle \tag{2.30}$$

can be used to describe the time evolution of the system. The wave function of the system $|\psi\rangle$ can be written as a superposition of the initial state $|i\rangle$ and the final state $|f\rangle$,

$$|\psi(t)\rangle = C_0^e(\mathbf{r},t)|i\rangle + \sum_{\mathbf{k}} C_{1\mathbf{k}}^g(\mathbf{r},t)e^{-i\omega_{\mathbf{k}}t}|f\rangle. \tag{2.31}$$

$C_0^e(\mathbf{r},t)$, $C_{1\mathbf{k}}^g(\mathbf{r},t)$ are the associated amplitudes with initial conditions $C_0^e(t) = 1$ and $C_{1\mathbf{k}}^g = 0$. In the Wigner-Weiskopf approximation (WWA) [3] a solution of the form

$$C_0^e(\mathbf{r},t) = C_0^e(\mathbf{r},t)e^{-i\left(\omega_0+\Delta\omega-i\frac{\gamma}{2}\right)t} \tag{2.32}$$

is found for Eq. (2.30) by inserting Eq. (2.31) into Eq. (2.30) where γ is the rate of spontaneous emission and $\Delta\omega$ is the Lamb shift which relates to the frequency shift of the atom. In the WWA the frequencies are close to the atomic transition frequency $\omega \approx \omega_0$ and the solution to the Schrödinger equation (Eq. (2.30)) is [102, 103],

$$\Delta\omega(\mathbf{r},\omega) - i\frac{\gamma}{2}(\mathbf{r},\omega) = \frac{\omega|\boldsymbol{\mu}|^2}{2\hbar\varepsilon_0}\sum_{\mathbf{k}}\left[\frac{\omega}{\omega_{\mathbf{k}}}\frac{|\boldsymbol{\mu}\cdot\mathbf{u}_{\mathbf{k}}(\mathbf{r})|^2}{\omega-\omega_{\mathbf{k}}} - i\pi|\boldsymbol{\mu}\cdot\mathbf{u}_{\mathbf{k}}(\mathbf{r})|^2\delta(\omega-\omega_{\mathbf{k}})\right] \tag{2.33}$$

Thus, it is found again that the spontaneous emission rate γ depends on the available modes $\mathbf{u}_{\mathbf{k}}(\mathbf{r})$ at the location $\mathbf{r}$ of the emitter.

2.4.1 Local density of states and Green function

In order to relate the rate of spontaneous emission γ to the eigenmodes $\mathbf{u}_{\mathbf{k}}$ of the structure, the concept of partial local density of states (PLDOS) was introduced in Ref. [4]. If an emitter is located at $\mathbf{r}_0$ with a transition frequency ω_0 then the rate of spontaneous emission is expressed

$$\gamma = \frac{\pi\omega_0}{3\hbar\varepsilon_0}|\boldsymbol{\mu}|^2\rho_\mu(\mathbf{r}_0,\omega_0) \tag{2.34}$$

where $\rho_\mu(\mathbf{r},\omega_0)$ is the PLDOS and ω_0 is the frequency of emission of the atom. The PLDOS $\rho_\mu(\mathbf{r},\omega_0)$ is related to the modes $\mathbf{u}_{\mathbf{k}}$ as

$$\rho_\mu(\mathbf{r}_0,\omega_0) = 3\sum_{\mathbf{k}}[\mathbf{n}_\mu\cdot\mathbf{u}_{\mathbf{k}}(\mathbf{r}_0,\omega_{\mathbf{k}})\mathbf{u}_{\mathbf{k}}^*(\mathbf{r}_0,\omega_{\mathbf{k}})\cdot\mathbf{n}_\mu]\delta(\omega_0-\omega_{\mathbf{k}}) \tag{2.35}$$

where $\mathbf{n}_\mu$ is the unit vector along the direction of the transition dipole moment. In Eq. (2.35) the presence of the delta function restricts the mode frequencies close to the transition frequency $\omega_{\mathbf{k}}$. In quantum mechanical systems usually the orientation of the dipole moment $\mathbf{n}_\mu$ is not fixed and the PLDOS has to be averaged over the orientations of the dipole. The orientational average of the PLDOS is referred to as the local density of states (LDOS).

As shown previously in Eq. (2.22), the modal representation is related to the Green function and hence the PLDOS (Eq. (2.35)) and the LDOS can also be expressed using the Green function. There are two reasons to describe the LDOS and spontaneous emission using the Green function formalism. First, the Green function formalism is more versatile and valid for a open or closed systems, with losses. Although the modal representation can be extended to open systems [97], the Green function approach does not impose any conditions on the set of eigenmodes. Secondly, and more relevant to this work, is that the Green function is the solution of a point dipole and later (Sec. 2.7) is the natural way to study the LDOS with classical dipoles.

From Eq. (2.21) it can be shown that the imaginary part of the Green function is

$$\mathrm{Im}\Big\{\overleftrightarrow{\mathbf{G}}(\mathbf{r}_0, \mathbf{r}_0; \omega_0)\Big\} = \frac{\pi c^2}{2\omega_0}\sum_{\mathbf{k}} \mathbf{u}^*_{\mathbf{k}}(\mathbf{r}_0, \omega_{\mathbf{k}})\mathbf{u}_{\mathbf{k}}(\mathbf{r}_0, \omega_{\mathbf{k}})\delta(\omega_0 - \omega_{\mathbf{k}}). \tag{2.36}$$

This allows us to express the PLDOS (Eq. (2.34)) and the rate of spontaneous emission in terms of the Green function

$$\rho_\mu(\mathbf{r}_0, \omega_0) = \frac{6\omega_0}{\pi c^2}\Big[\mathbf{n}_\mu \cdot \mathrm{Im}\Big\{\overleftrightarrow{\mathbf{G}}(\mathbf{r}_0, \mathbf{r}_0; \omega_0)\Big\} \cdot \mathbf{n}_\mu\Big] \tag{2.37}$$

The LDOS is obtained by averaging PLDOS over the orientations of dipole moment $\mathbf{n}_\mu$. In terms of the Green function

$$\rho(\mathbf{r}_0, \omega_0) = \frac{2\omega_0}{\pi c^2}\mathrm{Im}\Big\{\mathrm{Tr}[\overleftrightarrow{\mathbf{G}}(\mathbf{r}_0, \mathbf{r}_0; \omega_0)]\Big\} \tag{2.38}$$

where Tr denotes the trace of the 3×3 Green tensor such as the one seen previously in Eq. (2.8).

For vacuum, the Green function is [5]

$$\overleftrightarrow{\mathbf{G}}(\mathbf{r}, \mathbf{r}'; \omega) = \mathrm{P}\Big[k^2\overleftrightarrow{\mathbf{I}} + \nabla\nabla\Big]\frac{\exp(\mathrm{i}kR)}{4\pi\varepsilon_0 R} - \frac{\overleftrightarrow{\mathbf{I}}}{3\varepsilon_0}\delta(\mathbf{r} - \mathbf{r}') \tag{2.39}$$

where $R = |\mathbf{r} - \mathbf{r}'|$. As seen in Eq. (2.38), for LDOS calculation the imaginary part of the Green function is required, with the source position also being observation that is

$\mathbf{r}' = \mathbf{r} = \mathbf{r}_0$. When $\mathbf{r} = \mathbf{r}'$, the real part of the Green function diverges, in the limit $R \to 0$. However, the imaginary part remains finite [104]

$$\lim_{R\to 0} \mathrm{Im}[\overset{\leftrightarrow}{\mathbf{G}}(\mathbf{r}, \mathbf{r}'; \omega)] = \frac{k}{6\pi}\overset{\leftrightarrow}{\mathbf{I}}. \tag{2.40}$$

Substituting Eq. (2.40) into Eq. (2.38) the LDOS for vacuum ρ_0 is

$$\rho_0 = \frac{\omega_0^2}{\pi^2 c^3} \tag{2.41}$$

and the decay rate in vacuum is

$$\gamma_0 = \frac{\omega_0^3 |\boldsymbol{\mu}|^2}{3\pi\varepsilon_0 \hbar c^3}. \tag{2.42}$$

From Eq. (2.38) in conjunction with Eq. (2.34), it is clear that the rate of spontaneous emission depends upon two factors: the magnitude and orientation of the transition dipole moment $\boldsymbol{\mu}$ and the imaginary part of the Green function. The transition dipole moment is assumed to be unaffected by the environment hence, the effect of the electromagnetic environment on the rate of spontaneous emission is contained within the Green function. A more detailed approach from the quantum electrodynamical point of view on the role of Green function and decay rate can be found in Refs. [105–107]. Having established that the spontaneous emission rate is affected by the environment we can now proceed to define a figure of merit which allows us to quantify the effect.

2.5 Purcell factor

In Sec. 2.4, it was discussed that the decay rate of an emitter depends upon the mode structure. Consequently, the rate of spontaneous emission is modified upon modification of the modes, as in a cavity. This modification of the rate of spontaneous emission was first postulated by Purcell for a single mode cavity [1]. To characterize the change in decay rate a figure of merit is defined, which is the ratio of the rate of spontaneous emission in a structure (γ) to that in vacuum (γ_0) and is called the Purcell factor (F)

$$F \equiv \frac{\gamma}{\gamma_0}. \tag{2.43}$$

In the Green function representation the Purcell factor is

$$F \equiv \frac{\gamma}{\gamma_0} = \frac{\hat{\mathbf{n}}_\mu \cdot \mathrm{Im}[\overset{\leftrightarrow}{\mathbf{G}}(\mathbf{r}_0, \mathbf{r}_0; \omega_0)] \cdot \hat{\mathbf{n}}_\mu}{\hat{\mathbf{n}}_\mu \cdot \mathrm{Im}[\overset{\leftrightarrow}{\mathbf{G}}^{(0)}(\mathbf{r}_0, \mathbf{r}_0; \omega_0)] \cdot \hat{\mathbf{n}}_\mu} \tag{2.44}$$

where γ, γ_0 are the rates of spontaneous emission in the medium and vacuum respectively, $\overset{\leftrightarrow}{\mathbf{G}}(\mathbf{r}_0, \mathbf{r}_0; \omega)$ is the Green function in the medium, and $\overset{\leftrightarrow}{\mathbf{G}}^{(0)}(\mathbf{r}_0, \mathbf{r}_0; \omega)$ is the Green function in vacuum. Without the loss of generality, if it is assumed that the dyadic Green $\overset{\leftrightarrow}{\mathbf{G}}$ function is expressed in the cartesian coordinates and the transition dipole moment is oriented along $\hat{\mathbf{z}}$, Eq. (2.44) is recast as

$$F = \frac{\mathrm{Im}\{\mathbb{G}_{zz}\}}{\mathrm{Im}\{\mathbb{G}_{zz}^{(0)}\}} \tag{2.45}$$

where $\mathbb{G}_{zz}$ represents the $\hat{\mathbf{z}}\hat{\mathbf{z}}$ component of the dyad $\overset{\leftrightarrow}{\mathbf{G}}(\mathbf{r}_0, \mathbf{r}_0; \omega_0)$.

Apart from losing energy through spontaneous emission, emitting a photon, a molecule in an excited state can also lose energy non-radiatively for example, dissipating energy into heat. In a realistic system the decay rate γ of a fluorescent molecule would be influenced by both radiative and non-radiative decay channels. The apparent quantum yield η is then,

$$\eta = \frac{\gamma^R}{\gamma^{NR} + \gamma^R} \tag{2.46}$$

where γ^R is the radiative decay rate, γ^{NR} is the non-radiative decay rate which contains the internal losses within the emitter and the losses in the environment. The Purcell factor Eq. (2.43) can also be decomposed into its radiative and non-radiative components

$$F \equiv \frac{\gamma}{\gamma_0} = \frac{\gamma^R + \gamma^{NR}}{\gamma_0} = F^R + F^{NR} \tag{2.47}$$

where F^R is the radiative Purcell factor, while F^{NR} is the non radiative Purcell factor. A similar decomposition of the radiative and non-radiative LDOS can also be obtained [108].

2.6 Classical theory of radiation

Expressing the LDOS and Purcell factor in terms of the Green function, becomes useful when we study the radiation by a classical dipole. Let a harmonically oscillating, classical, electric dipole, with a classical dipole moment $\mathbf{p}$, be located at the position $\mathbf{r}_0$. The power radiated P by the dipole to its environment. For a dipolar current source the power radiated is [5],

$$P = \frac{\omega}{2}\mathrm{Im}\{\mathbf{p}^* \cdot \mathbf{E}(\mathbf{r}_0)\}, \tag{2.48}$$

where $\mathbf{E}(\mathbf{r}_0)$ is the electric field evaluated at the position of the dipole. The classical Green formulation (Eq. (2.12)) can be used to compute the electric field $\mathbf{E}(\mathbf{r}_0)$ and obtain

$$P = \frac{\omega^3 \mu_0 |\mathbf{p}|^2}{2} \left[\hat{\mathbf{n}}_p \cdot \mathrm{Im}\{\overleftrightarrow{\mathbf{G}}(\mathbf{r}_0, \mathbf{r}_0; \omega)\} \cdot \hat{\mathbf{n}}_p \right] \tag{2.49}$$

where $\hat{\mathbf{n}}_\mathbf{p}$ is the unit vector in the direction of the dipole moment of $\mathbf{p}$. For vacuum, the imaginary part of the Green function can be substituted from Eq. (2.40) into Eq. (2.49) to obtain the well known expression for the power emitted by a dipole emitter in vacuum

$$P_0 = \frac{\omega^4}{12\pi\varepsilon_0 c^3} |\mathbf{p}|^2. \tag{2.50}$$

In the semi-classical approximation [26] the decay rate γ can be obtained by dividing the average power emitted by a classical dipole P by the energy of one photon, $\gamma = P/\hbar\omega_0$. The classical dipole moment $\mathbf{p}$ and the quantum mechanical dipole moment $\boldsymbol{\mu}$ are linearly related as $\mathbf{p} = 2\boldsymbol{\mu}$ [109]. In Eq. (2.50), substituting $\mathbf{p}$ by $\boldsymbol{\mu}$ and replacing ω by the transition frequency ω_0, and dividing the power by the energy of one photon $\hbar\omega_0$, the exact expression for the decay rate in Eq. (2.42) is recovered. The Purcell factor expressed using the modification of the decay rate (γ/γ_0) or the power emitted by a dipole (P/P_0) is identical

$$F \equiv \frac{\gamma}{\gamma_0} = \frac{P}{P_0} = \frac{6\pi c}{\omega_0} \left[\hat{\mathbf{n}}_p \cdot \mathrm{Im}\{\overleftrightarrow{\mathbf{G}}(\mathbf{r}_0, \mathbf{r}_0; \omega_0)\} \cdot \hat{\mathbf{n}}_p \right]. \tag{2.51}$$

Changing the electromagnetic environment modifies the rate of spontaneous emission the same way it modifies the power radiated by a classical point dipole. Thus, the Purcell factor can also be seen as the normalized power radiated by a classical dipole antenna.

2.7 Antenna impedance and Purcell factor.

In Sec. 2.6 it was demonstrated that the power radiated by a classical point dipole is modified the same way as the rate of spontaneous emission by a two level system (Eq. (2.51)). In principle it allows the characterization of the LDOS using classical dipoles. However, a point dipole is a theoretical concept, implying a perfect electromagnetic source localized at a point in space and thus not feasible to realize experimentally. Here we show that using finite, subwavelength antennas, the Purcell factor

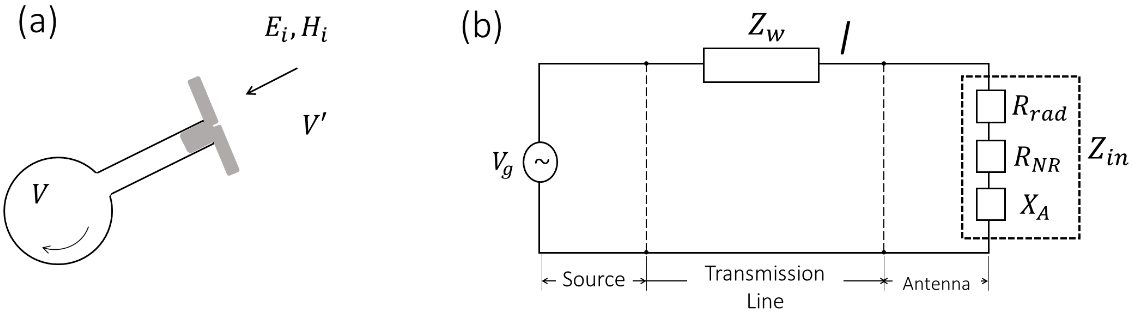

Figure 2.1: (a) Schematic of a dipole antenna, (b) equivalent circuit of dipole antenna attached to a coaxial cable of impedance Z_w.

can be measured experimentally. It is not a new idea and the first measurements were performed by Dowling [27, 31]. In this section we lay the theoretical foundations for measurement of the Purcell factor at microwave frequencies with antennas.

An antenna is a device which interacts with electromagnetic radiation, it can act as a receiver, as well as an emitter of electromagnetic waves. In more general terms an antenna is the interface which connects two volumes, V and V' as seen in Fig. 2.1(a). An opening in the volume V, connects to the antenna in Fig. 2.1(a) via a transmission line, usually a waveguide. The volume V is separated from volume V' via a perfectly conducting boundary shielding an electronic system. The electronic system dissipates incoming radiation through from V', and may contain the source that generates currents which are emitted to V' via the antenna.

The antenna system seen in Fig. 2.1(a) can be simplified into a lumped circuit model as shown in Fig. 2.1(b)[110]. Where the source V_g is a voltage source, the transmission line has an impedance Z_w. The important quantity is the input impedance Z_{in} of the antenna, which is the impedance presented by the antenna at its terminals. From the reciprocity principle, the circuit representation of the antenna is valid in the emitting mode as well as receiving mode of the antenna.

The input impedance can be decomposed into its constituents $Z_{in} = (R_{NR} + R_{rad}) - iX$ where R_{NR} is the non-radiative loss, R_{rad} is the radiative resistance, and X is the reactance. In this thesis the antennas considered are made of perfect electric conductors (PEC) and hence non-radiative losses in the antenna are negligible, that is, $R_{NR} \to 0$. The assumption is justified since the frequency of interest is in microwaves (5-15 GHz) and the antenna is made of copper which has negligible losses at these frequencies. The radiative resistance R_{rad} can be thought of as the magnitude of a fictitious resistance, when connected in series with an antenna, dissipates the same amount of power as much as the antenna radiates. R_{rad} not only depends upon the characteristics of the system, but also on the surrounding environment of the antenna, is well known in antenna theory [111]. The input impedance of a short sub-wavelength dipole antenna is analyzed next and its relation to the LDOS and the Purcell factor is presented.

2.7.1 Impedance of a subwavelength dipole antenna.

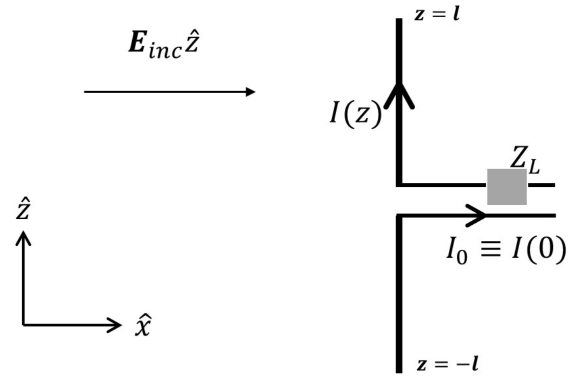

Figure 2.2: Schematic of a subwavelength dipole antenna with a load impedance Z_L.

A short dipole antenna (Fig. 2.2) is considered to be composed of two thin perfectly conducting wires along $\hat{\mathbf{z}}$, with a small gap at the center and loaded by a impedance Z_L. The arm length is denoted by l, with $l \ll \lambda$, where λ is the wavelength of operation. An electric field $E_z\hat{z}$ is incident upon the antenna, which induces a current along the length of the antenna. If the current at the center is denoted by $I_0 \equiv I(0)$ the current at a location z along the antenna arm is denoted by $I(z) = I_0 f_t(z)$ where $f_t(z)$ is [112]

$$f_t(z) = \frac{\sin k(l - |z|)}{\sin kl}, \tag{2.52}$$

and $k = 2\pi/\lambda$. Thus the current vanishes at the ends of the antenna ($f_t(z = \pm l) = 0$). In the long wavelength limit $kl \to 0$, $f_t(z)$ takes the takes the triangular form,

$$f_t(x) = 1 - \frac{|z|}{l}. \tag{2.53}$$

If the volume charge density is expressed as $\rho_q(z)$ then using the continuity condition,

$$\nabla \cdot \mathbf{j} = \frac{dI}{dz} = -\frac{\partial \rho_q'(z) e^{-i\omega t}}{\partial t} = i\omega\rho_q'(z) \tag{2.54}$$

where $\rho'_q = \rho_q/dxdy$. For such a thin wire system, the dipole moment can be expressed as $\mathbf{p} = p_z\hat{z}$ where,

$$p_z = \int_{-l}^{l} x\rho'_q(z)dz = -\frac{I_0 l}{i\omega}. \tag{2.55}$$

Thus the dipole moment is proportional to the current I_0.

If the voltage at the terminals is V_0, the input impedance Z_{in} is defined through a linear relationship between the voltage and the current $V_0 = Z_{in}I_0$. The input impedance is now calculated using Brillouin's induced electromotive force (IEMF) method [111]. The voltage induced at the center of the antenna is

$$V_0 = \int_{-l}^{l} dV = \frac{1}{I_0}\int_{-l}^{l} I(z')E_z(z')\, dz'. \tag{2.56}$$

and the input impedance is defined as,

$$Z_{in} = \frac{V_0}{I_0} = \frac{1}{I_0^2}\int_{-l}^{l} I(z')E_z(z')\, dz'. \tag{2.57}$$

For a short sub-wavelength antenna, the electric field $E_z(z')$ can be considered uniform over the length of the antenna and the current is assumed to be of the form in Eq. (2.53). Then, Eq. (2.57) simplifies to,

$$Z_{in} = \frac{E_z(\mathbf{r}_0)l}{2I_0} \tag{2.58}$$

where $\mathbf{r}_0$ is the location of the center of the antenna. Using the dipole moment obtained in Eq. (2.55) the field $E_z(\mathbf{r}_0)$ can be expressed using the Green function. Then from Eq. (2.58) the relationship between the Green function and the input impedance is

$$Z_{in} = \frac{(\mu_0\omega^2\overleftrightarrow{\mathbf{G}}(\mathbf{r}_0,\mathbf{r}_0;\omega)\cdot\mathbf{p})l}{2I_0} = \frac{(\mu_0\omega^2\mathbb{G}_{zz}(\mathbf{r}_0,\mathbf{r}_0;\omega))l}{2I_0}\left(-\frac{I_0 l}{i\omega}\right). \tag{2.59}$$

Re-arranging Eq. (2.59),

$$Z_{in} = \frac{(\mu_0 l^2)}{2}\Big[(i\omega)\mathbb{G}_{zz}(\mathbf{r}_0,\mathbf{r}_0;\omega)\Big] \tag{2.60}$$

From the expression in Eq. (2.60) it is clear that the real part of the input impedance Z_{in} corresponds to the imaginary part of the impedance $\overleftrightarrow{\mathbf{G}}(\mathbf{r}_0,\mathbf{r}_0;\omega)$. Substituting Eq. (2.60) into Eq. (2.45) the Purcell factor is obtained from the impedance [32]

$$F = \frac{\text{Re}\,\{Z_{in}\}}{\text{Re}\,\{Z_{in}^{(0)}\}} = \frac{\text{Im}\{\mathbb{G}_{zz}\}}{\text{Im}\{\mathbb{G}_{zz}^{(0)}\}}. \tag{2.61}$$

where $Z_{in}^{(0)}$ is the input impedance of the antenna in free space. Eq. (2.61) is a central result to this thesis. It shows that the real part of the input impedance of a short dipole antenna corresponds to the imaginary part of the Green function. The representation of the Purcell factor through the antenna impedance of an antenna is very useful because, at microwave frequencies input impedance is a quantity that can be measured directly. It allows us to measure the Purcell factor with an antenna, rather than measuring decay rates of fluorescent emitters.

2.8 Equivalent circuit model for Purcell effect.

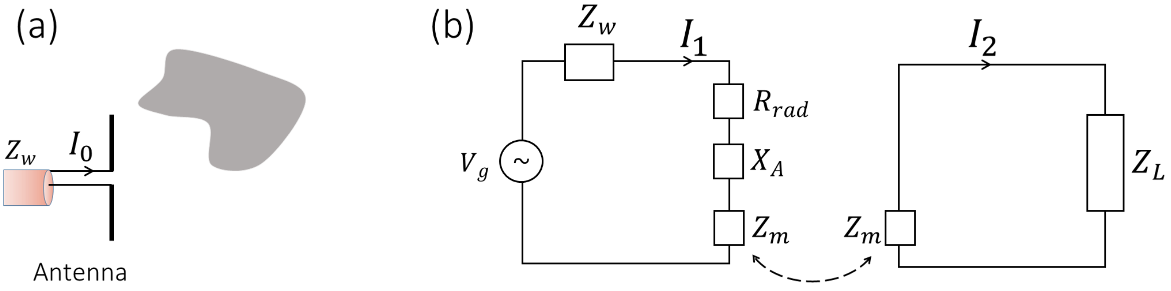

Figure 2.3: (a) Schematic of a dipole antenna near an object, (b) equivalent circuit model of harmonic dipole in presence of an object.

The Purcell factor can also be analyzed using lumped circuit models. Recalling the circuit representation of an antenna from Fig. 2.1(b), if the dissipative losses are negligible $R_{NR} \to 0$ the radiative resistance can be approximated by the real part of the input impedance $\mathrm{Re}\{Z_{in}\} \approx R_{rad}$. From Kirchoff's law the current flowing in the circuit is

$$I = V_g/(Z_w + R_{rad} - \mathrm{i}X_A). \tag{2.62}$$

If in free space the input impedance is denoted by $Z_{in}^{(0)}$ and the radiative resistance as $R_{rad}^{(0)}$ with $\mathrm{Re}\{Z_{in}^{(0)}\} = R_{rad}^{(0)}$, the presence of another object can be seen as the addition of a mutual impedance, which changes the input impedance to $Z_{in} = Z_{in}^{(0)} + Z_m$ as seen in Fig. 2.3. It is important to note that for a short dipole antenna the radiation resistance is very small compared to the impedance of the transmission line, $R_{rad} \ll Z_w$. It is a very important concept for the development of antenna based models for Purcell factor. To provide a rough estimate, assume a dipole antenna of length $l = 0.1\lambda$ is attached to a coaxial cable of impedance Z_w=50 Ω. The radiation resistance of such a short dipole antenna is given by [111]

$$R_{rad} = 20\pi^2 \left(\frac{l}{\lambda}\right)^2 \quad \Omega, \tag{2.63}$$

which yields a value of $R_{rad} = 1.97~\Omega$, which is much smaller than the reference impedance of the waveguide 50 Ω. Thus, the addition of the mutual impedance, of a magnitude similar to R_{rad}, does not change the current flowing (Eq. (2.62)) in the circuit significantly. This allows us to express the Purcell factor using only the impedances [33],

$$F = \frac{\mathrm{Re}\{~Z_{in}\}}{\mathrm{Re}\{Z_{in}^{(0)}\}} = 1 + \frac{\mathrm{Re}\{Z_m\}}{\mathrm{Re}\{Z_{in}^{(0)}\}}. \tag{2.64}$$

The Purcell factor can increase or decrease, depending upon the nature of the mutual impedance Z_m. In this discussion, the mutual coupling Z_m is not analyzed in any specific details. Rather, the aim is to present a general approach for an arbitrary electromagnetic environment. The reader is referred to the Refs. [32, 33] for more details on the role of mutual coupling and the Purcell factor.

2.9 Electric and magnetic Purcell factor.

The Green function $\overset{\leftrightarrow}{\mathbf{G}}(\mathbf{r}, \mathbf{r}'; \omega)$ used until now is the solution of wave equation for a point electric dipole source, which relates the electric field to the electric dipole moment (Eq. (2.12)), leading to the expression of the Purcell factor (Eq. (2.45)). An analogous concept of the magnetic Purcell factor can be derived using the magnetic Green function [113, 114]. In the context of antennas a small magnetic loop antenna can act as a magnetic dipole. The magnetic Purcell factor can similarly be obtained by a measurement of the input impedance of a magnetic loop antenna [34, 92]

$$F^{e/m} = \frac{\mathrm{Im}\{\mathbb{G}_{zz}^{e/m}\}}{\mathrm{Im}\{\mathbb{G}_{zz}^{e/m,(0)}\}} = \frac{\mathrm{Re}\{Z_{in}^{e/m}\}}{\mathrm{Re}\{Z_{in}^{e/m,(0)}\}}. \tag{2.65}$$

where $F^{e/m}$ denotes the electric/magnetic Purcell factors obtained for an electric/magnetic dipole. This concept has not been given much attention as the atom field coupling is generally electric dipolar in nature and only recently the concept has gained recent attention optics [35].

2.10 Theory of microwave measurements.

As this thesis focuses on studying radiation dynamics at microwave frequencies with antennas, in this section we describe the basic theory of microwave measurements. The aim is to familiarize the reader with the basic concepts such as scattering parameters (S-parameters) and impedance parameters (Z-parameters) to analyze microwave networks.

Microwave networks have been studied extensively theoretically [115] and experimentally [116]. A microwave network consists of a device under test (DUT) which can have any number of “ports". Excitation and taking measurement of the DUT can only occur through the ports. Usually the energy is fed through radio frequency (RF) waves by a transmission line. There can be any number of ports, ranging from 1 to N, with or without coupling between the ports. Here, we shall only consider linear coupling between the ports and the DUT. The objective in microwave measurements is to characterize the response of the DUT, through its response at the ports.

Here, we present two ways through which microwave networks can be described, the impedance parameters (Z-parameters) and the scattering parameters (S-parameters). They are equivalent representations and the preferred choice depends upon the type of problem. We apply it to the two most widely studied microwave networks, the one-port network and the two-port network. The one-port network is the simplest of all cases, where the network has only one port. In this case the entire system is characterised by measuring the reflection coefficient. We then outline how measurement of the Purcell factor through using an antenna can be seen as measurement of one port network. More generalized two-port networks are analyzed next. Two-port networks are relevant for measurements of resonance energy transfer. This section will build the requisite background to understand the experimental results in later Chapters 3, 5.

2.10.1 One port network

A one port network as the name suggests has only one port, as illustrated in Fig. 2.4. Consider for example a transmission line with a reference impedance Z_w terminated by a load Z. For simplicity we assume that the transmission line is a coaxial waveguide supporting a single transverse electric and magnetic (TEM) mode. The system is completely described by the voltage between the conducting terminals and the current

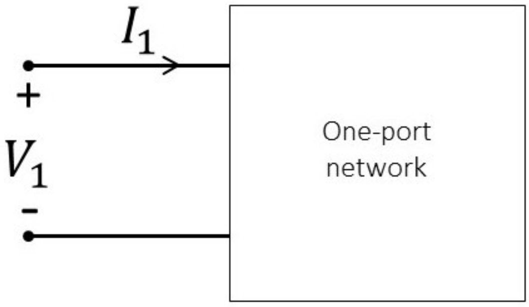

Figure 2.4: Schematic of a one port network.

flowing through the conductor in the transmission line. If the load Z is not perfectly matched with the transmission line, then a component of the waves at the load would be reflected. Hence we can decompose the current I and the voltage V as a superposition of the incident and reflected wave

$$V = V_i + V_r, \tag{2.66}$$

where V_i is the amplitude of voltage of the incident wave, V_r is the amplitude of the voltage of the reflected wave, the harmonic time dependence is implicit. The current I can be similarly decomposed as

$$I = I_i - I_r, \tag{2.67}$$

where I_i is the amplitude of current of the incident wave, I_r is the amplitude of the current of the reflected wave. The negative sign for the reflected current denotes that the current is reflected back from the load impedance Z. The reference impedance of the transmission line is defined as,

$$Z_w = \frac{V_i}{I_i} = \frac{V_r}{I_r}. \tag{2.68}$$

Substituting Eq. (2.68) in Eq. (2.67) the current is

$$I = \frac{1}{Z_w}(V_i - V_r). \tag{2.69}$$

If the reference plane is set at the terminals of the load Z and assuming a linear relationship between the current and voltage, the impedance of the load Z is

$$Z = \frac{V}{I}. \tag{2.70}$$

Substituting Eqs. (2.66), (2.69) into Eq. (2.70),

$$Z = Z_w \frac{1-\Gamma}{1+\Gamma} \tag{2.71}$$

where reflection coefficient Γ is defined as $\Gamma = V_r/V_i$. The reflection coefficient Γ is a commonly measured quantity in microwave measurements. Eq. (2.71) shows that in a one-port network the load impedance Z can be determined through a measurement of the reflection coefficient Γ, provided the reference impedance Z_w is known.

2.10.2 Antenna as a one-port network.

Consider the example of an antenna fed through a coaxial cable. We assume the coaxial cable is attached to a vector network analyzer (VNA). The VNA houses the electronics for the source, while at the same time it can measure the incoming and outgoing waves through the coaxial cable.

In such a system the reference impedance Z_w is determined by the type of waveguide, the impedance Z is determined by the input impedance Z_{in} of the antenna. The current that feeds the antenna terminals causes the antenna to radiate electromagnetic waves. Some of the waves would be reflected back at the antenna inducing a current in the antenna and influence the input impedance Z_{in} presented by the antenna. The environment changes the impedance of the antenna through the reflected fields (Eq. (2.71)). Thus, in principle the environment can also be characterized through the impedance. It is the measurement of the change in the impedance for a subwavelength antenna that provides the Purcell factor F as mentioned in Sec. 2.7.1.

The reference impedance of a coaxial cable is generally 50 Ω. The VNA can directly measure the impedance Z as the impedance parameter Z_{11}, where the subscript $_{11}$ denotes a one-port network. Alternatively as described in detail later in Sec. 2.10.4, the reflection coefficient Γ can be obtained as a measurement of scattering parameter S_{11} and substituted in Eq. (2.71) to obtain the impedance.

2.10.3 Two port network

A two port network (Fig. 2.5) is more general than a one-port network. As the name suggests the system consists of two input-output ports. A two-port network is the most exhaustively studied system in microwave measurement theory. While in one-port network the system could in principle be characterized using only one parameter: the reflection coefficient Γ (Eq. (2.71)), in a two port network the mutual coupling between the two ports has to be considered. That is, the current and voltage in port 1 can influence the current and voltage in port 2 and vice-versa.

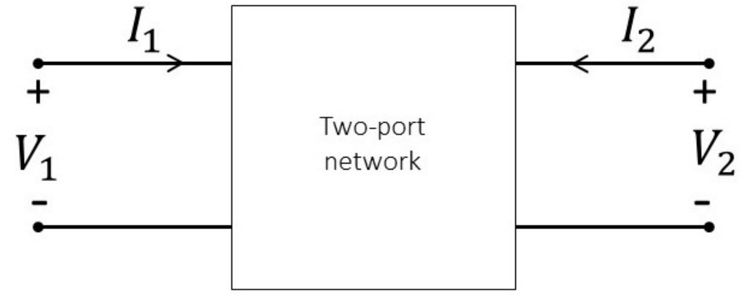

Figure 2.5: Schematic of a two port network in current and voltage representation.

Ports 1 and 2 have corresponding currents and voltages I_1, V_1, I_2, and V_2 associated with them. It is assumed that coupling between voltage and current is linear

$$[V] = [Z][I], \tag{2.72}$$

where $[V] = [V_1, V_2]^T$, $[I] = [I_1, I_2]^T$, and the impedance matrix

$$[Z] = \begin{bmatrix} Z_{11} & Z_{12} \\ Z_{21} & Z_{22} \end{bmatrix}. \tag{2.73}$$

The diagonal element Z_{ii} is the input impedance at port i if port j is open, that is no current is flowing in port j

$$Z_{ii} = \left.\frac{V_i}{I_i}\right|_{I_j=0}. \tag{2.74}$$

The off diagonal elements $Z_{ij \neq i}$, determine the coupling between the two ports. The impedance Z_{ij} is defined as the voltage induced at port i when port i is open [111],

$$Z_{ij} = \left.\frac{V_i}{I_j}\right|_{I_i=0} \qquad (i \neq j). \tag{2.75}$$

For a two-port network a knowledge of the elements of the impedance matrix $[Z]$ along with the reference impedances of the transmission lines characterize the entire system. Though we consider a system with only two-ports, the procedure can be extended to multi-port systems.

2.10.4 Scattering parameters (S-parameters)

Previously we studied the one-port and two-port networks from the linear relationship between the current and voltage obtained through the impedance parameters (Eq. (2.72)). An equivalent description in terms of the input and output waves at the two ports can also be formulated. It has to be pointed out that scattering parameters (S-parameters) and impedance parameters (Z-parameters) are equivalent representations and it is possible to convert one into the other [117].

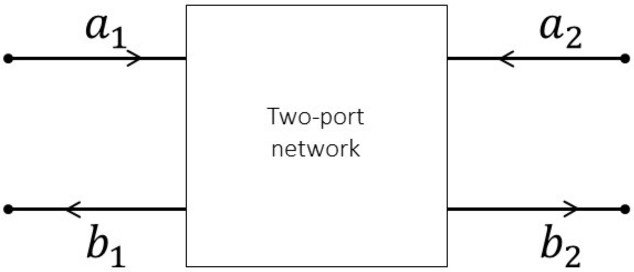

Figure 2.6: Two port network in S-parameter representation.

In the S-parameter representation, the input waves are denoted as a_1 and a_2 at ports 1 and 2 respectively. The output waves at ports 1 and 2 are denoted as b_1, b_2 respectively (Fig. 2.6). The parameters (a_1, a_2, b_1, b_2) could denote either the amplitudes of the current or the voltage of the waves. The input and output waves are linearly related as

$$[b] = [S][a], \tag{2.76}$$

where $[a] = [a_1, a_2]^T$, $[b] = [b_1, b_2]^T$, and the scattering matrix is

$$[S] = \begin{bmatrix} S_{11} & S_{12} \\ S_{21} & S_{22} \end{bmatrix}. \tag{2.77}$$

The diagonal elements S_{ii}, associated with the reflection coefficients are

$$S_{ii} = \left.\frac{b_i}{a_i}\right|_{a_j=0}. \tag{2.78}$$

The off diagonal elements are,

$$S_{ij} = \left.\frac{b_i}{a_j}\right|_{a_i=0} \qquad (i \neq j). \tag{2.79}$$

The one-port network can be seen as a special case with $a_2 = b_2 = 0$. From Eq. (2.78) and Eq. (2.79) the physical meaning of the S-parameters can be inferred. S_{11} is the reflection coefficient at port 1 when port 2 is terminated by a matched load. S_{21} is the transmission coefficient between ports 1 and 2 when port 2 is terminated in a perfectly matched load. S_{21} quantifies the signal that is transmitted from port 1 to port 2. This transmission property of scattering coefficient S_{21} will be useful for measurements of resonance energy transfer in Chapter 4.

2.11 Example: Purcell factor near a conducting interface

As an example to elucidate the effectiveness of using an antenna to probe the Purcell factor, we consider how a perfectly conducting interface influences the decay rates of emitters as the distance between the emitter and the interface is changed. While this was the first experiment which demonstrated the modification of decay rates of fluorescent emitters at optical frequencies [7], the same experiment was repeated at microwave frequencies using antenna impedance measurements [33]. At the same time in this simple geometry, analytical calculation of the Purcell factor is also possible. The example also exhibits the advantages of measuring the Purcell factor with antennas at microwave frequencies over conventional optics experiments.

Formulation of the problem.

Assuming a perfectly conducting plate in the x-y plane at $z = 0$ then, the problem is to determine how the decay rate of emitters change as a function of the distance z between the emitters and the conducting plate. The Purcell factor is proportional to the imaginary part of the Green function. The Green function near such a conducting $\overset{\leftrightarrow}{\mathbf{G}}(\mathbf{r}, \mathbf{r}'; \omega)$ interface can be expressed as a superposition of the Green function in vacuum $\overset{\leftrightarrow}{\mathbf{G}}^{(0)}(\mathbf{r}, \mathbf{r}'; \omega)$ (Eq. (2.39)) [2]

$$\overset{\leftrightarrow}{\mathbf{G}}(\mathbf{r}, \mathbf{r}'; \omega) = \overset{\leftrightarrow}{\mathbf{G}}^{(0)}(\mathbf{r}, \mathbf{r}'; \omega) - \overset{\leftrightarrow}{\mathbf{G}}^{(0)}(\rho, z + z', \rho', 0; \omega) + 2\overset{\leftrightarrow}{\mathbf{G}}^{(0)}_{zz}(\rho, z + z', \rho', 0; \omega)\hat{z}\hat{z} \quad (2.80)$$

where $\mathbf{r} = (x, y, z)$, $\mathbf{r}' = (x', y', z')$, $\rho = (x, y)$, $\rho' = (x', y')$, $\overset{\leftrightarrow}{\mathbf{G}}^{(0)}$ is the Green function in vacuum (Eq. (2.39)), and $\overset{\leftrightarrow}{\mathbf{G}}^{(0)}_{zz}$ is the $\hat{z}\hat{z}$ component of this Green function. The change in decay rate, which is the Purcell factor is proportional to the imaginary part (Eq. (2.44)) of the Green function. In this geometry, the Purcell factor is [7, 33],

$$F^{\perp} = 1 + 3\left(\frac{\sin(\eta)}{\eta^3} - \frac{\cos(\eta)}{\eta^2}\right), \quad (2.81)$$

$$F^{//} = 1 - \frac{3}{2}\left(\frac{\cos(\eta)}{\eta^2} + \left[\frac{1}{\eta} - \frac{1}{\eta^3}\right]\frac{\sin(\eta)}{\eta^2}\right), \tag{2.82}$$

where $F^{\perp}$ denotes the Purcell factor when the dipole moment of the emitter is oriented perpendicular to the conducting plane, $F^{//}$ is the Purcell factor when the dipole moment of the emitter is parallel to the conducting plane, and $\eta = 2kz$.

Measurement of Purcell factor at optical frequencies

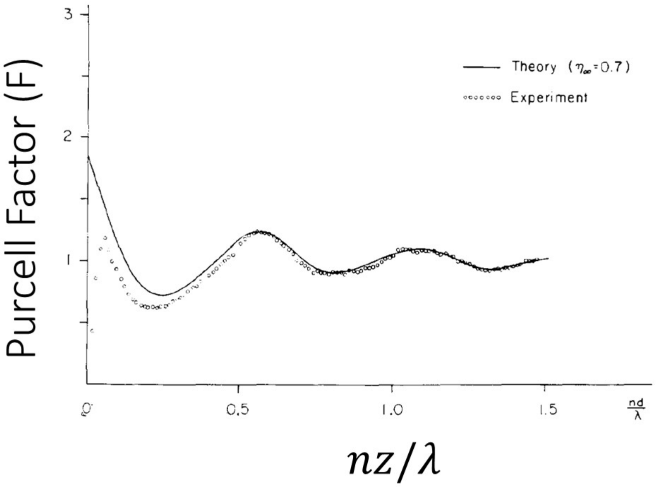

Figure 2.7: Modification of lifetimes of fluorescent molecules near a conducting mirror. (Source: Drexhage [7])

Change in decay rates of fluorescent molecules near a conducting interface at optical frequencies was reported by Drexhage [7]. The experiment was performed by characterizing the decay rates of Eu^{3+}-ion based fluorescent dye molecules close to a silver mirror. In order to precisely control the separation between the fluorescent molecules and the silver mirror, a number of layers of a fatty acid were deposited on top of the silver layer and then a monolayer of fluorescent molecules were deposited. The measurements were performed at a wavelength of 612 nm.

The results are shown in Fig. 2.7 with experiments indicated by the dots, and theoretical results, which neglect the competing non radiative decay channels by the solid curve. It is assumed that there is no preferred direction of the orientation of the dipole moments of the fluorescent molecules in the monolayer and the distribution of orientation of dipole moments is random. Hence the experiments are compared to theory by averaging the Purcell factor in the parallel and perpendicular directions (Eqs. (2.82), (2.81)), $\frac{1}{3}(F^{\perp} + 2F^{//})$.

Measurement of Purcell factor at microwave frequencies

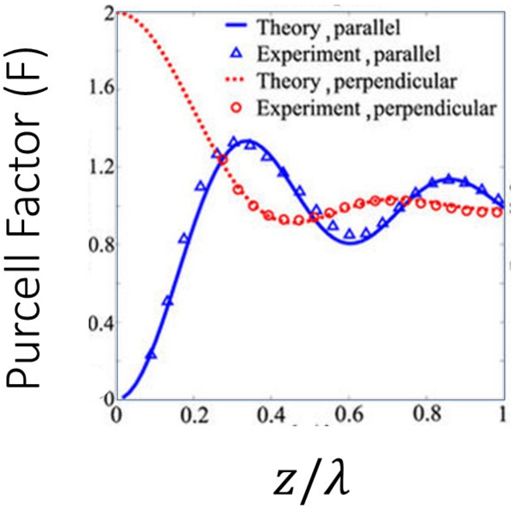

Figure 2.8: Purcell factor near a conducting plate at microwave frequencies for perpendicular (red) and parallel (blue) orientations of the antenna. (Source: Krasnok et al, [33])

The experiments performed by Drexhage were repeated in the microwave frequency range of 5-14 GHz which corresponds to a wavelength range 2.1 cm to 6.0 cm [33]. The Purcell factor is proportional to the real part of the input impedance of a subwavelength antenna (Eq. (2.61)). In this experiment, the impedance was obtained by measuring the scattering coefficient (Sec. 2.10.2) of the antenna near a large copper plate. Copper has negligible losses in the aforementioned frequency range hence non-radiative quenching can be neglected.

The Purcell factor with an antenna was measured for the perpendicular and parallel orientations of the antenna and compared with theoretical Purcell factor from Eqs. (2.82), (2.81). The results are shown in Fig. 2.8. Note that with an antenna it is possible to resolve the orientational dependence of the Purcell factor in the parallel and perpendicular directions of the dipole moment. It is an important advantage compared to measurements with an ensemble of fluorescent molecules, such as the experiment by Drexhage (Fig. 2.7), where the Purcell factor had to be averaged for comparison with experiments.

The aim of this chapter was to show the equivalence between the Purcell factor and the input impedance of an antenna. In the next chapter, we experimentally measure the antenna impedance, to obtain the electric and magnetic Purcell factor in a fishnet metamaterial at microwave frequencies. We show that we are able to discern the contribution of individual modes to the density of states, and gain a comprehensive understanding of the Purcell factor in the metamaterial.

Chapter 3

Purcell factor in a microwave fishnet hyperbolic metamaterial

In Chapter 2 we discussed that the Purcell factor is influenced by the electromagnetic environment. We showed that in the semi-classical approximation, by measuring the impedance of a subwavelength dipole antenna it is possible to find the Purcell factor. In this chapter we apply the methods developed in the previous Chapter 2 to study the Purcell factor numerically and experimentally in a microwave fishnet hyperbolic metamaterial. This chapter is based on the work published in Ref [92].

The fishnet metamaterial was designed to operate in the frequency range 5-15 GHz. The structure been previously proposed as a candidate for epsilon near zero (ENZ) metamaterial [118]. Due to the anisotropy, the metamaterial has different dispersion relations in transverse magnetic (TM_z) and transverse electric (TE_z) polarizations, which lead to distinct Purcell factors depending upon the polarization. The electromagnetic modes in the TM_z polarization have hyperbolic dispersion, which lead to an enhancement of the Purcell factor, while for the TE_z polarization, there are no propagating modes which reduces the Purcell factor. Thus, depending upon the orientation of the dipole antenna, both enhancement and suppression of the Purcell factor can be observed in the same structure.

The polarization dependence of the Purcell factor is confirmed when we analyze the band structure of periodic unit cell and numerically compute the density of states (DOS) of the available modes. The density of states is the spatial average of the LDOS in the periodic unit cell of the structure. We experimentally measure the electric and magnetic Purcell factor inside the structure, from impedance measurements antennas using the formalism developed in previous sections. Measurements are compared with finite difference time domain (FDTD) simulation of the Purcell factor. The aim of this chapter is to develop a coherent understanding of the electric and magnetic LDOS and Purcell factor, theoretically and experimentally in the hyperbolic metamaterial.

In Sec. (3.1) we present our fishnet metamaterial structure and discuss its dispersion relations for TM_z and TE_z polarised fields in Sec. 3.1. In Sec. 3.2 we present the details of the numerical modelling using finite difference time domain (FDTD) software for simulations of the Purcell factor with finite size dipole antenna in a finite metamaterial slab. Following that, eigenmode analysis of the unit cell of the infinite metamaterial is performed in Sec. 3.3 where the band-structure is discussed and used to calculate DOS. Section 3.4 presents the measurements of the Purcell factor using the impedance method for electric and magnetic dipoles in the metamaterial and comparison with FDTD simulations. We apply a method to filter out the reflections from the boundaries of the finite structure, which enables comparison with infinite structure's DOS. In Sec. 3.5 we compare the DOS obtained by the impedance method with the DOS obtained from eigenmode calculations.

3.1 Microwave fishnet metamaterial structure

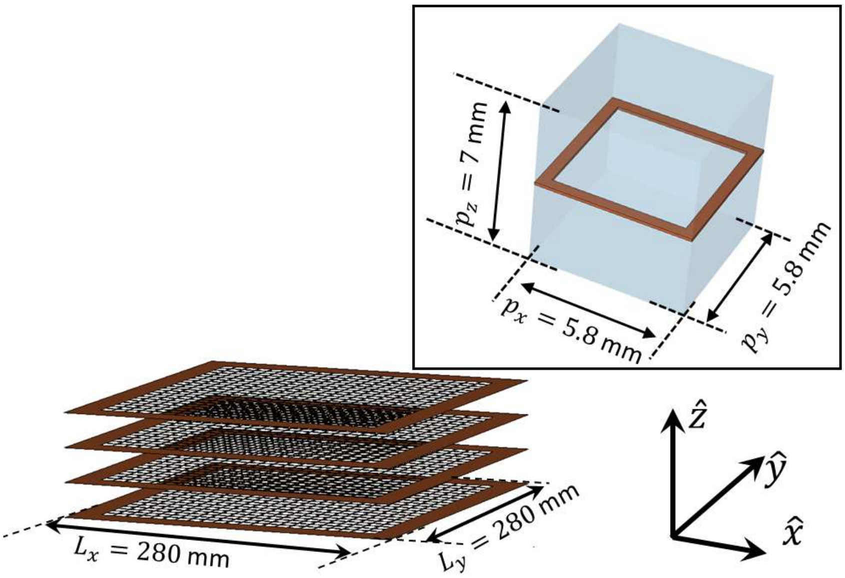

Figure 3.1: Fishnet metamaterial structure used for study is composed of 4 layers of 0.1 mm thick copper grids in the plane stacked in $\hat{z}$ direction. (Inset) Unit cell of the metamaterial structure.

We now present the fishnet metamaterial structure used in this chapter. The structure is composed of metal grids in the x-y plane stacked in the $\hat{z}$ direction (Fig. 3.1). The grids are separated in the $\hat{z}$-direction by expanded polystyrene which has a relative permittivity close to unity and negligible losses in the frequency range 5-15 GHz used in this study. Copper has negligible losses in the frequency range in our study; this means that quenching, which is a consequence of ohmic losses in the metal, will not have a significant effect on the Purcell factor. The structure was fabricated using copper grids with the period in x and y directions $p_x = p_y = 5.8$ mm and spacing between the grids $p_z = 7.0$ mm. The length of the inner edge is 4.95 mm. The total length of the structure in the x-y directions is 280 mm. The frequency range for the measurements is 5-15 GHz, which corresponds to a wavelength range of 20 - 60 mm, which is consistent with the frequency range of our experimental apparatus (see Section 3.4.1).

The effective permittivity of this structure can be expressed by a uniaxial anisotropic permittivity tensor $[\bar{\varepsilon}] = [\varepsilon_{//}, \varepsilon_{//}, \varepsilon_{zz}]$ where the anisotropy axis of the structure is the $\hat{z}$-direction. In the simplest approximation, the effective permittivity of this structure can be described by a local, lossless Drude model [119–121] with $\varepsilon_{//}(\omega) = 1 - \omega_p^2/\omega^2$, where ω_p is the effective plasma frequency. For $\omega < \omega_p$, $\varepsilon_{//} < 0$ whereas for $\omega > \omega_p$, $\varepsilon_{//}(\omega) > 0$.

The thickness of the copper sheets is 0.1 mm, which is much smaller compared to the wavelength. Hence, the structure has an effective electromagnetic response of dilute thin metal layers in the $\hat{z}$ direction. This leads to the effective permittivity along $\hat{z}$ close to unity$\varepsilon_{zz}(\omega) \simeq 1$. Our $5 - 15$ GHz frequency range includes the effective plasma frequency which was reported to be around 14 GHz for such a structure [118], so as to be able to observe the transition in the Purcell factor across the plasma frequency. At frequencies below 5 GHz the wavelength becomes comparable to the size of the structure so finite size effects become predominant, while above 15 GHz the effective medium approximation starts to break down.

The structure has a permittivity tensor such that $\mathrm{Re}(\varepsilon_{//}) \cdot \mathrm{Re}(\epsilon_{zz}) < 0$ below the plasma frequency. These materials were introduced as hyperbolic metamaterials in Sec. 1.3. For hyperbolic materials, the dispersion relation is different for TE$_z$ and TM$_z$ polarizations [70]. For a structure with such an effective anisotropic permittivity tensor, the electromagnetic waves can be split into transverse electric TE$_z$ and TM$_z$ polarizations with isofrequency dispersion relations given by Eqs. (1.11), (1.12).

The density of states is proportional to the infinitesimal volume between two closely separated isofrequency surfaces Eqs. (1.11), (1.12) formed by frequencies ω and $\omega+\delta\omega$. If $\varepsilon_{//}(\omega) < 0$ then, in the TE$_z$ polarisation Eq. (1.11), there are no real propagating solutions, whereas TM$_z$ polarisation Eq. (1.12) due to the hyperbolic nature of the dispersion relation can have a large Purcell factor [17, 71, 76, 122]. Hence, the TE$_z$ and TM$_z$ polarisations have different Purcell factors. Since we shall study the Purcell factor using the impedance of dipoles, we now discuss the effect of dispersion relations when the dipoles, electric and magnetic, are embedded inside such a uniaxial anisotropic structure.

In vacuum an electric dipole (along $\hat{z}$) emits completely in the TM$_z$ ($H_z = 0$) polarisation, similarly a magnetic dipole emits in the TE$_z$ ($E_z = 0$) polarisation. If the dipole is embedded in a general anisotropic medium, the fields cannot be decomposed simply into TE and TM polarisations. However, this decomposition becomes possible again in the particular case of a uniaxial medium where the dipole is oriented along the anisotropy axis $\hat{z}$. As shown by Clemmow [77], the electric and magnetic fields then retain the property ($H_z = 0$) and ($E_z = 0$) for electric and magnetic dipoles respectively. Hence, for our particular anisotropic structure we can use electric and magnetic dipoles to observe the effect of dispersion relations in Eqs. (1.11), (1.12) on the Purcell factor.

3.2 Numerical modelling for density of states calculation

For numerical calculations of the band structure and isofrequency dispersion relations, the periodic unit cell of the structure as shown in Fig. 3.1 was modeled and its propagating eigenmodes were calculated using the eigenmode solver in commercial software CST Microwave Studio [123]. Periodic boundary conditions are applied on the sides of the unit cell, which enforces that the structure is infinitely periodic in each direction. Individual phase shifts $\Delta\phi_x, \Delta\phi_y, \Delta\phi_z$ are applied on the boundaries, the phase shifts corresponding to phase difference between the fields on the two boundaries and by varying the phase between 0 to π the propagation vector (k_x, k_y, k_z) can be fixed to any location in the first Brillouin zone. The eigenfrequencies are then computed for the desired propagation vectors for obtaining the band-diagram (Fig. 3.2) and isofrequency

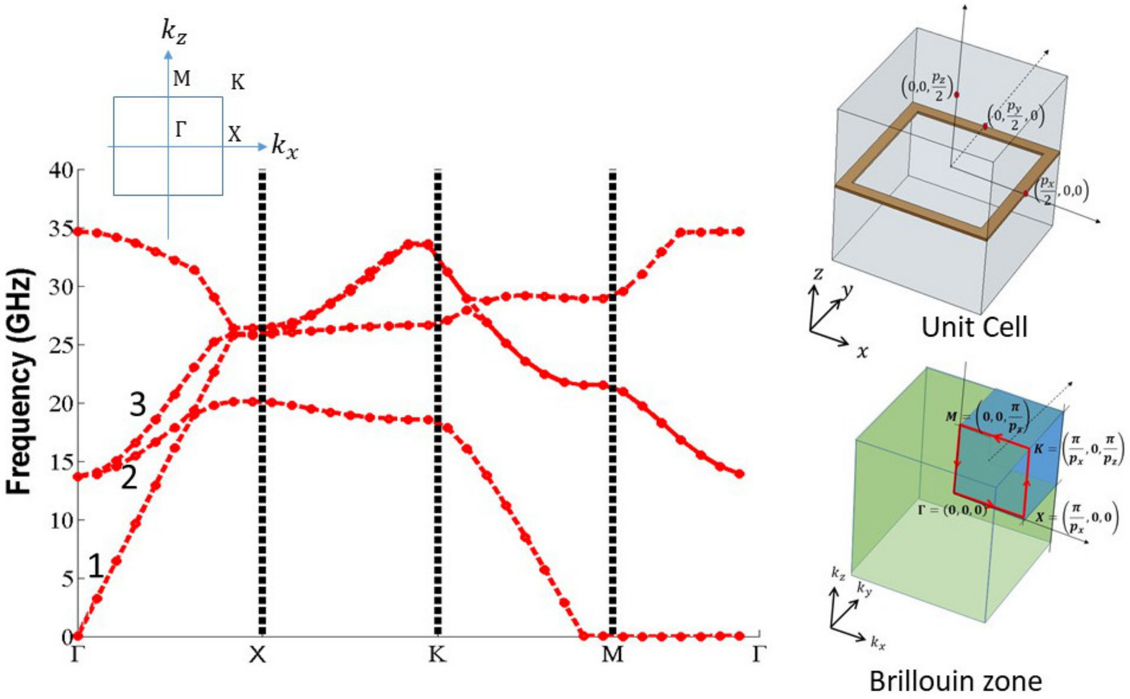

Figure 3.2: Band diagram of the metamaterial unit cell in (Fig. 3.1) along the path $\Gamma(k_x = 0, k_z = 0) - X(k_x = \pi/p_x, k_z = 0) - K(k_x = \pi/p_x, k_z = \pi/p_z) - M(k_x = 0, k_z = \pi/p_z) - \Gamma(k_x = 0, k_z = 0)$.

dispersion relations (Fig. 3.3).

In the band-diagram (Fig. 3.2) the first three modes are marked and the isofrequency dispersion curves for the three modes are presented in Fig. (3.3). The first mode starts from the Γ point ($k_x = 0, k_z = 0$) and has isofrequency curves resembling hyperboloids, as shown in (Fig. 3.3(a)). The second mode starts from 13.6 GHz, which also denotes the plasma frequency ω_p. In the previous work of Enoch et al [118] only the second mode was considered and the first mode was not excited.

From the hyperbolic isofrequency surfaces of mode 1 (Fig. 3.3(a)) we can confirm that the material acts as a hyperbolic metamaterial. However, at low frequencies the topology is more cylindrical than hyperbolic. The Poynting vector, which gives the direction of power flow, is normal to the isofrequency surfaces, so at low frequencies most power is confined in the x-y plane. It is consistent with the fact that at low frequencies the structure behaves like a parallel plate waveguide and most of the power is confined between two grids. Mode 2 (Fig. 3.3(b)) and mode 3 (Fig. 3.3(c)) start as spheres of small radius at the plasma frequency (ω_p) around 13.6 GHz. The radius of these spheres can be expressed as $k_0 n$, where n is an effective refractive index and $k_0 =$

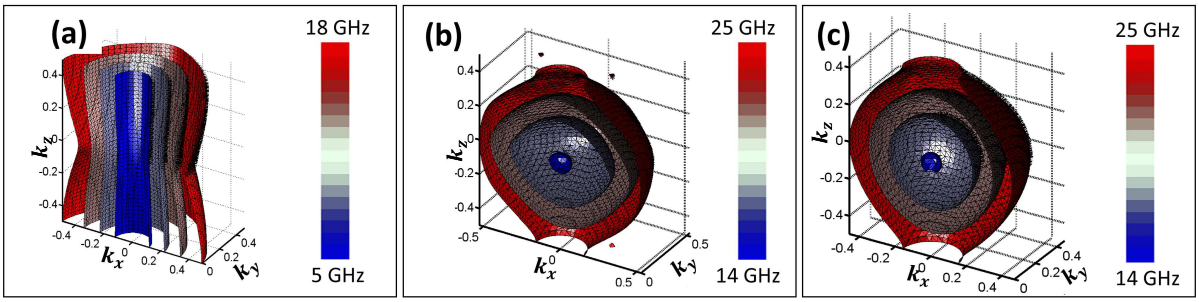

Figure 3.3: Isofrequency surfaces for the unit cell in (Fig. 3.1) (a), (b), (c) show isofrequency surfaces for modes 1, 2 and 3 respectively as marked in Fig. 3.2. The topology of isofrequency surfaces for mode 1 (a) is hyperbolic and leads to a high density of states. Mode 2 (b), mode 3 (c) begin at 13.6 GHz, at the plasma frequency ω_p. The Brillouin zone sectioned by the plane $k_y = 0$.

ω/c is the wave number in free space. A small radius implies a small effective refractive index n. Thus at frequencies slightly greater than the plasma frequency 13.6 GHz, where the second and third mode in the band diagram (Fig. 3.2) originate, the material acts as an epsilon-near-zero or index near zero medium [118].

3.3 Density of states calculation from iso-frequency surfaces

Having obtained the isofrequency surfaces, we now proceed to calculate the density of states for our metamaterial unit cell from these isofrequency surfaces. The density of states is defined as,

$$D(\omega) = \sum_n \int_{BZ} d\mathbf{k}\delta(\omega - \omega_{n,\mathbf{k}}). \tag{3.1}$$

Integration is performed over $\mathbf{k}$ where $\omega_{n,\mathbf{k}}$ are the eigenfrequencies corresponding to the wave vectors $\mathbf{k}$ and mode number n. The DOS can also be expressed in terms of the infinitesimal volume of the shell formed between two closely separated iso-frequency surfaces of frequencies ω and $\omega + \mathrm{d}\omega$

$$D(\omega)\mathrm{d}\omega = \frac{1}{(2\pi)^3} \iint_{\delta\omega} \mathrm{d}k_1^{//} \mathrm{d}k_2^{//} \frac{\mathrm{d}\omega}{|\vec{\nabla}\omega_k|}, \tag{3.2}$$

where $\mathbf{k_1}^{//}$ and $\mathbf{k_2}^{//}$ are tangential to the iso-frequency surface and $\mathrm{d}k_1^{//}\mathrm{d}k_2^{//}$ forms a differential surface area element on the isofrequency surface $\omega(k_x, k_y, k_z)$. The integral in (3.2) can be evaluated by discretizing the isofrequency surface (Fig. 3.4) into N

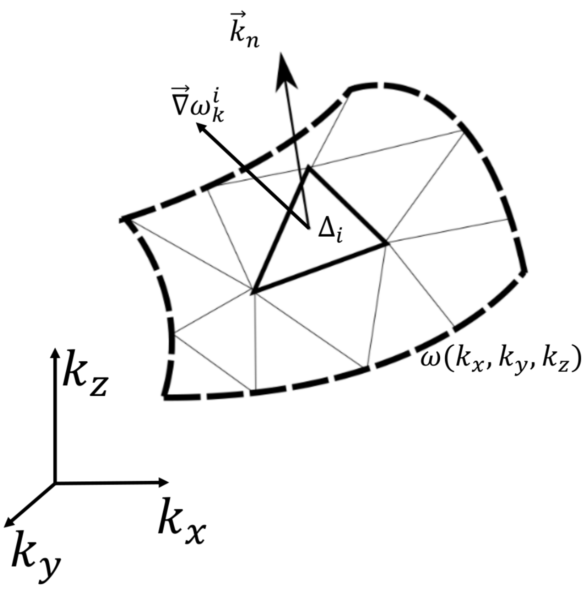

Figure 3.4: Illustration of the method used to compute the density of states. The isofrequency surface, $\omega(k_x, k_y, k_z)$ is divided into N triangles; the gradient $\vec{\nabla}\omega_k$ is computed at the centroids of the triangular patches and used in (Eq. 3.3) to compute the density of states.

triangles and expressing Eq. (3.2) as a summation,

$$D(\omega) = \frac{1}{(2\pi)^3} \sum_i^N \Delta^i \frac{1}{|\vec{\nabla}\omega_k^i|} \tag{3.3}$$

where, Δ^i is the area of the i^{th} triangular patch and $|\vec{\nabla}\omega_k^i|$ is the magnitude of gradient at the center of the triangle.

The density of states $D(\omega)$ calculated from the isofrequency surfaces shown in Fig. 3.3 using equation Eq. (3.3) is shown in Fig.3.5. The density of states of individual modes of the metamaterial unit cell is compared with the density of states for vacuum for TM polarisation given by $\frac{\omega^2}{2\pi^2 c^3}$. We observe that the DOS for mode 1 is large compared to vacuum which is expected due to the hyperbolic nature of the mode. In contrast, for modes 2 and 3 $D(\omega) = 0$ below $\omega_p \approx 13.6$ GHz as TE$_z$ modes cannot propagate at these frequencies.

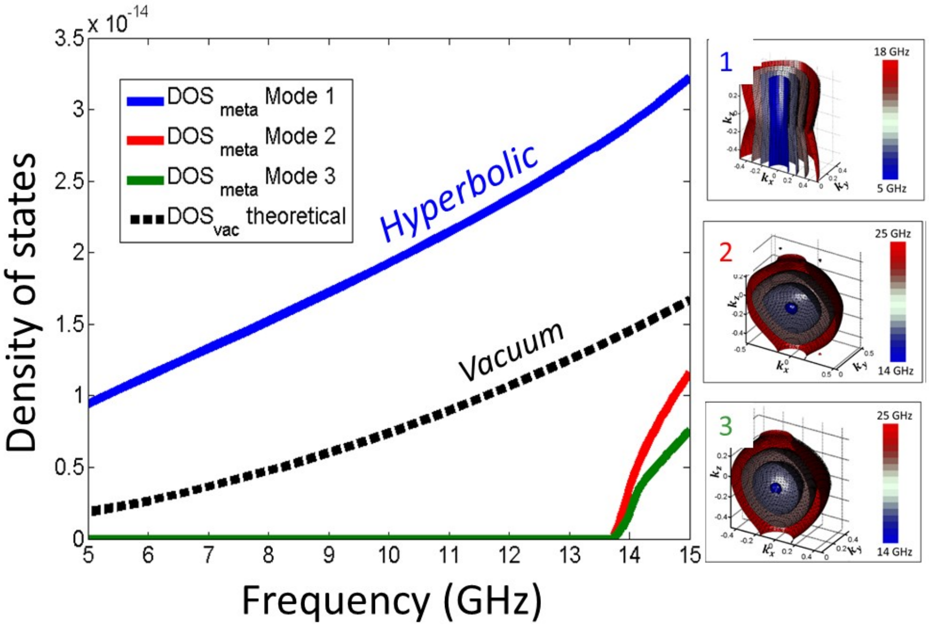

Figure 3.5: Density of states computed with the iso-frequency surfaces for mode 1 (blue), mode 2 (red) and mode 3 (green) as shown in (Fig. 3.3) and compared with the theoretical density of states for vacuum (dashed). The first mode due to hyperbolic isofrequency surfaces has higher DOS than vacuum.

3.4 Experiments

3.4.1 Measurement of the Purcell factor with antenna impedance

We now outline our procedure for the measurement of the Purcell factor. For a weakly lossy, subwavelength, dipole antenna the real part of the input impedance $\mathrm{Re}(Z_{in})$ is proportional to the Purcell factor (Eq. (2.65)). As discussed in Sec. 2.10.2, the input impedance can be obtained from the scattering coefficient S_{11} (Eq. (2.71)). The Purcell factor is thus obtained from the reflection coefficient S_{11} [33]

$$F = \frac{\mathrm{Re}(Z_{in})}{\mathrm{Re}(Z_{in}^{(0)})} = \frac{R_{in}}{R_{in}^{(0)}}, \tag{3.4}$$

where,

$$R^{in} = Z_w \frac{1 - \mathrm{Re}(S_{11})^2 - \mathrm{Im}(S_{11})^2}{(1 - \mathrm{Re}(S_{11}))^2 + \mathrm{Im}(S_{11})^2}. \tag{3.5}$$

Here S_{11} is the reflection coefficient and $Z_w = 50\ \Omega$ is the characteristic impedance and the superscript $^{(0)}$ is the reference measurements in vacuum. We use this approach to measure the Purcell factor of our metamaterial structure.

The procedure for measurement of the Purcell factor is as follows. The dipole (electric or magnetic) is attached to a coaxial cable and S_{11} is recorded in free space. From S_{11} measurements, the reference input impedance for vacuum $R_{in}^{(0)}$ is obtained via Eq. (3.5). The dipole is then placed at the center of the structure between the second and third copper grids. S_{11} is recorded and R_{in} is calculated again from Eq. (3.5). The Purcell factor is then obtained from Eq. (3.4) as the ratio of R_{in} in the metamaterial to the $R_{in}^{(0)}$ in vacuum. The electric and magnetic Purcell factors $(F^{e/m})$ thus measured experimentally are compared with the Purcell factor obtained using simulated S_{11} from FDTD method.

In simulations and for the experiments, the sub-wavelength size electric dipole antenna was made of thin conducting wires of total length 6.3 mm, while the magnetic dipole was a wire loop antenna of radius 3.0 mm. Measurements were performed with a vector network analyser (VNA) model Anritsu MS2027C for the frequency range 5-15 GHz. At the high-frequency end this was limited by the VNA. The plasma frequency $(\omega_p = 13.6\ \text{GHz})$ of the structure lies in this frequency range which allows us to observe the change in Purcell factor around this frequency.

Numerical simulations for calculations of the Purcell factor using the antenna impedance method were performed using commercial finite difference time domain solver software (CST Microwave Studio). Perfectly matched layers (PML) are used to truncate the computational domain with space added near the structure. The total number of mesh cells was approximately 10^9 for the entire structure. We checked numerically that the dipole is sufficiently subwavelength in length and the Purcell factor does not depend significantly on the dipole parameters. The available time domain solver in CST was used to calculate the scattering coefficients (S-Parameters) in the frequency range 5-15 GHz.

When the electric dipole is oriented along $\hat{z}$, the Purcell factor (F) is strongly affected by the Fabry-Perot (FP) resonances. The effect of FP resonances on the Purcell factor in metamaterials has been studied in the context of wire-medium hyperbolic metamaterials [91] where it was argued that the Fabry-Perot resonances do not affect the average value of the Purcell factor. It was numerically shown that the frequency averaged Purcell factor in a finite structure agreed with the Purcell factor of an infinitely periodic structure. While taking the average may seem heuristic, a similar signal processing technique can be justified from the physics of the resonances: The Fabry-Perot resonances are caused by reflections from the boundaries of the finite structure; eliminating these reflections by dismissing the time signal from the time during which reflections arrive should give a good approximation to the response of the infinite medium. A similar technique was used to remove Fabry-Perot resonance artifacts in hyperlens images [82].

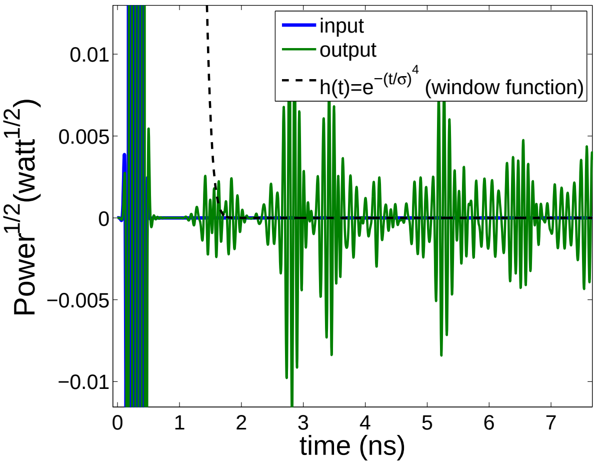

Figure 3.6: Input and output time signals from FDTD simulations for an electric dipole along $\hat{z}$ placed at the center of the structure. The first reflection in the output signal occurs around 0.9 ns which corresponds to the time taken by the wave to reflect back from the boundary of the structure.

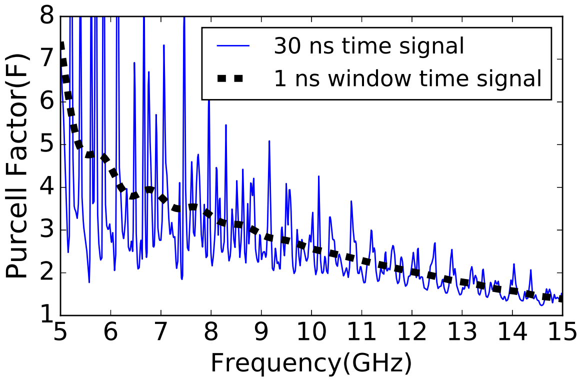

Figure 3.7: The Purcell factor for an electric dipole along $\hat{z}$ computed from the time signals in Fig. 3.7. Solid curves are calculated from time signals up to 30 ns; dashed curves give the corresponding results after time windowing to eliminate the effect of the reflections from the boundaries.

The Purcell factor is calculated from the reflection coefficient S_{11} (Eq. (3.5)). In the FDTD simulations S_{11} is calculated from the time signals as the ratio of the Fourier transform ($\mathfrak{F}$) of the output ($O(t)$) and the input ($I(t)$) time signals, $S_{11}(\omega) = \mathfrak{F}(O(t))/\mathfrak{F}(I(t))$. The dipole is placed at the center of the structure which has a lateral width of $L =$

280 mm. The time for the wave to reflect back from the boundaries (t^{ref}) is thus $t^{\mathrm{ref}} = L/c \simeq 0.9$ ns where c is the speed of light in free space. We can observe the reflections in the time signals at 0.9 ns in Fig. 3.6. By limiting our time signal to t^{ref} the reflections are excluded and Fabry-Perot resonances are eliminated. In order to limit the time signals to t^{ref} we multiply the input and output signals by a super gaussian windowing function $h(t) = e^{-(t/\sigma)^4}$ with window length $\sigma = 1$ ns. Since we obtain S_{11} in the frequency domain from the VNA, we convolve the measured S_{11} in frequency domain by $H(\omega)$ where $H(\omega) = \mathfrak{F}(h(t))$. Figure 3.7 shows that the truncation of the time signal (Fig. 3.6) removes the effect of the Fabry-Perot resonances on the Purcell factor (F).

3.5 Results and discussion

Measurement results for the Purcell factor using antenna impedance inside the metamaterial structure is now presented. Three cases are considered: First, for a magnetic loop dipole antenna oriented along $\hat{z}$. In this case the fields inside the metamaterial are in TE$_z$ polarization. Second, for an electric dipole antenna oriented along $\hat{y}$. In this case also the fields corresponds to the TE$_z$ polarization. Finally, for an electric dipole antenna oriented along $\hat{z}$. In this case the fields correspond to the TM$_z$ polarization.

3.5.1 Purcell factor for magnetic dipole oriented along $\hat{z}$

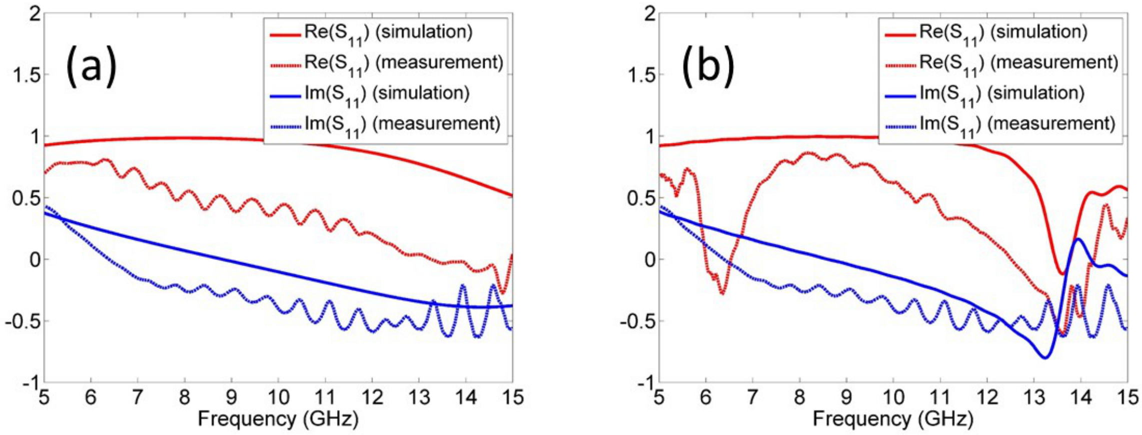

Figure 3.8: Real (red) and imaginary (blue) parts of scattering coefficient S_{11} from simulations (solid) and measurements (dashed), (a) in free space, (b) in metamaterial with magnetic loop dipole antenna oriented along $\hat{z}$.

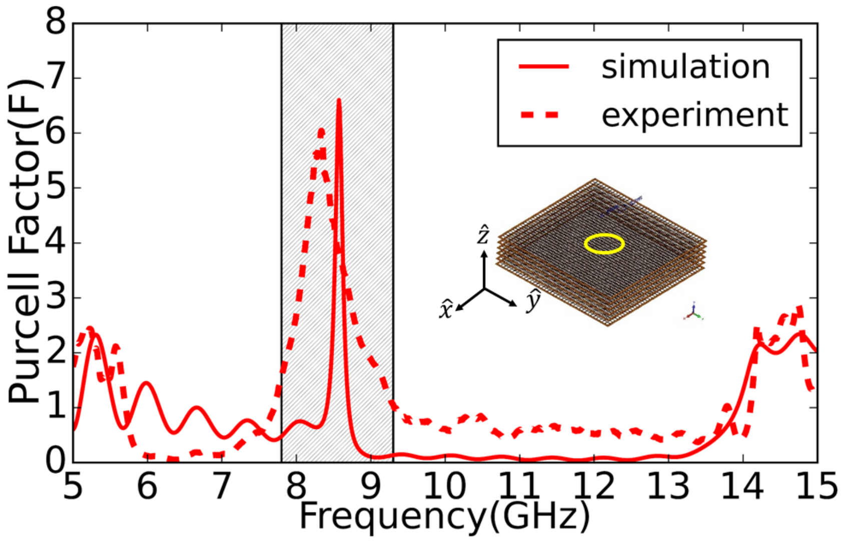

Figure 3.9: Measurement and simulation of magnetic Purcell factor for a magnetic dipole oriented along $\hat{z}$, inside the metamaterial structure.

Fig. 3.8 (a) shows measurements and simulations of the real and imaginary parts of scattering coefficient S_{11} for a magnetic dipole in vacuum. Fig. 3.8 (b) shows S_{11} for a magnetic dipole oriented along $\hat{z}$ inside the metamaterial structure. The measurement in vacuum serves as the reference measurement. The scattering coefficient S_{11} is then substituted in Eq. (3.5) to obtain the real part of the input impedance of the antenna. Which in turn is used to obtain the Purcell factor using Eq. (3.4). Figure (3.9) shows the magnetic Purcell factor for a magnetic dipole oriented along $\hat{z}$ inside the structure.

A magnetic dipole embedded inside a uniaxial anisotropic medium oriented parallel to the symmetry axis ($\hat{z}$) emits in the TE$_z$ polarization [77] which allows no propagating solutions when $\omega < \omega_p \approx 13.6\ \text{GHz}$ where $\varepsilon_{//} < 0$ (Eq. (1.11)). Indeed, we see that below the plasma frequency the Purcell factor is close to zero because emission is suppressed, and only takes significant values above the plasma frequency. This result is analogous to the inhibition of spontaneous emission of atoms [9].

The enhancement in Purcell factor in Fig. 3.9 around 8.5 GHz is due to the anti-resonance of the dipole which occurs when the circumference of the dipole loop $C = \lambda/2$. This is illustrated in Fig. 3.10, which shows the impedance of a magnetic dipole loop antenna with outer radius $b = 3\ \text{mm}$ and wire radius $a = 1\ \text{mm}$, using a Fourier series expansion method [111, 124] (green curve) and an FDTD calculation (blue curve). These confirm that the peak around 8.5 GHz corresponds to the first anti-resonance.

The Purcell factor is a property of the medium and cannot depend on the dipole.

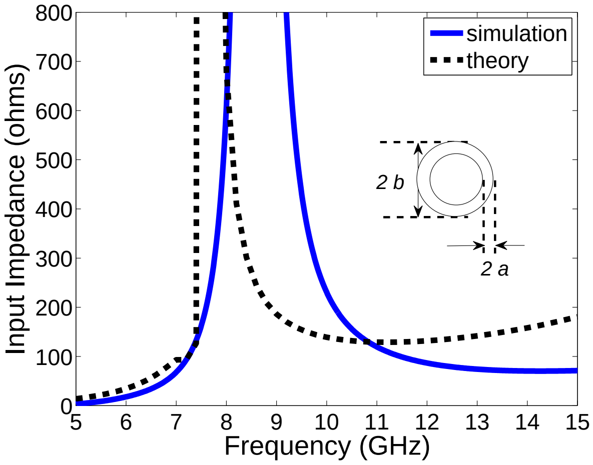

Figure 3.10: Comparison of FDTD simulations (blue) and theoretical calculations (black, dashed) of input impedance $\mathrm{Re}(Z_{in})$ of a magnetic dipole antenna in vacuum with outer radius $b = 3$ mm and wire radius $a = 1$ mm.

Hence the peak near 8.5 GHz in Fig. 3.9 does not correspond to an enhancement of the Purcell factor. This is analogous to the strong coupling regime where the LDOS loses its meaning. Strong coupling is discussed further in Appendix B. Hence, care must be taken to avoid antenna-related artifacts when using the impedance method to measure the Purcell factor.

3.5.2 Purcell factor for electric dipole oriented along $\hat{y}$

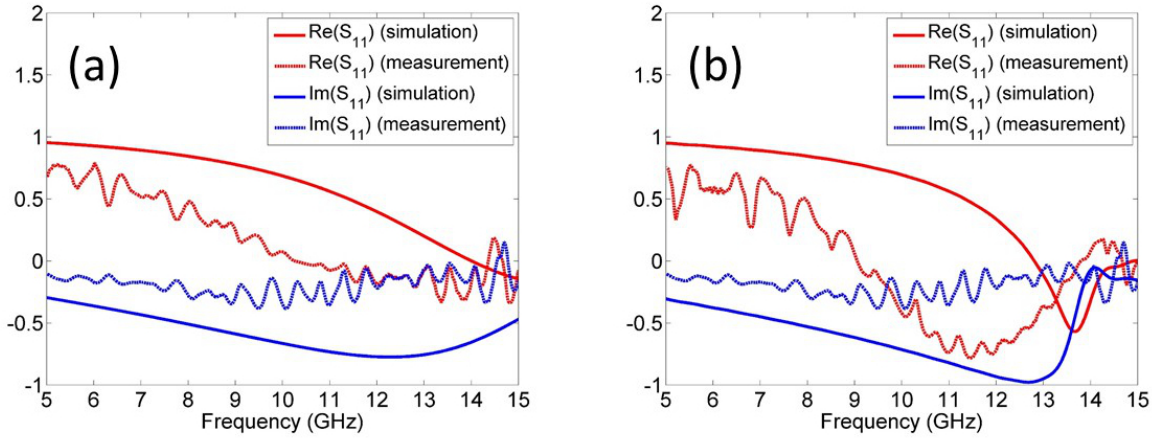

Figure 3.11: Real (red) and imaginary (blue) parts of scattering coefficient S_{11} from simulations (solid) and measurements (dashed), (a) in free space, (b) in metamaterial with electric dipole antenna oriented along $\hat{y}$.

Fig. 3.11 (a) shows measurements and simulations of the real and imaginary parts of scattering coefficient S_{11} for a electric dipole in vacuum. Fig. 3.11 (b) shows S_{11}

for the electric dipole oriented along $\hat{y}$ inside the metamaterial structure. The scattering coefficient S_{11} is then substituted in Eq. (3.5) to obtain the real part of the input impedance of the antenna. Which in turn is used to obtain the Purcell factor using Eq. (3.4). Figure (3.9) shows the electric Purcell factor for an electric dipole oriented along $\hat{y}$ inside the structure.

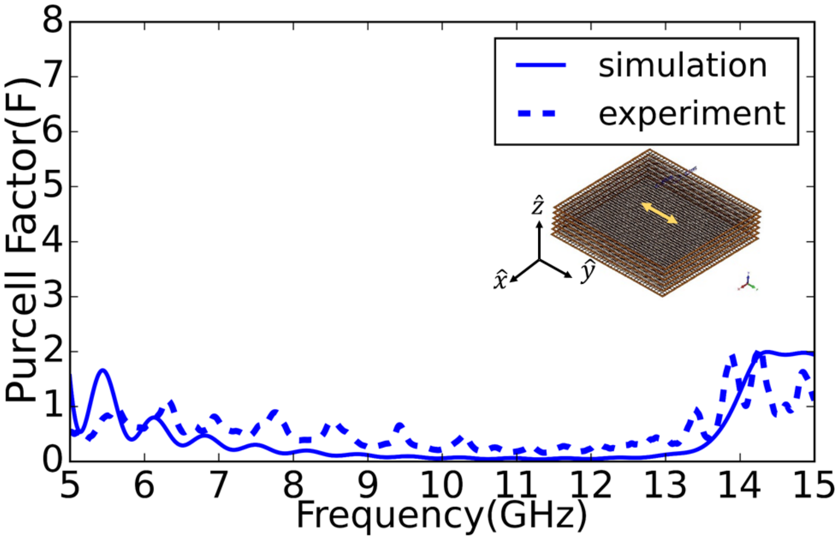

Figure 3.12: Measurement and simulation of electric Purcell factor for an electric dipole oriented along $\hat{y}$, inside the metamaterial structure.

In this particular orientation the field is a superposition of TE$_z$ and TM$_z$ polarisations. The Purcell factor is similar to that of the magnetic dipole parallel to the anisotropy axis (pure TE$_z$-polarisation) (Fig. 3.9), without the anti-resonance peak. The similarity with the magnetic Purcell factor can be interpreted as follows. For a magnetic dipole oriented along $\hat{z}$, the electric field is in the x-y plane (TE$_z$-polarisation). For the electric dipole along $\hat{y}$, perpendicular to the anisotropy axis $\hat{z}$ most of the power is radiated with the electric field along $\hat{y}$. However, the structure in which it is embedded does not allow propagation with a component of the electric dipole along $\hat{y}$, below the plasma frequency as the metallic grids are in the x-y plane similar to the magnetic dipole. Hence we measure the same plasma frequency in both cases and also a similar Purcell factor with the electric dipole perpendicular to the anisotropy axis.

We point out that there is no enhancement of the Purcell factor around 8.5 GHz for this case, in contrast to what was observed for the magnetic dipole (Fig. 3.9). Indeed, for an electric dipole of length $l = 6$ mm, the anti-resonance lies at the matching frequency $\lambda/2 = l$, (that is, 25 GHz) which is outside the measurement range.

3.5.3 Purcell factor for electric dipole oriented along $\hat{z}$

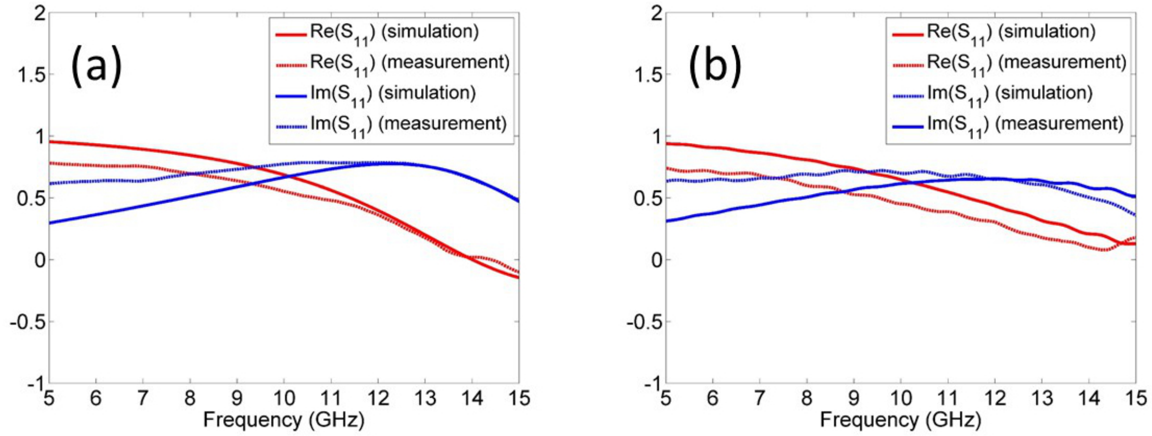

Figure 3.13: Real (red) and imaginary (blue) parts of scattering coefficient S_{11} from simulations (solid) and measurements (dashed), (a) in free space, (b) in metamaterial with electric dipole antenna oriented along $\hat{z}$.

Fig. 3.13 (a) shows measurements and simulations of the real and imaginary parts of scattering coefficient S_{11} for a electric dipole in vacuum. Fig. 3.13 (b) shows S_{11} for the electric dipole oriented along $\hat{z}$ inside the metamaterial structure. The scattering coefficient S_{11} is then substituted in Eq. (3.5) to obtain the real part of the input impedance of the antenna. Which in turn is used to obtain the Purcell factor using Eq. (3.4). Figure (3.14) shows the Purcell factor for an electric dipole oriented along $\hat{z}$ inside the structure.

The electric dipole embedded inside a uniaxial anisotropic medium oriented parallel to the anisotropy axis emits in the TM_z polarization [77]. The Fabry-Perot resonances are removed by applying a convolution which corresponds to a super gaussian window in the time domain, with a window length of $t^{\text{ref}} = 0.9$ ns as mentioned in Sec. 3.4. In the TM_z polarization the dispersion relation for the uniaxial hyperbolic medium is given by Eq. (1.12). The hyperbolic nature of the dispersion relation leads to a large LDOS and a large Purcell factor.

The Purcell factor decreases with frequency, which can be interpreted as a consequence of the periodicity of the structure limiting the maximum permitted value of k_z. In a medium where k_z is bound by a maximum value $k_{z,max}$ the DOS of the structure is linearly proportional to ω [73],

$$D(\omega) = \frac{\omega}{\pi^2 c^2} \frac{\varepsilon_{zz}}{2} k_{z,max}, \tag{3.6}$$

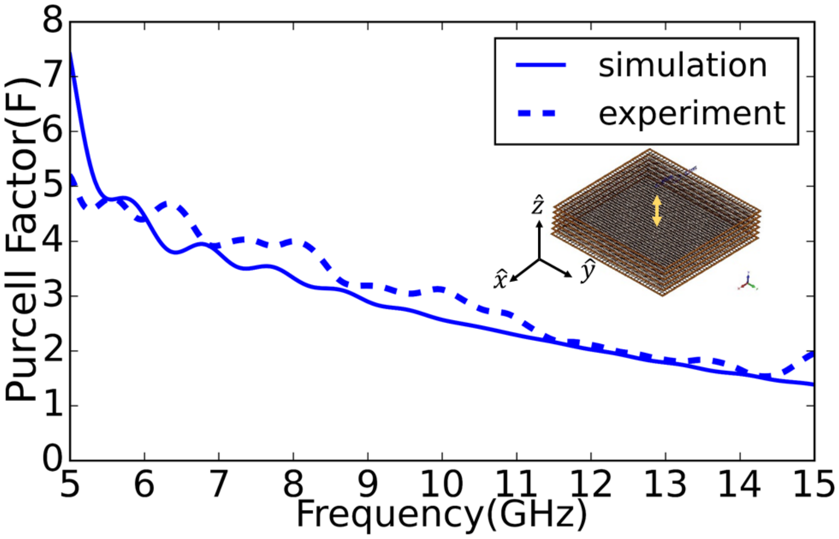

Figure 3.14: Measurement and simulation of electric Purcell factor for an electric dipole oriented along $\hat{z}$, inside the metamaterial structure.

whereas the DOS for vacuum is proportional to ω^2. The Purcell factor is the ratio of LDOS inside the structure to the LDOS in vacuum, and hence decreases with frequency ω.

3.5.4 Comparison of the DOS from eigenmode calculations and impedance of antennas

So far, we have calculated the DOS using eigenmode analysis (Sec. 3.3), and have measured and calculated the LDOS using the impedance method (Sec. 3.4). The LDOS can be computed from eigenmode calculations, as discussed in Ref. [125]. Conversely, the DOS can be calculated from the LDOS quite readily, allowing us to compare both results. We define the relative density of states ($rel.DOS$) as the ratio of the DOS of the metamaterial unit cell to the theoretical DOS for vacuum. The DOS is the spatial average of the LDOS over the unit cell. The Purcell factor depends on the location and the orientation of the dipole inside the unit cell. Hence, an average of the Purcell factor over the unit cell and the three orientations (x, y and z) is equivalent to $rel.DOS$.

For calculating the $rel.DOS$ with the impedance method, an average of the Purcell factor over a unit cell of the metamaterial is required. Numerical simulations of a dipole antenna were performed at 27 locations in one-eighth of the unit cell along $\hat{z}$ and $\hat{y}$ directions. By symmetry of the unit cell it is equivalent to $27 \times 8 = 216$ locations. The impedance was obtained from reflection coefficient S_{11} and the average of the Purcell

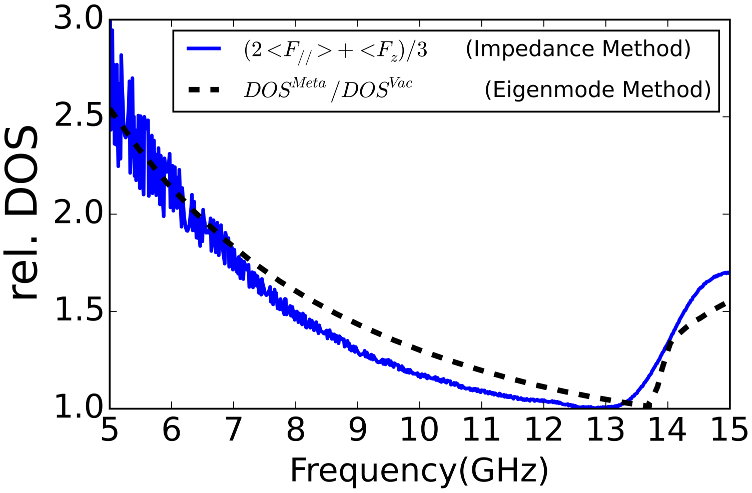

Figure 3.15: Comparison of the $rel.DOS$ obtained from impedance method (blue) and $rel.DOS$ from eigenmode calculations (dashed) as shown in (Fig. 3.5).

factor was calculated. The length of the dipole antenna was chosen to be 1 mm. The Purcell factor was numerically evaluated from the impedance method (Sec.3.4) at each location and its average is denoted as $\langle F_i \rangle$, where i is the orientation of the dipole. The simulation was limited to $t^{\text{ref}} = 0.9$ ns to remove reflections from the boundaries, as discussed in Sec. 3.4.

Averaging the Purcell factor in the three directions we obtain $rel.DOS = (\langle F_x \rangle + \langle F_y \rangle + \langle F_z \rangle)/3 = (2\langle F_{//} \rangle + \langle F_z \rangle)/3$. For the eigenmode method, there are three modes present between 5-15 GHz (Fig. 3.5) and they are summed to obtain $rel.DOS$ that is, $rel.DOS = (DOS^{Meta})/DOS^{vac} = (DOS^{Mode\ 1} + DOS^{Mode2} + DOS^{Mode\ 3})/DOS^{vac}$. Results of the comparison are presented in Fig. 3.15 and we find a good agreement between the two methods.

This chapter concludes the first part of this thesis, wherein we studied the influence of the environment on the Purcell factor using antennas. Though we focused on the density of states of a hyperbolic fishnet metamaterial at microwave frequencies, our method can be used to study the density of states for other periodic structures as well. In the following Chapters 4, 5 we study resonance energy transfer. We shall show that an antenna based formalism can also be developed to characterize the influence of the environment on resonance energy transfer.

Chapter 4

Resonance energy transfer

If two identical atoms are placed in proximity to each other, such that one of the atoms (donor) is its excited state while the other (acceptor) is in its ground state, the donor atom can transfer its excitation to the acceptor atom in the ground state and this process is called resonance energy transfer. In this chapter the aim is to study the influence of environment on resonance energy transfer. As the atom field coupling is dipolar in nature, it belongs to the general class of problems mediated by dipole-dipole interactions (DDI). In the previous chapter we studied the influence of environment on the decay rate of an atom its relation to the impedance of an antenna. Here, we show that similar antenna coupled circuit models can be developed to study DDI based resonance energy transfer.

Of particular importance is the case when the energy transfer in the near field non-radiative limit, that is $kr_{DA} < 1$ where r_{DA} is the separation distance between the molecules and $k = 2\pi/\lambda$ with wavelength λ, is mainly due to virtual photons, in contrast to far field ($kr_{DA} > 1$) where the energy exchange is due to real photons. This is relevant to Förster's resonance energy transfer (FRET) [126] and important to several areas of biology, chemistry and quantum computation. The near field non-radiative transfer and the far-field radiative transfer are the near-field and far-field limits of the same process [127] and the analysis presented here is valid for near-field as well as far field limits. Here, we develop a method to investigate DDI at microwave frequencies. We treat it as the interaction of two circuits which are linearly coupled through sub-wavelength antennas. We show that the impedance Z_{21} of such a two-port network is related to the Green function $\overleftrightarrow{\mathbf{G}}(\mathbf{r}_A, \mathbf{r}_D; \omega)$ which determines the FRET rate, where $\mathbf{r}_D$ and $\mathbf{r}_A$ are the locations of the donor and acceptor dipoles, respectively.

Starting with briefly summarizing the QED based approach to study resonance energy transfer in Sec. 4.1 we highlight the role of the classical Green function in DDI. The classical analogue to energy transfer between is discussed in Sec. 4.2, with particular emphasis to the case when the separation between the two dipoles is sub-wavelength. Then we develop the antenna coupled circuit model in Sec. 4.3 and define a figure of merit to characterize the effect of environment on the DDI and discuss the similarities and differences from studying the Purcell factor with antennas.

4.1 Quantum electrodynamical formulation of resonance energy transfer

Dipole-dipole Interaction has been investigated extensively in quantum electrodynamics [128–133] . Over here we shall briefly summarize the treatment as presented in Ref. [132] to study DDI which stresses the role of the Green function. Consider two identical quantum mechanical molecules denoted, donor (D) and acceptor (A) at locations $\mathbf{r}_D$ and $\mathbf{r}_A$ respectively. The distance between the emitters is denoted as $r_{DA} = |\mathbf{r}_A - \mathbf{r}_D|$. Both donor and acceptor are described by identical two level quantum mechanical systems, with a transition frequency ω which relates to the energy difference, $E_e - E_g = \hbar\omega$ between the excited state $|e\rangle$ and the ground state $|g\rangle$. The transition dipole moment $\boldsymbol{\mu} = -q^e\langle e|\hat{\mathbf{r}}|g\rangle$, where q^e is the magnitude of the charge of an electron. In the weak coupling regime, the coupling is (electric) dipolar and the interaction is equivalent to interaction between two classical dipoles.

The Hamiltonian of the system is given by $\hat{\mathcal{H}} = \hat{\mathcal{H}}_0 + \hat{\mathcal{H}}_{int}$, where $\hat{\mathcal{H}}_0$ is the unperturbed part and $\hat{\mathcal{H}}_{int}$ is the interaction Hamiltonian. The interaction Hamiltonian of the system in (electric-) dipole approximation is

$$\hat{\mathcal{H}}_{int} = -\sum_{j=D,A} \int_0^\infty d\omega \left[\hat{\boldsymbol{\mu}}_j \hat{\boldsymbol{E}}(\mathbf{r}_j, \omega) + h.c.\right]. \tag{4.1}$$

In a non-magnetic medium, the operator counterpart of the electric field is [132]

$$\begin{aligned}\hat{\mathbf{E}}(\mathbf{r}, \omega) = i\sqrt{\frac{\hbar}{\pi\varepsilon_0}\frac{\omega^2}{c^2}} \int d^3\mathbf{r}' \sqrt{\mathrm{Im}[\varepsilon(\mathbf{r}, \omega)]}\, \overset{\leftrightarrow}{\mathbf{G}}(\mathbf{r}, \mathbf{r}', \omega) \\ \cdot\hat{\mathbf{f}}(\mathbf{r}', \omega) + \mathrm{H.c.}\end{aligned} \tag{4.2}$$

where $\varepsilon(\boldsymbol{r}, \omega)$ is the relative permittivity of the medium. $\hat{\mathbf{f}}^\dagger(\hat{\mathbf{f}})$ is the raising (lowering) operator which is responsible for the creation(annihilation) of photons or virtual photons.

We shall consider the initial state in which, the donor is in the excited state while the acceptor is in the ground state, $|i\rangle = |D', A\rangle \otimes |\{0\}\rangle$, where the accent $'$ denotes the excited state of the molecule, $|\{0\}\rangle$ denotes vacuum. We want to investigate the evolution to the final state $|f\rangle = |D, A'\rangle \otimes |\{0\}\rangle$ where, the donor returns to the ground state and the acceptor is in the excited state. Then Fermi's golden rule [134], can be used to calculate the rate of this resonance energy transfer from the initial state $|i\rangle$ to the final state $|f\rangle$ as,

$$\Gamma_{DA} = \frac{2\pi}{\hbar} \sum_{i,f} |\langle f|\hat{T}|i\rangle|^2 \delta(E_f - E_i). \tag{4.3}$$

where $\delta(E_f - E_i)$ is the joint density of states. The transition matrix element $\langle f|\hat{T}|i\rangle$ can be calculated as,

$$\langle f|\hat{T}|i\rangle = \langle f|\hat{H}_{int}|i\rangle + \lim_{\epsilon \to 0} \sum_I \frac{\langle f|\hat{H}_{int}|I\rangle\langle I|\hat{H}_{int}|i\rangle}{E_i - E_I - i\epsilon}. \tag{4.4}$$

where the summation is over $|I\rangle$, the possible intermediate states $|D', A'\rangle\hat{\mathbf{f}}^\dagger|\{1\}\rangle$ and $|D, A\rangle\hat{\mathbf{f}}^\dagger|\{1\}\rangle$ where $|\{1\}\rangle = |\{1_{\omega,\mathbf{k}}\}\rangle$ represents a single photon state with frequency ω and wave vector $\mathbf{k}$. The rate of energy transfer Γ_{DA} is associated with FRET. The transition rate (Eq. (4.3)) expressed using the classical Green function is [132],

$$\Gamma_{DA} = \frac{2\pi}{\hbar^2} \frac{\omega^4}{\varepsilon_0^2 c^4} |\boldsymbol{\mu}_{A'A} \cdot \overset{\leftrightarrow}{\mathbf{G}}(\mathbf{r}_A, \mathbf{r}_D; \omega) \cdot \boldsymbol{\mu}_{DD'}|^2 \delta(\omega_{A'A} - \omega_{D'D}). \tag{4.5}$$

In terms of overlap integrals Eq. (4.5) is of the form [133],

$$\Gamma_{DA} = \int \tilde{\Gamma}_{DA}(\omega) \sigma_D^{em}(\omega) \sigma_A^{abs}(\omega)\, d\omega \tag{4.6}$$

with

$$\tilde{\Gamma}_{DA}(\omega) = \frac{2\pi}{\hbar^2} \frac{\omega^4}{\varepsilon_0^2 c^4} |\boldsymbol{\mu}_A \cdot \overset{\leftrightarrow}{\mathbf{G}}(\mathbf{r}_A, \mathbf{r}_D; \omega) \cdot \boldsymbol{\mu}_D|^2 \tag{4.7}$$

and

$$\sigma_D^{em}(\omega) = \sum_{D,D'} p_{D'} |v_{DD'}|^2 \delta(\omega_{D'D} - \omega) \tag{4.8}$$

$$\sigma_A^{abs}(\omega) = \sum_{A,A'} p_A |v_{A'A}|^2 \delta(\omega_{A'A} - \omega) \tag{4.9}$$

where $\sigma_A^{abs}(\omega)$, $\sigma_D^{em}(\omega)$ are the single photon absorption spectrum of the acceptor and the emission spectrum of the donor in *free space*, $p_{D'(A)}$ is the occupation probability of the donor (acceptor) in the excited (ground) state, and $v_{DD'(A'A)}$ is the overlap integral between the vibrational quantum states in the two electronic states of donor (acceptor).

If the Green function varies slowly over the frequency range of the relevant overlap spectrum then, Eq. (4.6) can be expressed as,

$$\Gamma_{DA}(\omega) = \tilde{\Gamma}_{DA}(\omega)\sigma \tag{4.10}$$

where $\sigma = \int \sigma_D^{em}(\omega)\sigma_A^{abs}(\omega)\, d\omega$. Thus the rate of energy transfer is proportional to the overlap of the two spectra, modulated by the square of the Green function. As we have assumed that the transition dipole moments of the donor and acceptor, $\boldsymbol{\mu}_D$ and $\boldsymbol{\mu}_A$ are unaffected by the change in the environment, then from Eq. (4.7), it is clear that the influence of the electromagnetic environment on rate of energy transfer is contained entirely within the classical Green function.

4.2 Classical dipole-dipole interaction.

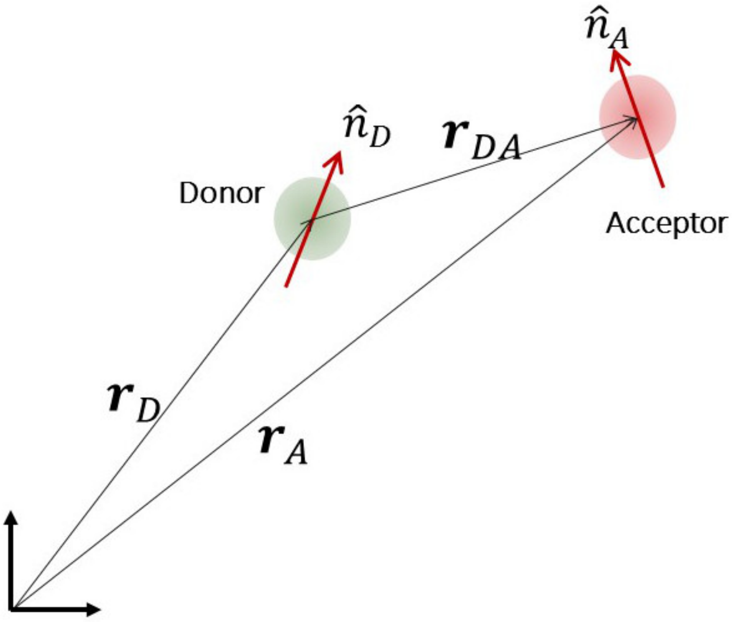

Figure 4.1: Resonance energy transfer between a classical dipole donor acceptor pair.

The interaction between the atoms is predominantly dipolar, hence it is not surprising that the resonant energy transfer can also be studied classically. Treating the donor and acceptor as classical damped harmonic oscillators, with classical dipole moments $\mathbf{p}_D$ and $\mathbf{p}_A$ respectively as seen in Fig. 4.1. As mentioned previously (Sec. (2.6)), in the semi-classical approximation, the quantum mechanical dipole matrix element [135] $\boldsymbol{\mu}$ is linearly related to the classical dipole moment as $\mathbf{p} = 2\boldsymbol{\mu}$. If the electric field due to the donor at the location of the acceptor is $\mathbf{E}_D(\mathbf{r}_A)$ and current density in the acceptor is denoted by $\mathbf{j}_A$ the power transferred from the donor to the acceptor $P_{D\to A}$ is [5]

$$P_{D\to A} = -\frac{1}{2}\int_{V_A} \mathrm{Re}\left\{\mathbf{j}_\mathrm{A}^* \cdot \mathbf{E}_\mathrm{D}(\mathbf{r}_\mathrm{A})\right\} \mathrm{dV}. \tag{4.11}$$

For the acceptor dipole with a dipole moment $\mathbf{p}_A$ Eq. (4.11) can be expressed as,

$$P_{D\to A} = \frac{\omega}{2}\mathrm{Im}\left\{\mathbf{p}_\mathrm{A}^* \cdot \mathbf{E}_\mathrm{D}(\mathbf{r}_\mathrm{A})\right\}. \tag{4.12}$$

Assuming that the donor dipole moment $\mathbf{p}_D$ is constant and the dipole moment of the acceptor $\mathbf{p}_A$ is induced by the electric field due to the donor at the location of the acceptor

$$\mathbf{p}_A = \overleftrightarrow{\boldsymbol{\alpha}}_A(\omega)\boldsymbol{E}_D(\mathbf{r}_A) = \frac{\omega^2}{c^2\varepsilon_0}\overleftrightarrow{\boldsymbol{\alpha}}_A(\omega)\cdot\overleftrightarrow{\mathbf{G}}(\mathbf{r}_A,\mathbf{r}_D;\omega)\cdot\mathbf{p}_D \tag{4.13}$$

where $\overleftrightarrow{\boldsymbol{\alpha}}_A(\omega)$ is the polarisability tensor of the acceptor dipole. Assuming the dipole moment of acceptor points along direction $\hat{n}_A$, acceptor polarizability can be simplified as $\overleftrightarrow{\boldsymbol{\alpha}}_A(\omega) = \alpha_A(\omega)\hat{n}_A\hat{n}_A$. Substituting Eq. (4.13) into Eq. (4.12) the power transferred from the donor to the acceptor is

$$P_{D\to A} = \frac{\omega^5 \mid \mathbf{p}_D \mid^2}{2c^4\varepsilon_0^2}\mathrm{Im}\left\{\alpha_\mathrm{A}(\omega)\right\} \mid \hat{\mathrm{n}}_\mathrm{A}\cdot\overleftrightarrow{\mathbf{G}}(\mathbf{r}_\mathrm{A},\mathbf{r}_\mathrm{D};\omega)\cdot\hat{\mathrm{n}}_\mathrm{D}\mid^2. \tag{4.14}$$

In order to be consistent with FRET literature [5], we recast Eq. (4.14) using the absorption cross section $\sigma_A^{abs}(\omega)$ of the acceptor and the emission spectrum of the donor $f_D^{em}(\omega)$ and normalize it by the power emitted by a single dipole in vacuum P_0,

$$\frac{P_{D\to A}}{P_0} = \frac{9c^4}{8\pi r_{DA}^6}\int \frac{f_D^{em}(\omega)\sigma_A^{abs}(\omega)}{\omega^4}T(\omega)\,d\omega \tag{4.15}$$

where $\sigma_A^{abs}(\omega) = \frac{\omega\mu_0 c}{3}\mathrm{Im}\left[\alpha_A(\omega)\right]$ and

$$T(\omega) = 16\pi^2k^4r_{DA}^6 \mid \hat{n}_A\cdot\overleftrightarrow{\mathbf{G}}(\mathbf{r}_A,\mathbf{r}_D;\omega)\cdot\hat{n}_D\mid^2 \tag{4.16}$$

From Eq. (4.15) it can be seen that the power transferred from the donor to the acceptor depends on the overlap between the spectra of the donor and acceptor modulated by the Green function. The effect of the electromagnetic environment on the energy transfer is contained within the Green function. The same conclusion is obtained from the quantum mechanical treatment Eq. (4.7) and the classical treatment Eq. (4.15).

The influence of the environment and the dipole orientations are embedded in $T(\omega)$. In free space using the Green function as defined in Eq. (2.39)

$$\begin{aligned}T(\omega) =&(1-k^2r_{DA}^2+k^4r_{DA}^4)(\hat{n}_A\cdot\hat{n}_D)^2\\ &+(9+3k^2r_{DA}^2+k^4r_{DA}^4)(\hat{r}_{DA}\cdot\hat{n}_D)^2(\hat{r}_{DA}\cdot\hat{n}_A)^2\\ &+(-6+2k^2r_{DA}^2-2k^4r_{DA}^4)(\hat{n}_A\cdot\hat{n}_D)(\hat{r}_{DA}\cdot\hat{n}_D)(\hat{r}_{DA}\cdot\hat{n}_A)\end{aligned} \tag{4.17}$$

where $\hat{r}_{DA}$ is the unit vector pointing from donor to the acceptor along $\mathbf{r}_A-\mathbf{r}_D$. For short distances in the near field $kr_{DA} < 1$, $T(\omega)$ is almost constant and the energy transfer Eq. (4.15) decays as r_{DA}^{-6}. It is the reason behind the well known distance dependence of FRET, the power transferred decays rapidly as r_{DA}^{-6} with the donor-acceptor separation. In the far field depending upon the orientation of the dipoles the power transfer may decay as r_{DA}^{-4} for longitudinal orientation of dipoles and r_{DA}^{-2} for transverse orientation of dipoles.

4.3 Antenna model for resonance energy transfer

In circuit theory the most basic donor-acceptor system is a two-port network. The two port network was analysed previously in Sec. 2.10.3. We now demonstrate that it is possible to study the energy transfer between two dipoles, by modeling it as two circuits linearly coupled through subwavelength antennas. We show that resonance energy transfer can be obtained through the mutual impedance of the two circuits.

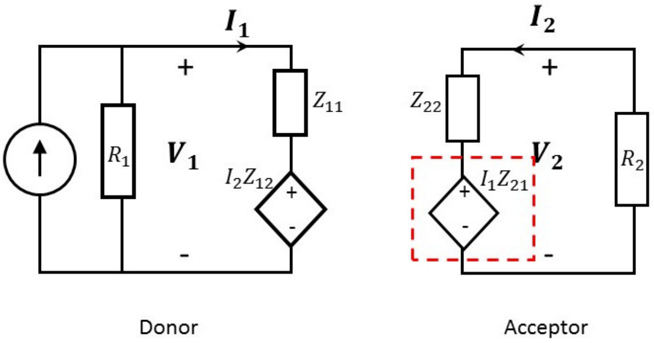

Figure 4.2: The two port network demonstrating a donor and an acceptor system

The two-port network which models the donor-acceptor system is shown in Fig. 4.2. Port 1 is labeled as donor and port 2 as acceptor. Donor and acceptor circuits have a purely dissipative, real resistance, R_1 and R_2 respectively, commonly referred to as reference impedances. Each port has a corresponding voltage and a current associated with it, namely V_1, I_1, V_2, and I_2. The driving current I_1 in donor port 1 can be assumed to be constant. Port 2 has no active source and acts as the acceptor thus, the whole system is driven by the source in the donor circuit. In acceptor circuit, the current I_2 and voltage V_2 are induced because of its coupling with port 1.

We assume that the coupling between the circuits is linear. Then, the currents and voltages in the two ports are then related through the complex impedance matrix $[Z_{ij}]$

$$\begin{pmatrix} V_1 \\ V_2 \end{pmatrix} = \begin{pmatrix} Z_{11} & Z_{12} \\ Z_{21} & Z_{22} \end{pmatrix} \begin{pmatrix} I_1 \\ I_2 \end{pmatrix}. \tag{4.18}$$

The diagonal elements Z_{ii} are generally associated with the reflection, while off diagonal elements $Z_{ij\neq i}$, determine the coupling between the two circuits. The voltage induced in acceptor port 2 due to its coupling with donor port 1 is $I_1 Z_{21}$, highlighted with a dashed red square in Fig. 4.2. In the absence of an active source this induced voltage acts as the source for acceptor circuit 2. A relation can then be obtained between the current induced in acceptor circuit I_2 and current in donor circuit I_1 using the Kirchoff's law

$$I_2 = -\left(\frac{Z_{21}}{R_2 + Z_{22}}\right) I_1. \tag{4.19}$$

Having established the relationship between the currents (Eq. (4.19)), the power transferred from the donor to the acceptor circuit is now derived.

The average power dissipated in any element in the circuit, with a voltage say, V across the element and a time harmonic current I flowing through it, is given by $P = (1/2)\mathrm{Re}[VI^*]$. As the voltage induced in port 2 due to its coupling with port 1 is $Z_{21}I_1$, the power transmitted from port 1 to port 2 is $P_{1\to2} = (1/2)\mathrm{Re}[(Z_{21}I_1)I_2^*]$. Replacing I_2 by I_1, using Eq. (4.19) we obtain,

$$\begin{aligned} P_{1\to2} &= \frac{1}{2}|I_1|^2|Z_{21}|^2\frac{\mathrm{Re}[Z_{22}+R_2]}{|Z_{22}+R_2|^2} \\ &= \frac{1}{2}|I_1|^2|Z_{21}|^2\frac{\mathrm{Re}[Z_{22}]}{|Z_{22}+R_2|^2} + \frac{1}{2}|I_1|^2|Z_{21}|^2\frac{R_2}{|Z_{22}+R_2|^2} \end{aligned} \tag{4.20}$$

Eq. (4.20) denotes the power transferred from the donor to the acceptor, it also provides an insight into how the power is used. The first term on the right hand side in Eq. (4.20) denotes the power radiated into the environment, while the second term denotes the power dissipated resistively in the acceptor.

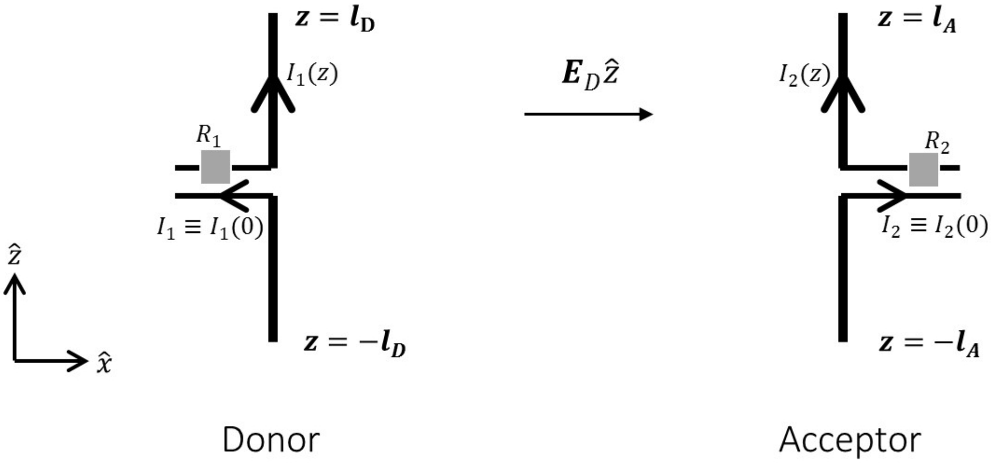

Figure 4.3: Dipole dipole interaction with subwavelength antennas.

Now we show that when the coupling between the two circuits is through two finite length sub-wavelengths antennas, the impedance Z_{21} of such a two-port network is related to the Green function $\overleftrightarrow{\mathbf{G}}(\mathbf{r}_A, \mathbf{r}_D; \omega)$. This allows us to investigate resonance energy transfer, in the context of antenna theory. Consider the donor-acceptor circuit in Fig. 4.2 coupled through two short electric dipole antennas such as shown in Fig. 4.3, composed of perfectly conducting wires of length l_D and l_A for the donor and acceptor respectively. For simplicity, in Fig. 4.3 we have illustrated both antennas to be pointing along $\hat{z}$. The donor dipole antenna is attached to circuit 1 while the acceptor dipole antenna is attached to circuit 2. The donor and acceptor dipole moments are, $\mathbf{p}_D = p_D\hat{n}_D$ and $\mathbf{p}_A = p_A\hat{n}_A$ respectively. As pointed out in Eq. (2.55) for a short dipole antenna the dipole moment and current are linearly related $I_1 = -i\omega p_D/l_D$ and $I_2 = -i\omega p_A/l_A$ thus

$$|I_{1(2)}|^2 = \frac{\omega^2}{l_{D(A)}^2}|p_{D(A)}|^2. \tag{4.21}$$

It is assumed both dipoles are fed through coaxial cables of impedance $50\ \Omega$. Thus the antenna loads $R_1 = R_2 = 50\ \Omega$ are the purely dissipative (real) and determined by the reference impedance of the coaxial cables.

The impedance Z_{21} is defined as the voltage induced at port 2 when the current flowing in port 2 is zero [111],

$$Z_{21} = \left.\frac{V_{2o}}{I_1}\right|_{I_2=0}, \tag{4.22}$$

where V_{2o}, is the voltage induced across port 2 if no current flows through port 2, which means that the reference impedance R_2 (load) is infinite and the dipole does not radiate. When the acceptor dipole antenna length $l_A \ll \lambda$ then, the electric field is linearly related to the voltage and we can express Z_{21}

$$Z_{21} = \frac{\hat{n}_A \cdot \mathbf{E_D}(\mathbf{r}_A) l_A}{I_1} = \frac{k^2 l_A l_D}{\varepsilon_0} \left[\hat{n}_A \cdot \frac{\overset{\leftrightarrow}{\mathbf{G}}(\mathbf{r}_A, \mathbf{r}_D; \omega)}{-i\omega} \cdot \hat{n}_D \right], \tag{4.23}$$

using the relationship between the currents and the dipole moments in Eq. (4.21)

$$Z_{21} = \frac{k^2 l_A l_D}{\varepsilon_0} \left[\hat{n}_A \cdot \frac{\overset{\leftrightarrow}{\mathbf{G}}(\mathbf{r}_A, \mathbf{r}_D; \omega)}{-i\omega} \cdot \hat{n}_D \right]. \tag{4.24}$$

Eq. (4.24) is a central result which relates the “two point" Green function $\overset{\leftrightarrow}{\mathbf{G}}(\mathbf{r}_A, \mathbf{r}_D; \omega)$ to the impedance Z_{21}, in a coupled circuit network system with realistic finite length dipole antennas. A similar relation between Green function and impedance was obtained in Ref. [33] but for studying LDOS.

Once the relationship between the impedance Z_{21} of a two port network, with short dipole antennas and the Green function is established (Eq. (4.24)), it is now possible to define a figure of merit which characterises the influence of the environment on the resonance energy transfer rate Γ_{DA} (Eqs. (4.7),(4.14)) in terms of the impedance Z_{21}

$$\frac{\Gamma_{DA}}{\Gamma_{DA}^{(0)}} = \frac{|\mathbb{G}_{DA}|^2}{|\mathbb{G}_{DA}^{(0)}|^2} = \frac{|Z_{21}|^2}{|Z_{21}^{(0)}|^2} \tag{4.25}$$

where, $\Gamma_{DA}^{(0)}$ is the resonance energy transfer rate in vacuum, $\mathbb{G}_{DA} = \hat{n}_A \cdot \overset{\leftrightarrow}{\mathbf{G}}(\mathbf{r}_A, \mathbf{r}_D; \omega) \cdot \hat{n}_D$, the subscript $_{DA}$ denotes the orientation of the dipole moments of the donor and acceptor, and $\mathbb{G}_{DA}^{(0)}$ is the Green function in vacuum. A similar figure of merit was recently used for studying FRET enhancement across a hyperbolic medium [57].

It is also instructive to derive the power transferred in a donor-acceptor antenna system. The polarizability $\alpha(\omega)$ of such a short dipole antenna of length l is of the same form as a small lossy scatterer [112],[136]

$$\frac{1}{\alpha(\omega)} = \frac{1}{l^2}[-i\omega(Z_{in} + R_L)] \tag{4.26}$$

where Z_{in} is the input impedance, R_L is the load. Using Eq.(4.26) we can find the relation between the imaginary part of the polarizability $\alpha_A(\omega)$ of the acceptor and the impedances which we express in a convenient form as,

$$\frac{\mathrm{Re}[Z_{22}] + R_2}{|Z_{22} + R_2|^2} = \frac{\omega}{l_A^2} \mathrm{Im}[\alpha_A(\omega)]. \tag{4.27}$$

If we substitute Eqs. (4.27) and (4.24) into Eq. (4.20) we recover the exact form of power transferred between dipoles as seen Eq. (4.14).

4.4 Resonance energy transfer measurement at microwave frequencies

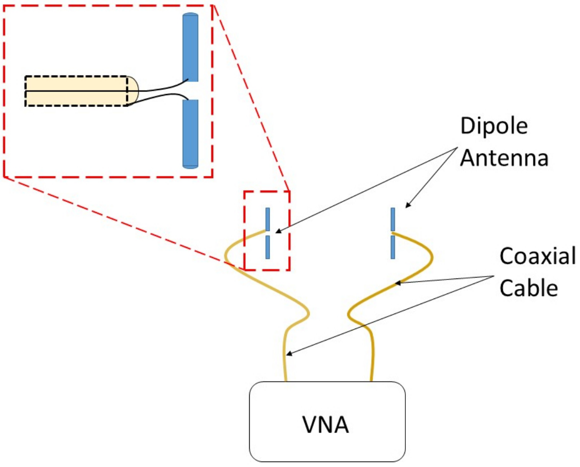

Figure 4.4: Setup for measurement of energy transfer between two dipoles at microwave frequencies with antennas.

At microwave frequencies it is possible to measure the power transferred between two antennas using a vector network analyser (VNA) as seen in Fig. 4.4. It is a more direct approach than conventional FRET experiments where the FRET rate is measured as the difference in the decay rates of the donor with and without an acceptor [5]. The impedances $[Z_{ij}]$ (i=1,2) can be measured directly through VNA, but its more common to measure the scattering parameters (S-Parameters) which relates the amplitudes of the incoming and outgoing waves through the coaxial cable. The impedances $[Z_{ij}]$ (i=1,2) can be completely known from S-Parameters and vice-versa [117].

The scattering coefficient S_{21} is the measure of the power dissipated in the resistance R_2 in the acceptor circuit as seen in Fig.4.2.

$$|S_{21}|^2 = \frac{1}{2}|I_1|^2|Z_{21}|^2\frac{R_2}{|Z_{22}+R_2|^2} \tag{4.28}$$

For a short dipole, as discussed previously $Re(Z_{22}) \ll R_2$ [33] and most of the power which is transferred into the acceptor circuit 4.20 is dissipated in R_2. Hence a measurement of $|S_{21}|^2$ in the near field is analogous to measuring FRET.

4.4.1 Difference from antenna based Purcell factor measurements

We wish to clearly point out the differences between Purcell factor measurements (Sec. 2.7) and resonance energy transfer measurements with antennas. The Purcell factor is the ratio of the change in the rate of spontaneous emission in the medium to vacuum $F = \gamma/\gamma_0$ and can be understood as the modification the radiative resistance of a subwavelength antenna $F = R_{rad}/R_{rad}^{(0)}$. For a small sub-wavelength antenna the radiative resistance is given by the real part of input impedance which corresponds to $\mathrm{Re}\{Z_{in}\} = \mathrm{Re}\{Z_{11}\}$ [33, 111]. The impedance Z_{11} is thus related to the *"one point"* Green function $\overset{\leftrightarrow}{\mathbf{G}}(\mathbf{r}_0, \mathbf{r}_0; \omega)$ where $\mathbf{r}_0$ is the location of the emitting dipole (Eq. (2.65)). This differs from resonance energy transfer measurements where the impedance Z_{21} is required. For DDI mediated resonance energy transfer, the *"two point"* Green function $\overset{\leftrightarrow}{\mathbf{G}}(\mathbf{r}_A, \mathbf{r}_D; \omega)$ is the relevant quantity. Another difference is that for Purcell factor measurements of the real part of impedance Z_{11} is required. Measuring the real part requires phase measurements in addition to magnitude measurements. On the other hand, for resonance energy transfer only measurements of magnitude of $|Z_{21}|$ suffice (Eq. (4.25)). The difficulty in microwave resonance energy transfer experiments, as we shall see in Chapter 5, is due to low signal to noise ratio. The highly sub-wavelength donor and acceptor antennas are required for accurate measurements. These antennas are poor emitters and receivers [111] which make the experiments challenging.

In this chapter we developed antenna models to investigate the energy transfer between a donor-acceptor pair. In the next Chapter 5, we shall apply this to experimentally measure resonance energy transfer with two antennas at microwave frequencies. In addition to measurements of resonance energy in vacuum, we shall also show that altering the modes of a cavity alters resonance energy transfer which can be measured with antennas.

Chapter 5

Resonance energy transfer measurements at microwave frequencies

In Chapter 4 we developed a classical analogue to resonance energy transfer between atoms using antennas. In a two-port network coupled with sub-wavelength dipole antennas, the impedance Z_{21} is related to the Green function $\overset{\leftrightarrow}{\mathbf{G}}(\mathbf{r}_A, \mathbf{r}_D; \omega)$ (Eq. (4.24)). It is thus possible to investigate resonance energy transfer by measuring the scattering coefficient S_{21}.

In this chapter we measure resonance energy transfer at microwave frequencies with antennas in vacuum (free-space) and in a parallel plate waveguide. In Sec. 5.1 we measure the resonance energy transfer between two antennas in vacuum, while changing the separation r_{DA} between the two antennas. We compare the measurements with analytical calculations. We demonstrate it is possible to recover both the near-field FRET, as well as the far field characteristics. In Sec. 5.2 we examine how resonance energy transfer is influenced in a parallel plate cavity. We demonstrate resonance energy transfer is modified by the electromagnetic mode structure of the cavity and the change can be measured with antennas. We find that the measurement results are in good agreement with analytical calculations.

5.1 Resonance energy transfer in vacuum

5.1.1 Experiments

We shall now apply our method, as developed in Chapter 4 to study resonance energy transfer between two dipole antennas in vacuum, while varying the separation distance r_{DA}. The advantage of this is that we can compare it with analytical calculations, as

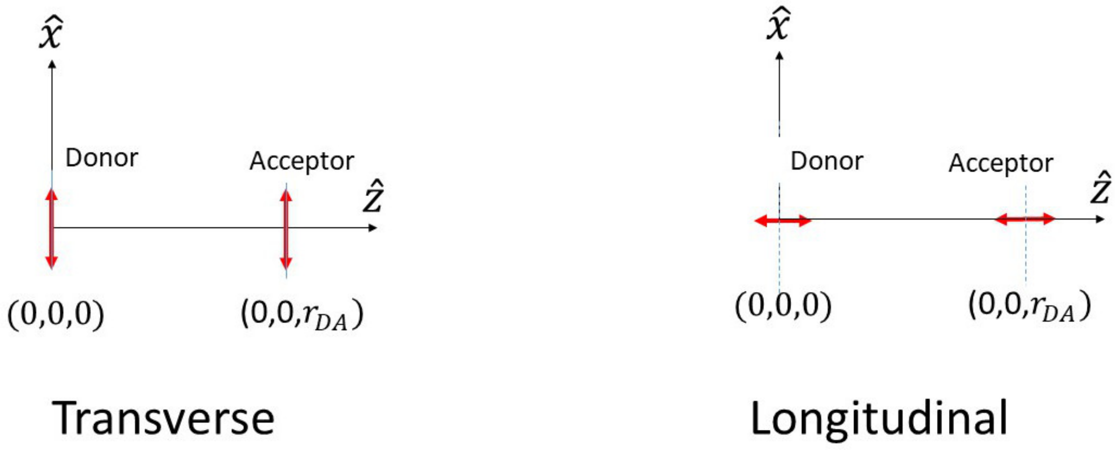

Figure 5.1: Schematic of resonance energy transfer experimental setup, illustrating the transverse and longitudinal orientation of dipole antennas.

the Green function is well known. We shall experimentally measure resonance energy transfer in two orientations of the antennas: transverse orientation and longitudinal orientation, as illustrated in Fig. 5.1. Even though vacuum is the simplest possible environment, the dependence of resonance energy transfer on r_{DA} differs in the near field ($k_0 r_{DA} < 1$) and far field ($k_0 r_{DA} > 1$), depending upon the orientation of the antennas have distinct characteristics. From the experiments with antennas we are able to measure the predicted features including the well known r_{DA}^{-6} dependence of FRET energy transfer in near field.

5.1.2 Finite dipole antenna length

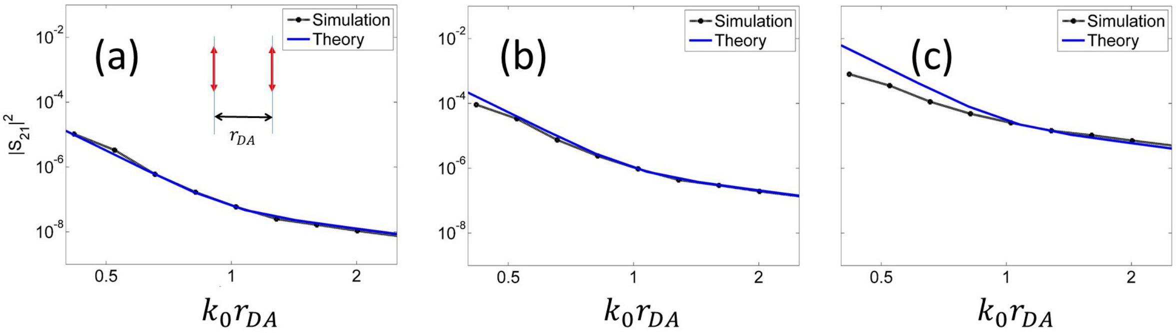

Figure 5.2: $|S_{21}|^2$ for a donor-acceptor antenna system in the transverse orientation (black, dashed), obtained with FDTD simulations, for antenna lengths (a) 10 mm, (b) 20 mm, and (c) 40 mm at 1 GHz, fitted with the theoretical Green function $|\hat{n}_A \cdot \overset{\leftrightarrow}{\mathbf{G}}(\mathbf{r}_A, \mathbf{r}_D; \omega) \cdot \hat{n}_D|^2$ (blue, solid).

In Fig. 5.2 we compare the $|S_{21}|^2$ at 1 GHz for donor-acceptor antennas, obtained from FDTD simulations, with the Green function for antenna lengths of 10, 20 and 40 mm. For all three lengths, there is excellent agreement between theory and simulations in the far-field regime $k_0 r_{DA} > 1$.

In the near field, the validity condition for agreement between energy transfer from the Green function calculations and finite antennas is $2l \ll r_{DA}$. Which is also the validity condition for the energy transfer is described as interaction between two electrostatic dipoles. This is indeed the case, as in the near-field, retardation is negligible and the scalar potential is the electrostatic potential. Hence, the validity condition that is applicable is the electrostatic validity condition. This is also consistent with FRET literature [2], where it is known that the Green function can be decomposed into a static part and a radiative part and, only the static part of the Green function is responsible for FRET. This helps us ascertain a suitable length of the dipole antenna for our measurements and we choose an antenna length of 10 mm. The antenna length of $2l = 10$ mm corresponds to $2l/\lambda \approx 0.03$ at 1 GHz.

The experimental setup for the measurement of resonance energy transfer for free space in vacuum is shown in Fig. 5.3. Two copper dipole antennas, each of length 10 mm, are fed through coaxial cables of reference impedance $50\ \Omega$ each. The donor dipole antenna is located at $\mathbf{r}_D = (0, 0, 0)$ while the acceptor antenna is located at $\mathbf{r}_A = (0, 0, r_{DA})$. Thus the separation is $\mathbf{r}_{DA} = \mathbf{r}_A - \mathbf{r}_D = r_{DA}\hat{z}$. Measurements were performed for two orientations of antennas, transverse and longitudinal. In the transverse orientation the antennas are oriented perpendicular to $\mathbf{r}_{DA} = r_{DA}\hat{z}$, with both donor and acceptor antennas oriented along $\hat{x}$. In the longitudinal orientation the antennas are oriented parallel to $\mathbf{r}_{DA}$ along $\hat{z}$.

As shown in Eq. (4.28) the power transferred from the donor to the acceptor antenna can be obtained through the scattering coefficient S_{21}. The scattering coefficient S_{21} is measured with a vector network analyser at frequency 1 GHz while varying the separation r_{DA} between the antennas. r_{DA} is varied in the range $k_0 r_{min} = 0.2$ to $k_0 r_{max} = 2$ with a fixed value of k_0 corresponding to frequency 1 GHz. The highly subwavelength antennas, are poor emitters and receivers of radiation. Thus, the maximum measurement distance r_{max} was limited by the noise and measurement limit of the VNA, while the minimum measurement distance r_{min} was limited by the size of the

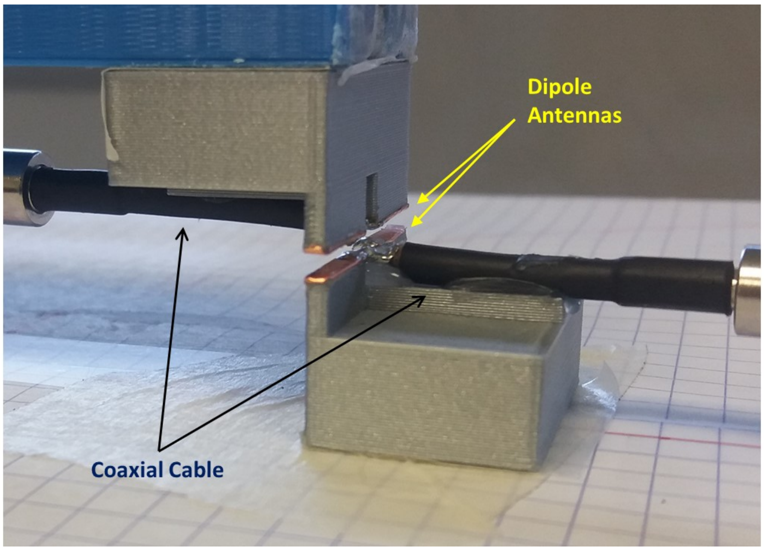

Figure 5.3: Experimental setup for resonance energy transfer measurement in free space, showing the copper dipole antennas attached to coaxial cables, in the transverse orientation.

antennas itself. Measurements were performed in an anechoic chamber.

The measurement results for $|S_{21}|^2$ varying with the distance r_{DA} between two antennas is presented Fig. 5.4. Measurements are compared to the theoretical Green function $|\hat{n}_A \cdot \overset{\leftrightarrow}{\mathbf{G}}(\mathbf{r}_A, \mathbf{r}_D; \omega) \cdot \hat{n}_D|^2$. In free-space the Green function was expressed in Eq. (2.39) with the real and imaginary parts [127], [106]

$$\begin{aligned}\mathrm{Re}[\overset{\leftrightarrow}{\mathbf{G}}^{(0)}(\mathbf{r}_A, \mathbf{r}_D; \omega)] = \frac{-k}{4\pi}\Bigg[(\delta_{ij} - 3\hat{\boldsymbol{r}}_i\hat{\boldsymbol{r}}_j)\left(\frac{\sin(kr_{DA})}{k^2r_{DA}^2} + \frac{\cos(kr_{DA})}{k^3r_{DA}^3}\right) \\ - (\delta_{ij} - \hat{\boldsymbol{r}}_i\hat{\boldsymbol{r}}_j)\frac{\cos(kr_{DA})}{kr_{DA}}\Bigg] \\ \mathrm{Im}[\overset{\leftrightarrow}{\mathbf{G}}^{(0)}(\mathbf{r}_A, \mathbf{r}_D; \omega)] = \frac{k}{4\pi}\Bigg[(\delta_{ij} - 3\hat{\boldsymbol{r}}_i\hat{\boldsymbol{r}}_j)\left(\frac{\cos(kr_{DA})}{k^2r_{DA}^2} - \frac{\sin(kr_{DA})}{k^3r_{DA}^3}\right) \\ + (\delta_{ij} - \hat{\boldsymbol{r}}_i\hat{\boldsymbol{r}}_j)\frac{\sin(kr_{DA})}{kr_{DA}}\Bigg]\end{aligned} \tag{5.1}$$

where $\hat{\mathbf{r}}_i$ represents the i^{th} component of the unit vector $\hat{r}_{DA} = \mathbf{r}_{DA}/|\mathbf{r}_{DA}|$.

Fig. 5.4 shows the measurement data for the transverse orientation fitted with the transverse Green function $A|\hat{x} \cdot \overset{\leftrightarrow}{\mathbf{G}}^{(0)}(r_{DA} + \delta r; \omega) \cdot \hat{x}|^2$ as seen in Eq. (5.1) where A and δr are obtained as fitting parameters. The fitting parameter A depends upon the initial power injected into the donor (excited) dipole, or in other terms accounts for the strength of the donor dipole moment $|\boldsymbol{\mu}_D|$. The distance correction distance δr is required because when the antennas are attached to coaxial cables. The feeding mech-

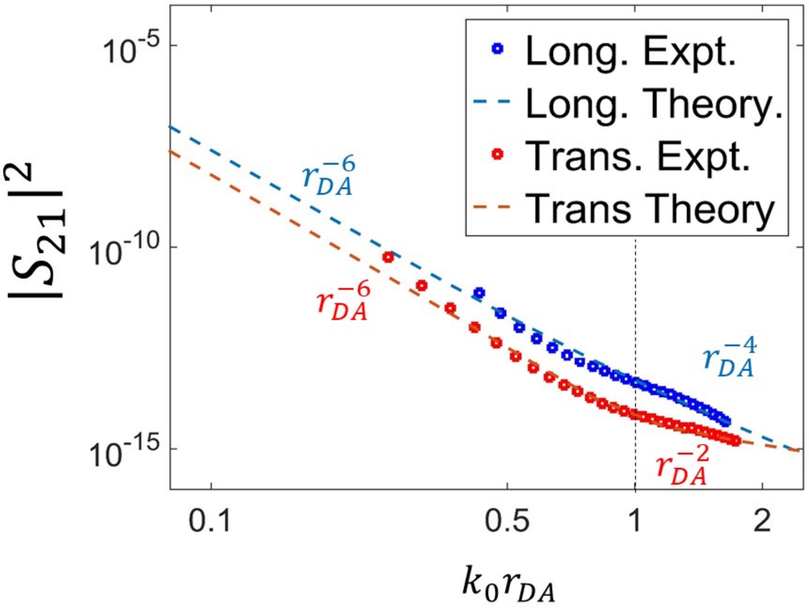

Figure 5.4: Measurements (dotted) of $|S_{21}|^2$ as a function of separation r_{DA} between the antennas, compared with theoretical Green function (dashed) in vacuum. For transverse orientation (red) and longitudinal orientation (blue) at frequency 1 GHz (λ=300 mm).

anism alters the center to center distance of antennas. The feeding point corrections were ascertained to be $\delta r = 5$ mm and $\delta r = 8$ mm for the transverse and longitudinal orientation experiments respectively. Since there are two antennas, δr corresponds to a corrections of $\delta r/2 = 2.5$ mm and $\delta r/2 = 4$ mm, at each antenna, for the transverse and longitudinal orientations. This is a reasonably small correction when compared to the wavelength $\lambda = 300$ mm. The feeding length correction δr would not be an issue for conventional microwave measurements with resonant antennas, where the distances are much larger compared to the antenna length. However, here antennas are subwavelength, with subwavelength separation distance between them, and the feeding correction is important.

We point out that in Fig. 5.4 the fit is only performed on the transverse data, to obtain the theoretical curve for the longitudinal data $A|\hat{z} \cdot \overset{\leftrightarrow}{\mathbf{G}}^{(0)}(r_{DA} + \delta r; \omega) \cdot \hat{z}|^2$ (dashed, blue in Fig. 5.4), the parameter A is remains unchanged from the fit obtained for transverse data. Fitting experimental data for only one orientation allows the comparison with the theoretically predicted ratio between the resonance energy transfer in the transverse and longitudinal orientations.

In the near field the $k_0 r_{DA} < 1$ power transfer decays as r_{DA}^{-6} for both transverse and longitudinal orientations. In the far field $k_0 r_{DA} > 1$ the power transfer between two dipoles decay as r_{DA}^{-4} and r_{DA}^{-2} for longitudinal and transverse orientations respectively. These features predicted through the Green function are confirmed through measurements. Thus, we can conclude that measurements of $|S_{21}|^2$ of a two port network, coupled via subwavelength antennas can be used to measure FRET at microwave frequencies.

5.2 Resonance energy transfer in parallel plate cavity

Now we investigate how resonance energy transfer depends upon the electromagnetic modes. We analyze the modification of resonance energy transfer with antennas in a parallel plate cavity with antennas. The effect of the modes on resonance energy transfer is studied by keeping the relative separation distance between the donor-acceptor antennas fixed while changing the separation L between the plates. The distance between the antennas is chosen such that measurements are performed the near-field regime, $k_0 r_{DA} < 1$. Through this experiment, we aim to measure the resonance energy transfer with antennas, inside ($L < \lambda/2$) and outside ($L < \lambda/2$) the cut-off regime of the waveguide. Studying FRET like near-field energy transfer between donor-acceptor in the cut-off is interesting, because in the cut-off regime, the LDOS $\rho = 0$ which inhibits spontaneous emission. The only channel (barring dissipation in heat) through which the donor can lose energy is near field transfer to the acceptor through evanescent waves. Here, measurements of $|S_{21}|^2$ are compared with the figure of merit for resonance energy transfer $|\mathbb{G}_{DA}|^2/|\mathbb{G}_{DA}^{(0)}|^2$ defined in Eq. (4.25), where the Green function is obtained analytically and also with FDTD simulations.

The setup as shown in Fig. 5.5, consists of two parallel, conducting plates in the x-y plane located at $z = 0$ and $z = L$. The donor-acceptor antennas are located at $(0, 0, L/2)$ and $(x, 0, L/2 + d)$ respectively. The dipole orientation of both antennas is along $\hat{x}$. The position of the donor antenna is always fixed at the center of the cavity $(0, 0, L/2)$ and we change the separation L between the plates. We point out that resonance energy transfer in this configuration has been studied previously theoretically using QED, where the real and imaginary parts of the Green function for this system were

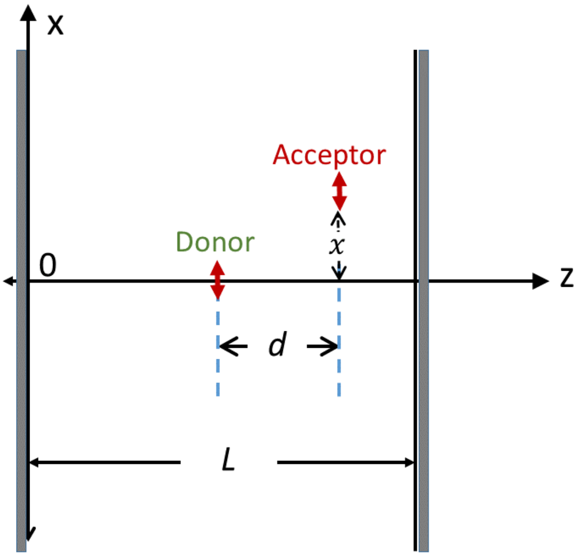

Figure 5.5: Schematic of setup to measure the influence of electromagnetic modes on resonance energy transfer.

calculated to be [137, 138]

$$\begin{aligned}\mathrm{Re}[\overleftrightarrow{\mathbf{G}}_{xx}(\mathbf{r}_A,\mathbf{r}_D,\omega)] = \frac{c^2}{\omega^2}\frac{\pi}{4}\Bigg\{ \frac{\pi}{L^3}\sum_{n_{odd}<n^*} \cos\frac{n\pi d}{L}\Big[&(n^{*2}+n^2)Y_0\left(\frac{\pi x}{L}\sqrt{n^{*2}-n^2}\right)\\ &+(n^{*2}-n^2)Y_2\left(\frac{\pi x}{L}\sqrt{n^{*2}-n^2}\right)\Big]\\ +\frac{2}{L^3}\sum_{n_{odd}>n^*}\cos\frac{n\pi d}{L}\Big[(-n^{*2}-n^2)K_0\left(\frac{\pi x}{L}\sqrt{n^2-n^{*2}}\right) &+ (n^{*2}-n^2)K_2\left(\frac{\pi x}{L}\sqrt{n^{*2}-n^2}\right)\Big]\Bigg\},\end{aligned} \tag{5.2}$$

$$\begin{aligned}\mathrm{Im}[\overleftrightarrow{\mathbf{G}}_{xx}(\mathbf{r}_A,\mathbf{r}_D,\omega)] = \frac{c^2}{\omega^2}\frac{\pi^2}{4L^3}\sum_{n_{odd}<n^*}\cos\frac{n\pi d}{L}\Big[&(n^{*2}+n^2)J_0\left(\frac{\pi x}{L}\sqrt{n^{*2}-n^2}\right)\\ &+(n^{*2}-n^2)J_2\left(\frac{\pi x}{L}\sqrt{n^{*2}-n^2}\right)\Big],\end{aligned} \tag{5.3}$$

where the subscript xx denotes that both donor and acceptor are along $\hat{x}$, $n^* = \lfloor 2L/\lambda \rfloor$ is the largest integer less than $2L/\lambda$. $Y_m(z)$, $J_m(z)$, and $K_m(z)$ are Bessel functions. Of these Bessel functions $Y_m(z)$, $J_m(z)$ represent propagating modes, whereas $K_m(z)$ is responsible for evanescent modes. From the Green function, modification of resonance energy transfer is then calculated by substituting Eqs (5.2), (5.3), (5.1) into Eq. (4.25) to obtain the ratio $|\mathbb{G}_{DA}|^2/|\mathbb{G}_{DA}^{(0)}|^2$.

The cavity is formed of two square steel plates with sides of length 200 cm. Measurements are performed at a frequency of 0.9 GHz, which corresponds to a wavelength of $\lambda = 33.33$ cm. Antennas are separated by a fixed distance $d = 1.8$ cm with $x = 0.1$ cm. The distance L between the plates is changed from $L = 10$ cm to $L = 60$ cm. The results are shown in Fig. 5.6. The variation in $|S_{21}|^2/|S_{21}^{(0)}|^2$, where $|S_{21}^{(0)}|^2$ is the reference in vacuum, from measurements is compared with FDTD simulations and analytical Green function calculations $|\mathbb{G}_{DA}|^2/|\mathbb{G}_{DA}^{(0)}|^2$.

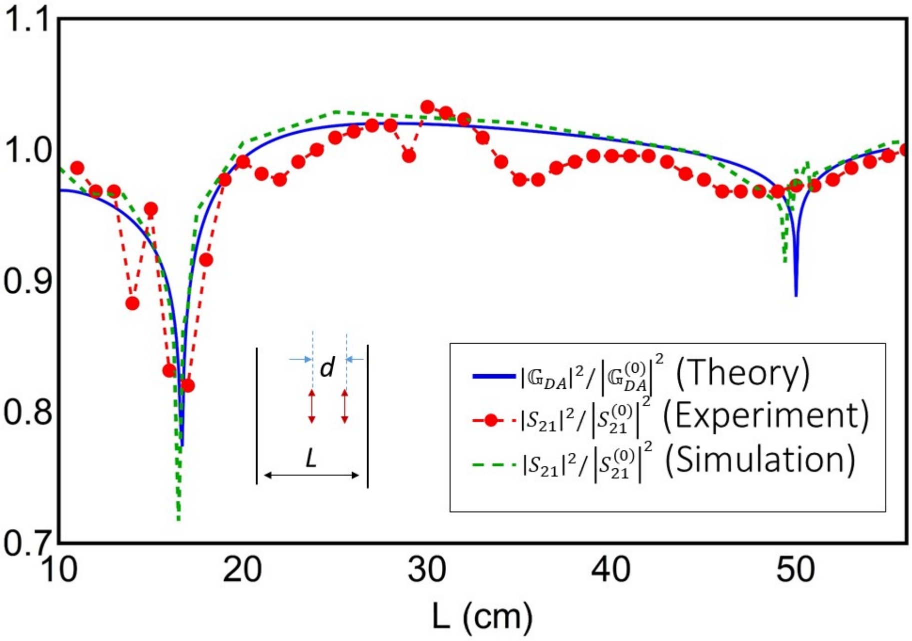

Figure 5.6: Comparison of resonance energy transfer rate between two dipoles inside a parallel plate waveguide as a function of the cavity width (L) as shown in Fig. 5.5. (Blue, solid) from theoretical Green function, (red) from antenna measurements, and (green) FDTD simulations. The antenna length is 10 mm with $\lambda = 33.33$ cm, $d = 1.8$ cm, and $x = 0.1$ cm.

For this system, the cut-off length of the waveguide corresponds to $L_c = \lambda/2 = 16.66$ cm. Thus, when $L < 16.66$ cm, the LDOS is zero (see Fig. A.1), however resonance energy transfer can also occur due evanescent modes (Eq. (5.2)). While, below the cut-off length $L < L_c$ spontaneous emission is inhibited, resonance energy transfer Fig. 5.6 is almost equal to that in vacuum as $|S_{21}|^2/|S_{21}^{(0)}| \approx 1$.

In Fig. 5.6 resonance energy transfer is suppressed at $L = 16.66$ cm and $L = 50$ cm, which correspond to $\lambda/2$ and $3\lambda/2$ respectively. It can be numerically shown to be caused by the destructive interference of large number of modes ranging up to $n = 1500$ (Eq. (5.2)) at $L = \lambda/2$ and $n = 4000$ at $L = 3\lambda/2$. We emphasize that the LDOS inside a parallel plate waveguide also has discontinuities at $L = \lambda/2$ and $L = 3\lambda/2$ (Fig. A.1) however, resonance energy transfer has no correlation to the LDOS for this system. In this system the separation d between the donor and acceptor causes the modes to interfere destructively at $L = \lambda/2$, suppressing resonance energy transfer.

Calculations of the Green function (Eqs. (5.2), (5.3)) show that for a different separation distance d, the modes can also interfere constructively and enhance the resonant energy transfer [137].

The discrepancy between analytical calculations and FDTD simulations is due to finite size effect of the plates. The analytical Green function Eqs. (5.2), (5.3) is obtained for infinitely large plates with point dipoles. For simulations and experiments the plate edge length was 200 cm, which is approximately equal to 6.6λ at 1 GHz. We checked numerically that edge length is sufficiently large to provide results similar to the infinitely large case. Another source of discrepancy is that the FDTD method itself is not the most ideal method for simulations inside cavities because of the large "ring-out" times. Achieving high accuracy with FDTD simulations requires long simulations times. Better agreement between FDTD simulations and theory can be achieved using shorter antennas, larger plates, and longer simulations times. In measurements (Fig. 5.6) we could observe the suppression in resonance energy transfer at $L = \lambda/2$, but not at $L = 3\lambda/2$, as predicted by analytical theory and FDTD simulations. Further investigation is required to address this and experiments are underway.

Chapter 6

Conclusion

Spontaneous emission and resonance energy transfer are processes that are generally attributed to atoms and molecules. It is interesting, that these processes can be controlled in a classical way. The spontaneous emission rate is determined by the local density of states, which in turn can be expressed using the classical electromagnetic Green function. As the impedance of a short dipole antenna is related to the Green function, the impedance is thus the quantity that links the classical formalism to the quantum mechanical formalism for studying the modification of spontaneous emission that is, the Purcell factor.

This study was designed at microwave frequencies, because antenna and its impedance at microwave frequencies, has been a well-researched topic in the field of electrical engineering. Measurements of the Purcell factor, with antennas, are made with short, subwavelength antennas, operating at frequencies far below their resonance frequencies. Under these conditions, the antennas are poor emitters and receivers of radiation. Hence, measurements involve extremely low powers. With the improvements in microwave measurement techniques, experiments are feasible at microwave frequencies.

The benefit of using antennas is that it naturally permits precise control of the location of the emitter and the orientation of its dipole moment. In this aspect, microwave experiments are preferable to optics experiments. As at optical wavelengths, the experiments are generally performed using an ensemble of fluorescent molecules, which offer limited control over the position and orientation of the dipole moment [139].

We applied the antenna impedance method to study the electric and magnetic Purcell factor in a hyperbolic metamaterial in the microwave frequency range 5-15 GHz (Chap. 3). Measuring the Purcell factor for different orientations of antennas, we obtained an understanding of the role of individual modes of the structure and their contribution to the density of states.

While the impedance-based formalism has been extended to study strong coupling phenomena [140], the scope of the thesis is limited only to the weak coupling regime. One of the limitations of using the impedance method is when measuring the magnetic Purcell factor with a magnetic dipole loop antenna, the method is unreliable near the anti-resonance frequency of the antenna, and we must be careful so as not to misinterpret the results.

In the second part of the thesis, we developed the antenna impedance analogy to study resonance energy transfer (Chap. 4). This is the first time such models have been developed to characterize resonance energy transfer. We measure resonance energy transfer in vacuum, and its modification inside a parallel plate waveguide at frequency 1 GHz. We demonstrate that resonance energy transfer can occur even in regimes where the LDOS is zero (Chap. 5).

While antenna impedance based methods were developed previously for measurement of the Purcell factor, they were not applied to study resonance energy transfer. By developing the theory and validating the predictions with experiments, this thesis fills that gap successfully. It is arguably the more interesting part of the thesis. It is also more interesting from the physics point of view. While studying spontaneous emission and LDOS, by definition we consider only the effect of modes which radiate to the far-field. However, in resonance energy transfer, depending upon the separation distance r_{DA} between the donor and acceptor dipole, the near-field, non-radiative, modes also participate in the exchange of the energy. It is this near-field, non-radiative, energy transfer, which is responsible for FRET.

For resonance energy transfer, microwave measurements hold a fundamental advantage, over optical measurement techniques. In FRET experiments at optical wavelengths made with fluorescent molecules, the energy transferred from the donor to the acceptor is ascertained through indirect measurements of changes in intensities or in lifetimes of fluorescent molecules. None of the techniques at optical wavelengths can directly measure the energy transfer because FRET is a near-field, dark process, mediated by virtual photons. On the other hand, microwave experiments as the antennas are attached to coaxial cables, a direct measurement of the energy transfer is possible.

One of the limitations of this work is that while developing antenna based models for resonance energy transfer, we considered the transition frequencies of the donor and acceptor to be the same. Our model does not account for the overlap between the donor emission spectrum and acceptor absorption spectrum as in actual FRET experiments, performed with fluorescent molecules [55]. It would be interesting if antenna based circuit models can be developed even further to provide an analogy to the role of the overlap of the spectrums in resonance energy transfer.

Several interesting studies using this method are possible. For example, it can be interesting to apply this method to study the modification of energy transfer in other interesting structures such as metamaterials, spherical resonators, and photonic crystals at microwave frequencies. In Chapter 4 only a single donor-acceptor pair was considered, using a similar scheme, a generalization to multiple emitter systems is also feasible.

The most crucial factor in resonance energy transfer experiments with antennas is their size. As the power transferred between dipoles scales as r_{DA}^{-6} in the near field, it is essential that the antenna lengths be highly subwavelength, to avoid finite length effects. We showed that (Fig. 5.2) in the near-field, even antennas as small as 40 mm for $\lambda = 300$ mm ($2l/\lambda \approx 0.13$) do not give accurate results. While an antenna of length 40 mm, would have been sufficiently subwavelength for measurement of the Purcell factor, for an accurate measurement of resonance energy transfer, we had to use even smaller antennas of length 10 mm ($2l/\lambda \approx 0.03$). Using smaller antennas, the experiments agree with theoretical predictions from the Green function. However, decreasing the size of the antennas decreases the amount of power they emit and absorb. Hence, it is important to judiciously choose an appropriate antenna length that reconciles the demand for the desired level of accuracy to the measurement capability of the experiments.

In this thesis, we have shown that antenna based methods successfully extend the range of studying LDOS and FRET from optical to microwave frequencies. This work provides a simple framework to characterize the influence of the electromagnetic environment on spontaneous emission and resonance energy transfer, with antennas, connecting the electrical engineering and quantum mechanical points of view.

Appendix A

LDOS in a parallel plate cavity.

The local density of states in a parallel plate waveguide has been studied previously in Ref. [141]. In a parallel plate waveguide as seen in Fig. (5.5), if an emitter is located at the center of the waveguide oriented along $\hat{x}$ at $z = L/2$, the rate of spontaneous emission (γ_{xx}) is given by [141]

$$\gamma_{xx} = \gamma_0 \left(\frac{3\lambda}{4L}\right) \sum_{n=1}^{\lfloor 2L/\lambda \rfloor} \left[1 + \left(\frac{n\lambda}{2L}\right)^2\right] \sin^2\left(\frac{n\pi z}{L}\right), \tag{A.1}$$

where γ_0 is the rate of spontaneous emission of the same emitter in vacuum, the subscript $_{xx}$ denotes the emitter is along $\hat{x}$.

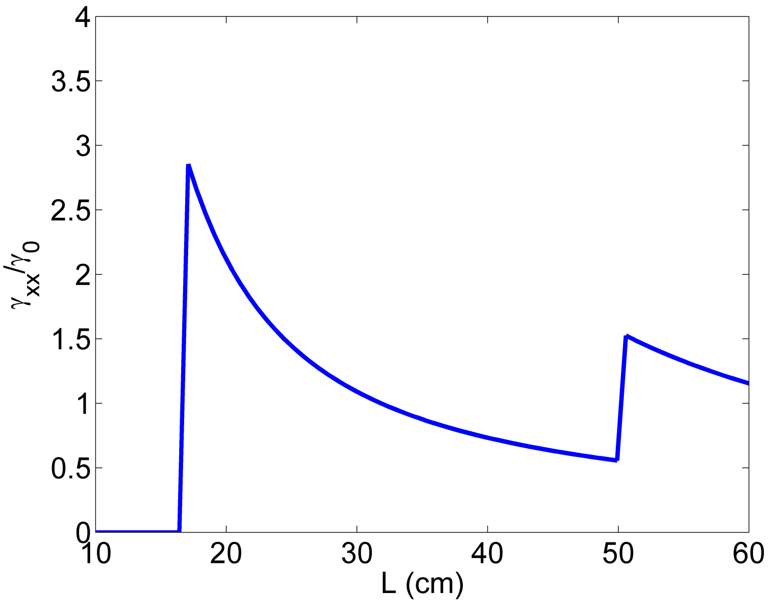

Figure A.1: The spontaneous emission in a parallel plate waveguide as seen in Fig. (5.5) normalised to vacuum as a function of the distance between the plates L. The emitter is located at the center of the waveguide oriented along $\hat{x}$ at $z = L/2$. The wavelength is taken to be $\lambda = 33.33$ cm.

The rate of spontaneous emission in a waveguide as a function of the separation between the parallel plates (L) is shown in Fig. (A.1) at $\lambda = 33.33$ cm. As we can see the LDOS enhanced, discontinuously at odd multiples of $L = \lambda/2$. The waveguide cutoff lies at $L < \lambda/2 = 16.66$ cm, when the separation between the plates of the waveguide $L < \lambda/2$ the emitter cannot emit because the local density of states (LDOS) is zero.

Appendix B

Strong coupling.

When we measured the magnetic Purcell factor in Sec. 3.5.1 we reported an anti-resonance frequency of the magnetic loop antenna observed as a peak in Fig. 3.9. We pointed out that this is analogous to the strong coupling regime. We wish to clarify at the onset that, while have some indication that strong coupling can also be observed with antennas, we have not performed a systematic study, which would be necessary for drawing any concrete conclusions.

While, in the weak coupling regime, the decay rate is much less than the frequency of the emitted photon $\gamma \ll \omega_0$. In the strong coupling regime, the emission rate of the emitter becomes comparable to the frequency of the emitted photon $\gamma \approx \omega_0$, the scattering from the emitter dominates over its coupling to the structure. The antenna impedance formalism is valid, and capable of quantitatively describing emission in the strong coupling regime [140]. While there is a substantial body of literature, studying the Purcell factor in the weak coupling regime, with antenna impedance, there are no existing systematic studies, theoretical or experimental, applying antenna impedance to study strong coupling.

The anti-resonance frequency of the antenna in the strong coupling regime depends upon the characteristics of the emitter and also its coupling with the structure. Hence, in principle, in the measurement of the magnetic Purcell factor, we should observe a shift in the anti-resonance frequency of the antenna, when placed in the structure. To study the shift in the resonance frequency, one can fit a Lorentzian function to the impedance and obtain the frequency at which the anti-resonance occurs, as the frequency at which the Lorentzian is centered. A simpler alternative is, through observing Eq. (3.5), that the anti-resonance frequency of the magnetic loop antenna

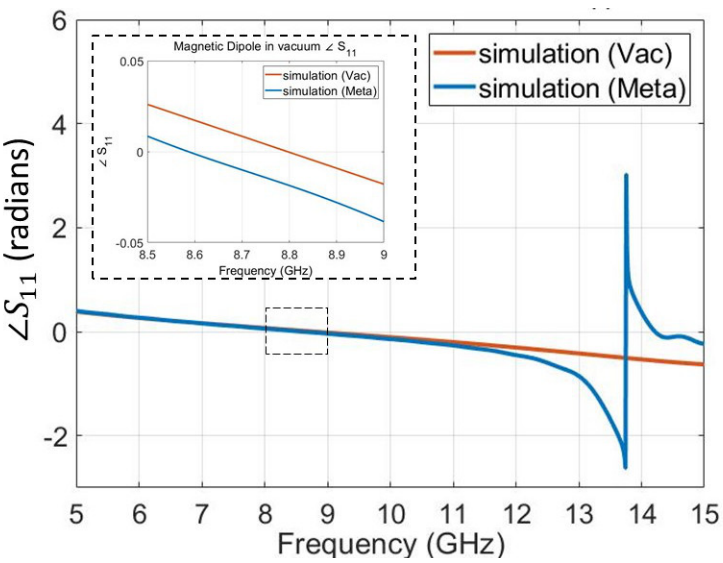

Figure B.1: Phase of scattering coefficient S_{11} for the magnetic loop antenna used for Purcell factor measurements in Sec. 3.5.1. In vacuum (orange) and in the metamaterial (blue).

occurs when the denominator $(1 - \mathrm{Re}(S_{11}))^2 + \mathrm{Im}(S_{11})^2 = 0$, the anti-resonance frequency corresponds to the frequency when the phase $\angle S_{11} = 0$. For the magnetic Purcell factor configuration in Sec. 3.5.1, the shift in the anti-resonance frequency can be seen in Fig. B.1. The inset, shows that the anti-resonance frequency (where $\angle S_{11} = 0$) is 8.8 GHz in vacuum which shifts to 8.6 GHz when the antenna is in the metamaterial. The shift in the anti-resonance frequency is not very large, but for future studies, it would be worthwhile to systematically characterize this frequency shift. By optimizing the structure and the antenna, we could have larger shifts of resonance frequency which could in principle be characterized and measured by the phase of S_{11} of the antenna. For the magnetic Purcell factor measurement, as used in Sec. 3.5.1, while the antenna is anti-resonant, the response of the structure is non-resonant. If the structure also demonstrates resonant features in the vicinity of the anti-resonance frequency of the antenna it could be interesting to explore if features analogous to Rabi splitting could be observed.

Appendix C

Mimicking electromagnetic wave coupling in tokamak plasma with fishnet metamaterials

MIMICKING ELECTROMAGNETIC WAVE COUPLING IN TOKAMAK PLASMA WITH FISHNET METAMATERIALS

K. Rustomji[1, 2], R.Abdeddaim[1], J.Achard[3], M.Chmiaa[1], E. Georget[4], M. Goniche[3], W. Helou[3], J.Hillairet[3], S. Enoch[1], G.Tayeb[1]
[1] *Aix Marseille Univ, CNRS, Centrale Marseille, Institut Fresnel, Marseille, France.*
[2]*Centre for Ultrahigh Bandwidth Devices for Optical Systems and Institute of Photonics and Optical Science, School of Physics, University of Sydney, Sydney, NSW 2006, Australia*
[3]*CEA, IRFM, F-13108 St-Paul-Lez-Durance, France.*
[4]*CEA-Saclay, DRF/I2BM/Neurospin/UNIRS, 91191, Gif-sur-Yvette Cedex, France.*

Keywords: Metamaterials, hyperbolic, anisotropy, LHCD antenna, lower hybrid wave coupling

Introduction

Tokamaks are expected to become the standard choice for magnetic confinement devices to produce nuclear fusion, an environmentally friendly solution for future large-scale energy supply. International projects such as ITER are leading the way in this field. To transfer energy into the plasma, dedicated radio frequency antennas are required. Their development and optimization requires the availability of a loading material that mimics the plasma. The electromagnetic properties of magnetically confined plasma are strongly anisotropic and different from any conventional material. We have designed and created a fishnet hyperbolic metamaterial that mimics these properties. This solution breaks a long-lasting bottleneck and will accelerate the development of high-frequency heating systems to be used in nuclear fusion.

The starting point is the fact that there is no available load able to simulate tokamak plasma, and consequently no way to test the antennas that will be used for heating or for current drive applications. The problem is to transfer power from the antenna to the plasma, and test these antennas under relevant conditions. The power transfer is related to the characteristics of the plasma at the tokamak edge (location of the antenna's mouth). The idea is to design and build a metamaterial to mimic the plasma. It appears legitimate to simplify the characteristics of the edge plasma by tending towards hyperbolic materials. This allowed us to design a metamaterial while freeing ourselves from the problems of spatial dispersion. We carried out measurements, which confirm the validity of this concept and of the numerical simulations. As a result, we now have a way to characterize and test the antennas. One of the other advantages is that these tests can be done at low power, without the need for elaborate sources or cooling. It should be noted that we do not intend to model with our metamaterials actual tokamak plasma, but only simplified plasma from the tokamak edge that retains the essential properties related to the coupling of the waves launched by the antenna to the plasma.

The coupling of LHRF waves to strongly magnetized plasmas is a critical issue for tokamaks as it often limits the RF power, which can be transferred from the antenna to the plasma. Development of new types of antennas to improve the ability of the antenna to handle large power in stationary conditions, as required on a fusion reactor, is hampered by the long and costly delay between the design and the feedback from experiments on large facilities such as tokamaks. Numerical codes that model both the plasma and the antenna are now available and provide an accurate characterization of the RF coupling. Before a full-scale test of the antenna on the plasma, the test of a mock-up with a load mimicking the plasma is believed to be a step forward by reducing the risks and accelerating the development process.

The magnetic configuration of a tokamak requires a strong DC current flowing along the plasma ring [1]. Generally, this current is inductively driven by the solenoid located on the tokamak axis. However, in order to achieve continuous operation of the reactor, an external source of current is needed. RF waves emitted from the plasma periphery are well fitted for this task when the wavevector spectrum is properly chosen in order to transfer the wave energy to the electrons of the plasma current (Fig. 1). Among these waves, lower hybrid range of frequency (LHRF) waves are a good candidate, thanks to their high current drive efficiency [2].

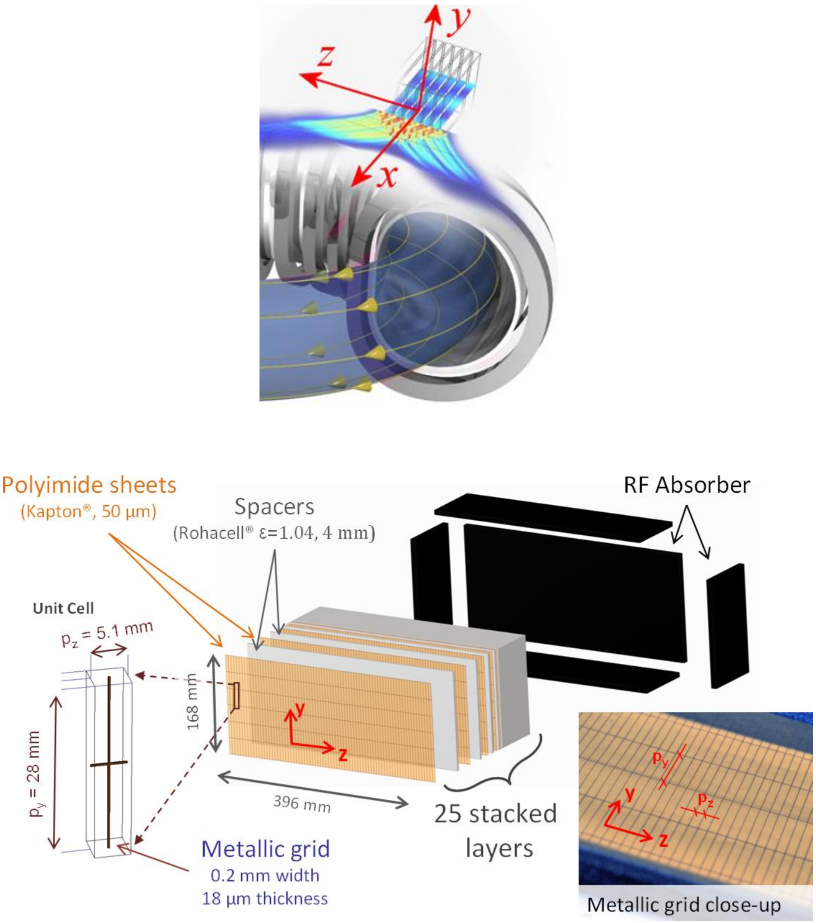
y
z
x
Polyimide sheets
(Kapton®, 50 µm)
Spacers
(Rohacell® ε=1.04, 4 mm)
RF Absorber
Unit Cell
p_z = 5.1 mm
p_y = 28 mm
168 mm
y
z
396 mm
25 stacked layers
Metallic grid
0.2 mm width
18 µm thickness
p_y
p_z
y
z
Metallic grid close-up

Fig. 1, Top: sketch of an antenna made of 6 waveguides, heating tokamak plasma (not to scale). The yellow lines depict the plasma current. For a picture of an actual set of waveguides feeding a tokamak, see the supplementary material.
Bottom: schematic view of the metamaterial fishnet load.

The dielectric tensor of magnetized plasma in the cold plasma approximation can be written in the form [3]:

$$\boldsymbol{\varepsilon} = \varepsilon_0 \begin{bmatrix} \varepsilon_\perp & \varepsilon_A & 0 \\ \varepsilon_A & \varepsilon_\perp & 0 \\ 0 & 0 & \varepsilon_{//} \end{bmatrix}$$

where the subscript // denotes the direction of the confinement magnetic field, i.e., the z-axis on Fig. 1.

In the case of LHRF waves of frequency $\omega_0/2\pi$ in the 1-8 GHz range, the electron density in the vicinity of the antenna has to be optimized to minimize the RF power reflected towards the generator and the electric field in the waveguides. This is achieved when the density n_e exceeds the cut-off density ($n_{\text{cut-off}}$ = $(\varepsilon_0\, m_e /e^2)\, \omega_0^2$) typically by a factor of 3. Under such conditions, the non-diagonal term ε_A is small ($\varepsilon_A \sim 0.1$) and $\varepsilon_\perp$ differs from 1 by less than 1%. Consequently, $\boldsymbol{\varepsilon}$ can be simplified using $\varepsilon_\perp \approx 1$ and $\varepsilon_A \approx 0$. The third parameter $\varepsilon_{//}$ is approximatively reduced to a Drude model $\varepsilon_{//} = 1 - \omega_{pe}^2/\omega_0^2 = 1 - n_e/n_{\text{cut-off}}$ where $\omega_{pe}/2\pi$ is the plasma frequency ($\omega_{pe}^2 = n_e\, e^2/(\varepsilon_0\, m_e)$).

To achieve good coupling conditions of the wave to the plasma, the relative permittivity in the direction of the magnetic field is negative ($\varepsilon_{//} < 0$). The density of the plasma layer facing the antenna is far from being spatially homogeneous and constant with time. There is usually a strong radial density gradient in the vicinity of the antenna. However, the simplification of the dielectric tensor ($\varepsilon_\perp \approx 1$ and $\varepsilon_A \approx 0$) still holds for the plasma layer close to the antenna, which matters for the coupling of the wave. In high performance plasma, instabilities occur in the plasma; the density at the plasma edge varies periodically with time from a low value ($\varepsilon_{//} \sim -1$) to a high value ($\varepsilon_{//} \sim -10$) [4] and can depart from the optimal coupling conditions achieved for $-3 < \varepsilon_{//} < -2$. If a medium mimicking a homogeneous plasma is well-suited to fully determining the properties of an RF antenna, a complete characterization would require several loads to cover the range of useful densities. We present here a metamaterial load that is close to optimal coupling conditions ($\varepsilon_{//} = -3$) for LHRF waves.

We are led to materials whose permittivity is diagonal, in the form $\boldsymbol{\varepsilon} = \varepsilon_0\, \mathrm{diag}(1,1,\varepsilon_{//})$, where $\varepsilon_{//} < 0$. These materials are called hyperbolic materials, since waves polarized in the *xy*-plane (TE polarization) behave as in a vacuum, whereas TM waves obey a hyperbolic dispersion relation (their dispersion curve is a hyperboloid) [5, 6]. In our case the field entering into the plasma from the antenna propagates in the *xz*-plane. See supplementary material for more details.

One way to obtain a material with a diagonal permittivity $\varepsilon = \varepsilon_0\, \mathrm{diag}(1,1,\varepsilon_{//})$ is to use an array of thin metallic wires that are parallel to the *z*-direction. Previous works [7, 8] have shown that $\varepsilon_{//}$ expresses using the Drude formula $\varepsilon_{//} = 1 - \omega_p^2/\omega_0^2$ with a plasma frequency ω_p depending on the wire's dimensions and spacing, at least when the wavelength is much greater than the wire's spacing, when the wavevector has no component along the *z*-direction, and when the electric field is parallel to the *z*-direction. Wire metamaterials have a strong spatial dispersion, i.e., ω_p (and consequently $\varepsilon_{//}$ and the response of the medium) depends on the wavevector component along the wire direction [9].

Considering our case of LHRF waves, in order to emit waves propagating inside the plasma, the antennas must generate waves where the wavevector has a non-null component along the z-axis. To this end, we use a phased array of waveguides that emits waves where the wavevector spectrum has *z*-components that are centered on $k_z = k_{//} \approx 2k_0 = 2\omega_0 / c$, a typical value for current drive applications in a tokamak. In this configuration, to mimic the plasma we need to manage the spatial dispersion of the metamaterial. Several solutions have been proposed for this [10]. We use the method of connecting the conducting wires of our metamaterial, which has been shown to limit the spatial dispersion [9]. We designed and tested a fishnet load composed of stacked thin metallic grid layers. The fishnet structure has the important practical advantage that it can be built layer by layer. This kind of construction was previously used by some of the authors for very low $\varepsilon_{//}$ medium to propagate a very low divergence beam in a vacuum [11,12], and more recently to control the density of states in hyperbolic metamaterials [13].

The fishnet metamaterial load is depicted in Fig. 1. It is made of a stack of thin copper grids. Each grid is parallel to the *yz*-plane with the following dimensions 0.2 mm width of the conductors along *y* or *z*, 18 μm thickness along *x*, periods p_y and p_z. The grids are printed on a 50 μm-thick polyimide film. They are spaced using Rohacell foam with low density (permittivity $\varepsilon = 1.04$) that gives a period p_x along the *x*-axis.

The electromagnetic properties of the structure strongly depend on these dimensions. To obtain a metamaterial with properties as close as possible to the expected hyperbolic material, we adjusted these parameters and tried to get dispersion curves as close as possible to those of a hyperbolic material with $\varepsilon_{//} = -3$. Due to the symmetry of the excitation versus *y*, the set of phased waveguides generates waves in the plasma that have a k_y component centered in $k_y = 0$; the k_y bandwidth can be reduced by increasing the dimension of the antenna along *y*, or by piling up several rows of waveguides. For this reason, we assume in the following that the spectrum of waves launched into the plasma has a negligible k_y component. Since the excitation is at a given frequency, all the electromagnetic characteristics of the material related to wave propagation are contained in the equi-frequency dispersion curve for the components k_x and k_z of the wavevector.

Fig. 2a shows the equi-frequency dispersion curves (k_x, k_z) for various dimensions of the fishnet cell. To get these curves, we enforced the electric field to have no component along the *y*-axis. This is consistent with the way the material is excited (TE_{10} mode inside the waveguides). The gray hyperbola is the dispersion curve of a homogeneous plasma with $\varepsilon_\perp = \varepsilon_{xx} = \varepsilon_{yy} = 1$ and $\varepsilon_{//} = \varepsilon_{zz} = -3$. Note that its equation is $\varepsilon_{xx}\, k_x^2 + \varepsilon_{zz}\, k_z^2 = \varepsilon_{xx}\, \varepsilon_{zz}\, k_0^2$, i.e., $k_x^2 - 3 k_z^2 = -3 k_0^2$. The colored curves show the dispersion curves of the fishnet metamaterials for several values of the period p_y. The two black vertical dashed lines are obtained when the wires along the *y*-direction are suppressed (the only wires are along the *z*-direction). As mentioned before, even if the effective parameters for a null z-component of the wavevector are correct, wire media fail to reproduce the dispersion relation of the homogeneous plasma for larger k_z values. For our application, we are interested in propagative waves with $k_z > k_0$, but no propagative waves exist inside the wire media for these wavevector values.

As shown in Fig. 2, for a fishnet metamaterial, the dispersion relation is not a perfect hyperbola. Thus, we had to make some choices: either choose parameters that give a curve as close as possible to the desired hyperbola in the range of k_z or choose parameters that fulfill some other physical properties. We chose to build a metamaterial that will give a direction of energy propagation close to that of homogeneous plasma. Note that the direction of energy propagation is normal to the dispersion curve [14]. Since the phased waveguide antenna launches waves with $n_{//} = k_z / k_0 \approx 2$, we retained the parameters associated with the green dispersion curve (Fig. 2b). This is a good compromise between a curve close to the hyperbola and one that gives for $k_z / k_0 \approx 2$ the same energy propagation direction as the homogeneous plasma (magenta arrows).

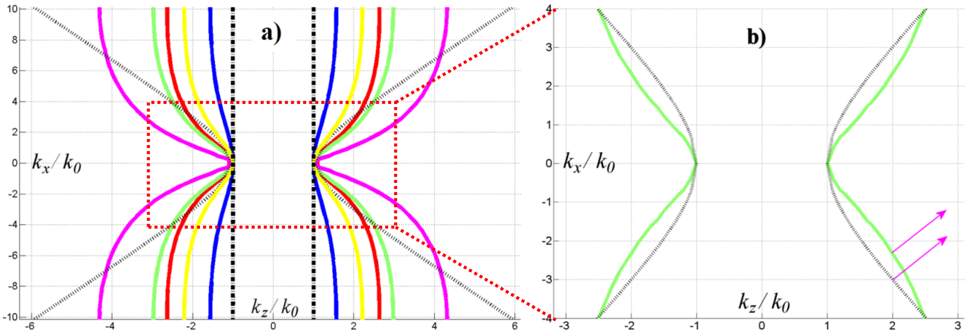

Fig. 2. Equi-frequency dispersion curves at 3.7 GHz. ***a)*** *The gray hyperbola is the dispersion curve of a hyperbolic material with* $\varepsilon_{\perp} = 1$ *and* $\varepsilon_{//} = -3$. *The colored curves are the dispersion curves of the grid-made metamaterial with periods* $p_x = 4\,\mathrm{mm}$, $p_z = 5.1\,\mathrm{mm}$, *and* p_y *varying from 10 mm, 20 mm, 25 mm, 28 mm, 35 mm for blue, yellow, red, green and magenta curves respectively. The dashed black vertical lines correspond to the wired media.* ***b)*** *Enlargement of the curve for* $p_y = 28\,\mathrm{mm}$. *The arrows show the average direction of energy propagation for* $k_z = 2k_0$.

The configuration is shown in Fig. 1. The dimensions of the grid layers are 396 mm (along the *z*-direction) × 168 mm (along the *y*-direction). To reduce the parasitic reflections of the electromagnetic field at the boundaries of the fishnet load, we surrounded the load by a 30-mm thick RF absorber foam on five of its faces, the sixth being the one where the waveguides feed the load.

The antenna exciting the LHRF wave is composed of one input waveguide feeding 6 narrow phased waveguides stacked along the *z*-direction (see Fig. 3). This type of antenna, called a multi-junction antenna, allows reduction of the reflection coefficient in the input principal waveguide at the expense of an increase of the electric field in the narrow waveguides compared to a conventional antenna. The field emitted by this antenna has a spectrum centered on $n_{//} = k_z / k_0 \approx 2$. Consequently, there is no propagation inside the vacuum, a high reflection coefficient, and a high standing-wave ratio (SWR) inside the antenna, as shown in Fig. 3 left. Propagation inside the plasma is allowed according to Fig. 2(b). In this case, the SWR inside the antenna is low (Fig. 3, middle). The modeling depicted in Fig. 3 (right) shows that the fishnet metamaterial load that we designed preserves these properties similar emitted field and low SWR.

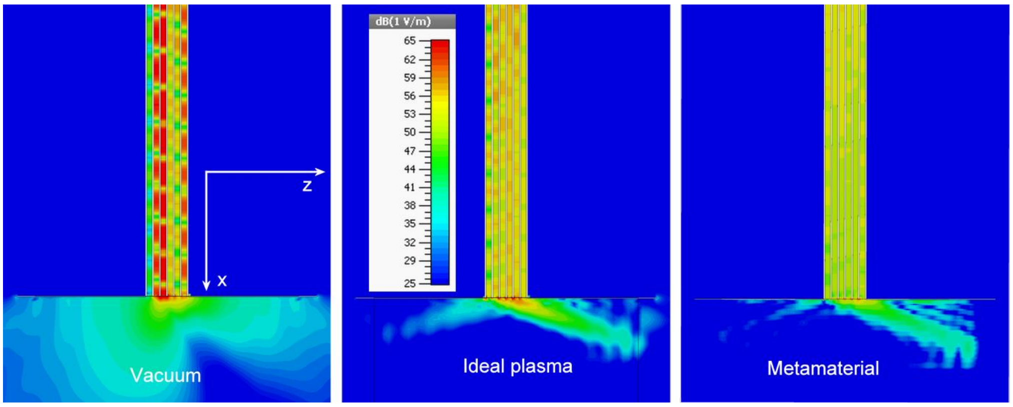

Fig. 3. Numerical modeling of the modulus of the electric field at 3.7 GHz. The multi-junction antenna mouth is surrounded by a ground plane mimicking the tokamak vessel wall (horizontal line on these graphs). The field map is in the middle of the antenna (y = 0 according to Fig. 1). The multi-junction antenna is loaded with vacuum (left), an ideal plasma with $\varepsilon_{\perp} = 1$ *and* $\varepsilon_{//} = -3$ *(middle), and the fishnet metamaterial (right). A high resolution version of this graph showing the entire multi-junction antenna is given in supplementary material*.

To quantify the ability of our structure to fit to the plasma behavior, we measured the reflection coefficient S_{11} of the multi-junction antenna, and compared it (Fig. 4) to simulations using both CST Microwave Studio and the open-source code ALOHA [15]. CST is a full-wave frequency solver while ALOHA is a mode-matching code where the electromagnetic waves are fully absorbed in idealized semi-infinite plasma, which explains the small discrepancies between their results. We call d_{vac} the gap distance between the antenna and the load. As expected S_{11} is low when the metamaterial is close to the antenna and increases with d_{vac}. Considering that in this case the results given by ALOHA have an uncertainty of approximately ±2 dB, one can note that there is a good agreement between the measurements and the modeling.

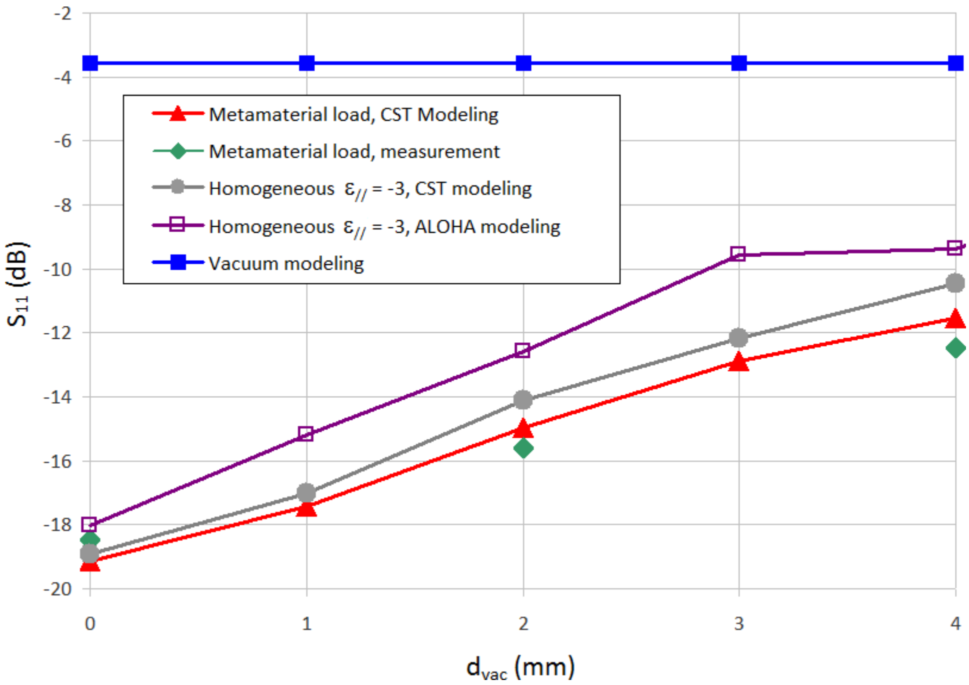

Fig. **4**: *Reflection coefficient as a function of the gap between the antenna and the metamaterial load* d_{vac}. *We also give the value of* S_{11} *when the antenna radiates in a vacuum.*
In the figure caption, "$\varepsilon_{//} = -3$*" stands for the homogeneous load with* $\varepsilon_{//} = -3$ and $\varepsilon_{\perp} = 1$.

The map of the magnetic field propagating from the antenna to the medium was constructed from the measurements (Fig. 5) and compared to the simulations. The main lobe of the launched spectrum ($n_{//} = 2$) is propagating along an angle α with the parallel direction (*z*-axis). The angle is given by

$\alpha = \tan^{-1}\left(\frac{\varepsilon_{xx}(\varepsilon_{xx} - n_z^2)}{\varepsilon_{zz}\, n_z^2}\right)^{1/2} \approx 27\ \mathrm{deg}$, whereas the measurement gives α = 29 deg. The Fourier transform of the field emitted by the antenna leads to secondary $n_{//}$ lobes. The details are given in supplementary information. The highest amplitude secondary mode is for $n_{//} = -6$. This mode can be seen on Fig. 5c, and it propagates towards increasing *z*. In the case of the metamaterial, we can see from Fig. 2 that for $n_{//} = k_z / k_0 = -6$ there is no existing propagative mode, and consequently the field is evanescent and decays rapidly ~ -25 dB below the main lobe amplitude (Fig. 5a and 5b) whereas it is about -10 dB for a homogeneous plasma for which a propagative mode exists (Fig. 5c).

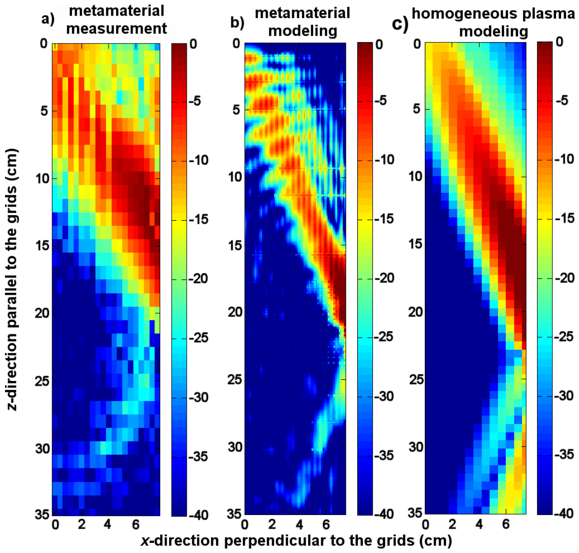

Fig. 5: Magnetic field map with the metamaterial load: a) experiment, b) modeling. The modeling of the equivalent plasma ($\varepsilon_{//} = -3$) is shown in c).

Discussion

We numerically and experimentally show that the metamaterial load we designed matches well the properties of a homogeneous plasma with equivalent hyperbolic dielectric tensor, resulting in low reflection or low insertion losses for a typical LHRF antenna with $n_{//} = 2$. Experimental measurements and numerical modeling of magnetic field maps show that waves propagate in the anisotropic medium ($\varepsilon_{//} = -3$, $\varepsilon_{\perp} = 1$) along the expected directions. Thus, the metamaterial load will provide a drastic simplification for development of tokamak antennas and will help to make tokamak technology more efficient.

We envision many different versions and improvements. In a next step, two loads at 5 GHz with $\varepsilon_{//} = -10$ and -1 will be manufactured using the same scheme. These loads will be tested with a simple 4-waveguide antenna.

New concepts of antenna will also be tested with these loads. From a longer term perspective, several refinements can be proposed. For instance, a load mimicking a typical density gradient along the *x*-axis (radial) of a tokamak plasma near the antenna ($\Delta\varepsilon_{//}/\Delta x$ ~ -10/5 cm) can be obtained by continuously varying the dimensions of the metallic grid across the 25 layers. Gyrotropic properties that we neglected, but could be important for some frequency ranges could also be simulated by specific metamaterials structures [16, 17]. Moreover, active metamaterials could reproduce the dynamics and instabilities of the plasma [18]. Finally, such anisotropic structures can be used in optical domain to enhance spontaneous emission, negative refraction and superlensing effects [5].

Methods

The load is tested with a 6-waveguide multi-junction-type antenna module. The individual waveguides (dimensions 8 mm×72 mm) are phased with built-in phase shifters ($\Delta\Phi = \pi/2$) in order to launch a wave with a parallel wave index centered on $n_{//} = 2.0$. The height of the waveguides is such that all modes, except TE_{10}, are evanescent. Due to the limited number of waveguides the $n_{//}$ spectrum is rather broad $(\Delta n_{//})_{\text{mid-height}} = \lambda_0 / L_{//,\text{ant}} \approx 1$. A detailed analysis of the emitted spectrum is presented in supplementary material and shows that in addition a secondary lobe exists for $n_{//} = -6$. The distance between the antenna and the load, which is terminated by one half of a period $p_x / 2$ of foam layer, needs to be accurately tuned as the wave ($n_{//} > 1$) is evanescent in vacuum/air with an evanescent length in the mm range. However, because of the rather poor flatness and thickness accuracy of the layers of spacers and absorbers, the mean gap cannot be controlled with accuracy better than 0.5-1 mm.

The RF field in the load was measured in a plane at mid-height of the waveguides ($y = 0$) where the amplitude of the TE_{10} mode is the highest. The field was measured with a magnetic loop (ϕ = 3 mm) inserted inside the load through empty channels hollowed in the foam.

The experimental results are compared to those obtained by full wave modeling, using either an open-source code ALOHA including a plasma module [15] or a commercial RF code CST Microwave Studio, which can also describe the wave propagation in homogeneous plasma.

Acknowledgements

This work is partially supported by the Région Provence-Alpes-Côte d’Azur (Project DEB 13-1464).

This work was carried out thanks to the support of the A*MIDEX project (n◦ ANR-11-IDEX-0001-02) funded by the Investissements d’Avenir French Government program, managed by the French National Research Agency (ANR). Research was conducted within the context of the International Associated Laboratory “ALPhFA: Associated Laboratory for Photonics between France and Australia”.

References

[1] Ongena, J., Koch, R., Wolf, R., & Zohm, H. (2016). Magnetic-confinement fusion. Nature Physics, 12(5), 398-410.

[2] Stevens, J., Ono, M., Horton, R., & Wilson, J. R. (1981). Edge density profile effects for lower hybrid waveguide coupling. Nuclear Fusion, 21(10), 1259.

[3] T.H. Stix, Waves in plasmas, AIP-Press, 1992.

[4] Goniche M. et al., SOL characterization and LH coupling measurements on JET in ITER-relevant conditions, Plasma Phys. Control. Fusion 51 044002 (2009).

[5] Poddubny, A., Iorsh, I., Belov, P., & Kivshar, Y., Hyperbolic metamaterials, Nature Photonics 7, 948-957 (2013).

[6] L. Ferrari et al., Hyperbolic metamaterials and their applications, Progress in Quantum Electronics 40 (2015) 1–40.

[7] G. Guida, D. Maystre, G. Tayeb, and P. Vincent, "Mean-field theory of two-dimensional metallic photonic crystals," J. Opt. Soc. Am. B 15, 2308-2315 (1998).

[8] J. B. Pendry, A. J. Holden, W. J. Stewart, and I. Youngs, Extremely Low Frequency Plasmons in Metallic Mesostructures, Phys. Rev. Lett. 76, 4773 (1996).

[9] P. A. Belov, R. Marqués, S. I. Maslovski, I. S. Nefedov, M. Silveirinha, C. R. Simovski, and S. A. Tretyakov, Strong spatial dispersion in wire media in the very large wavelength limit, Phys. Rev. B 67, 113103 (2003).

[10] Demetriadou A. & Pendry J.B, Taming spatial dispersion in wire metamaterial, J. Phys. Condens. Matter 20 (2008) 295222.

[11] Enoch, S., Tayeb, G., Sabouroux, P., Guérin, N., & Vincent, P. , A Metamaterial for Directive Emission, Phys. Rev. Lett. 89, 213902 (2002)

[12] Ourir, A., Abdeddaim, R., & de Rosny, J., Planar metamaterial based on hybridization for directive emission. Optics express, 20(16), 17545-17551 (2012).

[13] Rustomji, K., Abdeddaim, R., de Sterke, C. M., Kuhlmey, B., & Enoch, S. Measurement and simulation of the polarization-dependent Purcell factor in a microwave fishnet metamaterial, Phys. Rev. B **95**, 035156 (2017).

[14] Boris Gralak, Stefan Enoch, and Gérard Tayeb, "Anomalous refractive properties of photonic crystals," J. Opt. Soc. Am. A 17, 1012-1020 (2000).

[15] Hillairet J. et al., ALOHA: an Advanced LOwer Hybrid Antenna coupling code, Nucl. Fusion 50 (2010) 125010. https://github.com/jhillairet/ALOHA

[16] Wang, Z., Wang, Z., Wang, J., Zhang, B., Huangfu, J., Joannopoulos, J. D., Soljacic, M., Ran, L. (2012). Gyrotropic response in the absence of a bias field. Proceedings of the National Academy of Sciences, 109(33), 13194-13197.

[17] Rogacheva, A. V., Fedotov, V. A., Schwanecke, A. S., & Zheludev, N. I. (2006). Giant gyrotropy due to electromagnetic-field coupling in a bilayered chiral structure. Physical Review Letters, 97(17), 177401.

[18] Zheludev, N. I., & Kivshar, Y. S. (2012). From metamaterials to metadevices. Nature Materials, 11(11), 917-924.

SUPPLEMENTARY INFORMATION

Propagation inside the plasma

The axes *x*,*y*,*z* are those used in the previous part of the paper (see Fig. 1) and $(\mathbf{e}_x,\mathbf{e}_y,\mathbf{e}_z)$ are the unit vectors along these axes.

We consider, inside a medium with permittivity

$$[\varepsilon]=\begin{bmatrix}\varepsilon_{xx} & 0 & 0\\ 0 & \varepsilon_{yy} & 0\\ 0 & 0 & \varepsilon_{zz}\end{bmatrix}$$

the propagation of a plane wave with electric field (time dependence in $\exp(-i\omega t)$)

$$\mathbf{E}(x,z)=\mathbf{E}_0\exp\left(i\,\mathbf{k}\bullet\mathbf{r}\right)$$

where $\mathbf{k}=k_0(n_x\mathbf{e}_x+n_z\mathbf{e}_z)$.

The wave equation

$$-\mathbf{k}\times\left(\mathbf{k}\times\mathbf{E}\right)=k_0^2\left[\varepsilon\right]\mathbf{E}$$

leads to

$$\begin{bmatrix}\varepsilon_{xx}-n_z^2 & 0 & n_xn_z\\ 0 & \varepsilon_{yy}-n_x^2-n_z^2 & 0\\ n_xn_z & 0 & \varepsilon_{zz}-n_x^2\end{bmatrix}\begin{bmatrix}E_x\\ E_y\\ E_z\end{bmatrix}=0$$

This equation splits into two separate equations:

$$\left(\varepsilon_{yy}-n_x^2-n_z^2\right)E_y=0 \qquad (1.1)$$

and

$$\begin{bmatrix}\varepsilon_{xx}-n_z^2 & n_xn_z\\ n_xn_z & \varepsilon_{zz}-n_x^2\end{bmatrix}\begin{bmatrix}E_x\\ E_z\end{bmatrix}=0 \qquad (1.2)$$

The solutions of the first equation (1.1) are plane waves with electric field parallel to $\vec{e}_y$ and their dispersion relation is that of a homogeneous media with permittivity ε_{yy}:

$$n_x^2+n_z^2=\varepsilon_{yy}$$

In our present problem, we can consider that these waves are not present, because the antenna generates almost no wave with this polarization.

The second equation (1.2) admits solutions $\mathbf{E}=\left(E_x,0,E_z\right)$ polarized in the plane $(\vec{e}_x,\vec{e}_z)$, provided that its determinant vanishes, which gives their dispersion equation:

$$\varepsilon_{xx}n_x^2+\varepsilon_{zz}n_z^2=\varepsilon_{xx}\varepsilon_{zz}$$

Spectrum generated by phased waveguides

In this appendix, we give a rough description of the spectrum of the waves launched into the plasma by a set of phased waveguides. The waveguides are in the half space $x<0$, their terminations are in the plane $x=0$, and we assume that anywhere else in this plane $x=0$ there is a perfect conducting plate. The field emitted by these waveguides is launched in the half-space $x>0$. We make some simplifying hypotheses; we assume that the waveguides apertures are infinitely extended along the *y*-axis. This means that the problem becomes *y*-independent, and the field emitted can be written as a plane wave packet

$$\mathbf{E}(x,z)=\int_{-\infty}^{+\infty}\mathbf{A}(k_z)\exp\big(i(k_x x+k_z z)\big)dk_z$$

We denote by *b* the waveguide aperture along the *z*-axis. We denote by Δz the distance between the centers of two adjacent waveguides along the *z*-axis. We denote by $\Delta\phi$ the phase shift between the fields emitted by two adjacent waveguides. We denote by *N* the numbers of waveguides (N = 6 and $\Delta\phi=\pi/2$ in our practical case).

We assume that the electric field in the waveguide termination has constant amplitude and a linear polarization along *z*.

If we denote by $\Pi(u)$ the rectangular function with width *b*, equal to 1 for $-b/2<u<b/2$ and vanishing anywhere else, the electric field in the plane $x=0$ where the waveguides end is the function

$$E_z(x=0,z)=\sum_{n=1}^{N}\exp(in\,\Delta\phi)\,\Pi(z-n\,\Delta z)$$

The spectrum $A_z(k_z)$ emitted by the set of waveguides in the half-space $x>0$ is such that

$$E_z(0,z)=\int_{-\infty}^{+\infty}A(k_z)\exp\big(ik_z z\big)dk_z$$

and consequently

$$A(k_z)=\frac{1}{2\pi}\int_{-\infty}^{+\infty}E_z(0,z)\exp\big(-ik_z z\big)dz$$

After some calculations, and putting

$$k_z=k_0\,n_z=\frac{2\pi}{\lambda_0}n_z$$

$$X=\exp\big(i(\Delta\phi-k_0\,\Delta z\,n_z)\big)$$

we get

$$A(n_z)=\frac{X^{N+1}-X}{X-1}\;\frac{b}{2\pi}\;\frac{\sin\left(\frac{k_0\,b\,n_z}{2}\right)}{\frac{k_0\,b\,n_z}{2}}$$

Finally, if we put

$$\operatorname{sinc}(x)=\frac{\sin(\pi x)}{\pi x}$$

the spectral density of the waves launched by the set of waveguides is

$$\left|A(n_z)\right|^2=\left|\frac{X^{N+1}-X}{X-1}\right|^2\left(\frac{b}{2\pi}\right)^2\operatorname{sinc}^2\left(\frac{b\,n_z}{\lambda_0}\right)$$

The following figure gives the spectral density at 3.7 GHz in two cases:

a) $N=6$ waveguides with width $b=8\,\text{mm}$, spacing $\Delta z=10\,\text{mm}$ and phase shift $\Delta\phi=\pi/2$

b) $N=1$ waveguide with width $b=8\,\text{mm}$

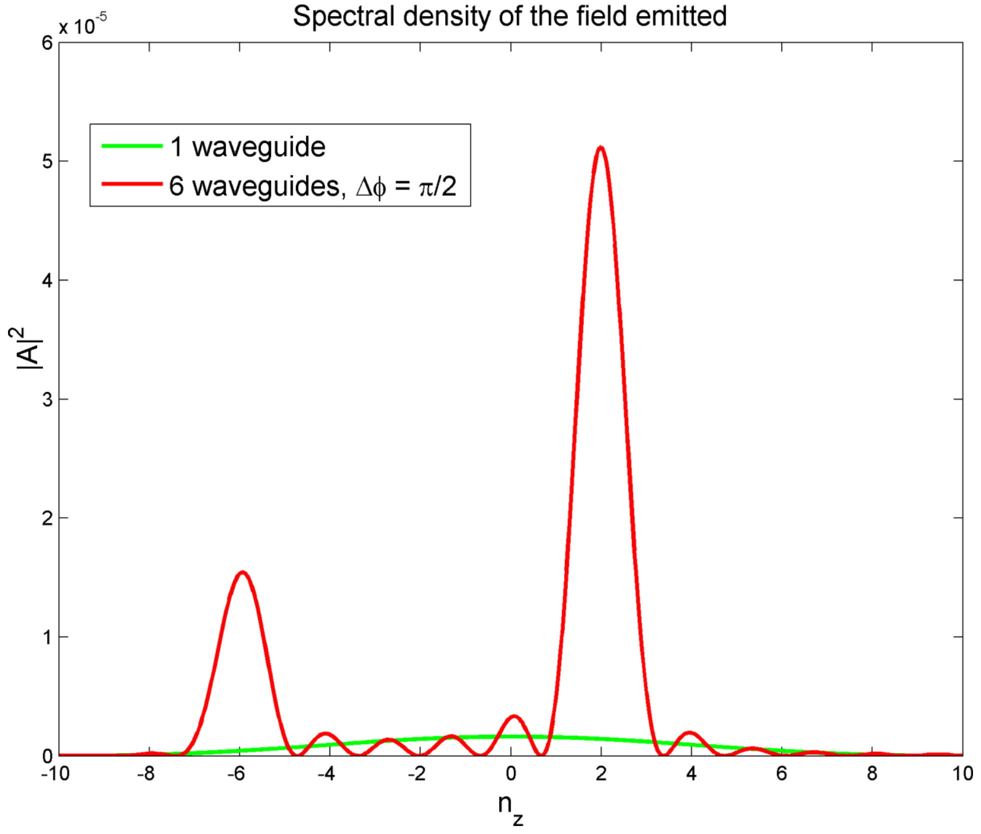

The position of the peaks can be easily retrieved using well known diffraction gratings properties. When N tends to infinity, the set of phased waveguide apertures give birth to grating orders and the separation between the orders is $\Delta k_z = 2\pi / \Delta z$, i.e., $\Delta n_z = 2\pi / (k_0 \, \Delta z)$. The position of the first order ($m = 0$) is linked with the phase shift $\Delta\phi$: $n_z(0) = \Delta\phi / (k_0 \, \Delta_z)$. Consequently, the positions of the peaks are given by

$$n_z(m) = n_z(0) + m \frac{2\pi}{k_0 \, \Delta z} = \frac{\Delta\phi}{k_0 \, \Delta z} + m \frac{2\pi}{k_0 \, \Delta z}$$

In our case, at a frequency of 3.7 GHz, $\Delta z = 10^{-2}$ m, and $\Delta\phi = \pi / 2$, this formula gives the position of the two major peaks: $n_z(0) = 2.03$ and $n_z(-1) = -6.08$.

Picture of a real LHRF antenna

This picture shows a LHRF antenna in the vessel of the Tore Supra tokamak. The dimensions of the array of 6 × 48 waveguides are 580 mm ×580 mm.

The multi-junction antenna that has been used for our measurements simulates one module of 6 waveguides. Both antenna provide an emitted spectrum centered on $k_z = 2k_0$.

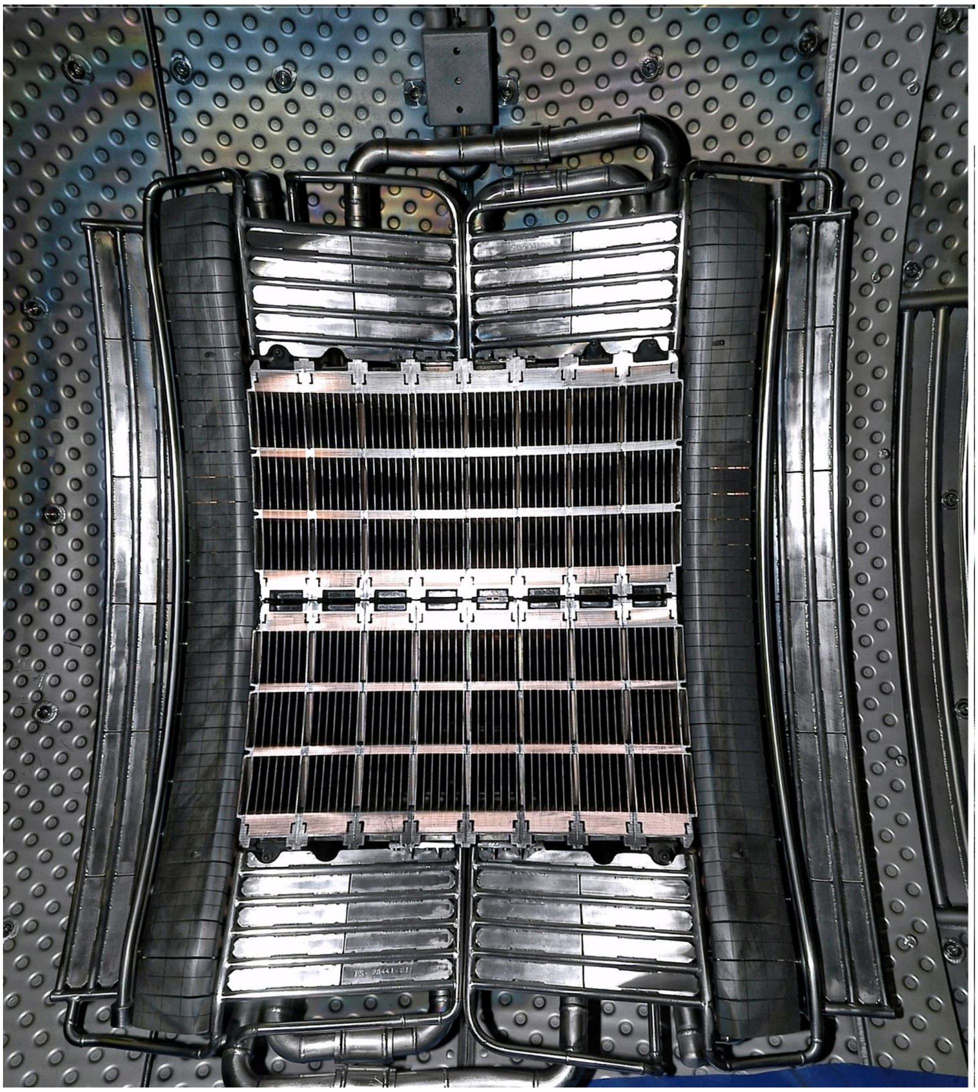

Numerical modeling of the entire multi-junction antenna

The picture below is the complete version of Fig. 3. It shows the entire multi-junction antenna. This antenna is fed from the top. The first section splits into three waveguides, then into six waveguides, with the required phase shifts between adjacent waveguides. The same color scale is used for the three graphs. The vacuum load generates high reflection coefficients and a high standing wave ratio inside the waveguides. The "ideal plasma" and the metamaterial load generate much less standing wave ratio.

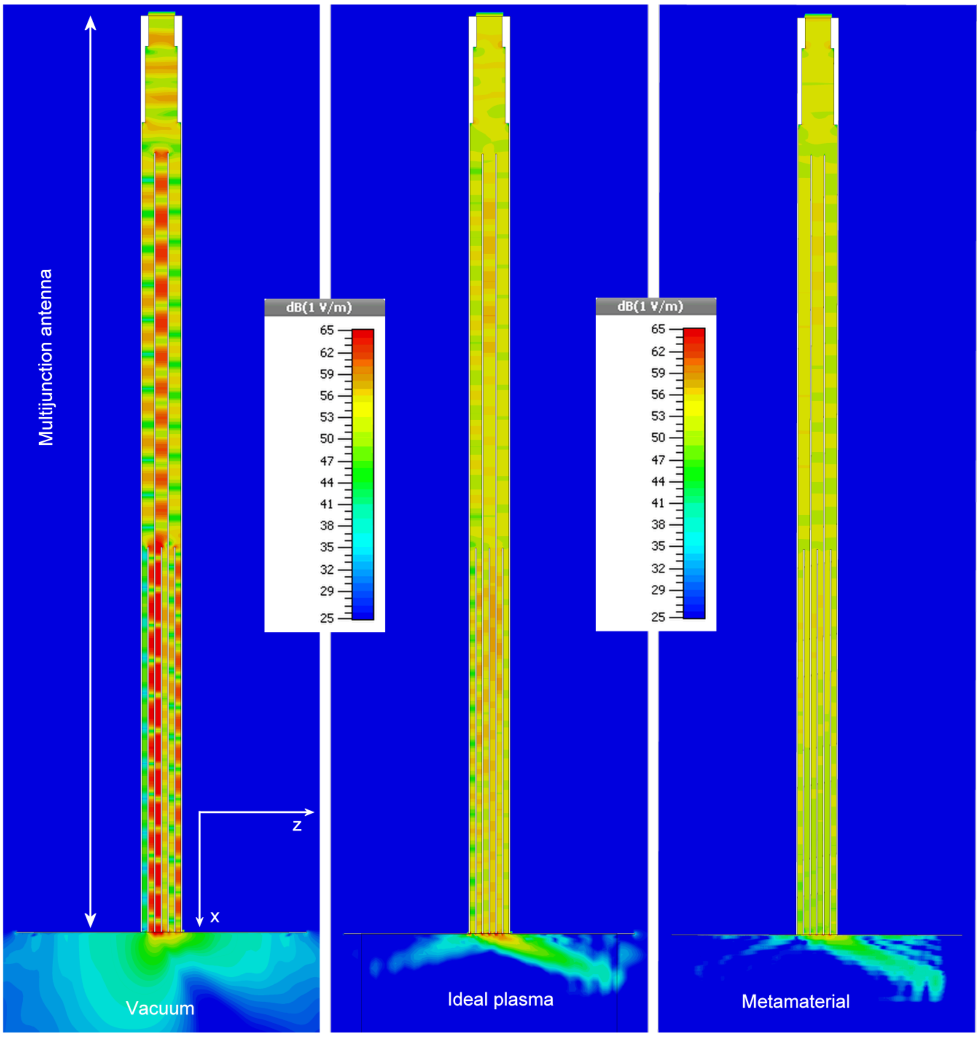

Numerical modeling of the modulus of the electric field at 3.7 GHz. The multi-junction antenna mouth is surrounded by a ground plane (horizontal line on these graphs). The field map is in the middle of the antenna (y = 0 according to figure 1). The multi-junction antenna is loaded with vacuum (left), an ideal plasma with $\varepsilon_{\perp} = 1$ *and* $\varepsilon_{//} = -3$ *(middle), and the fishnet metamaterial (right).*

Bibliography

[1] E. M. Purcell, "Spontaneous emission probabilities at radio frequencies", in, Vol. 69 (1946).

[2] M. Wubs and W. L. Vos, "Förster resonance energy transfer rate in any dielectric nanophotonic medium with weak dispersion", en, New J. Phys. **18** (2016).

[3] V. Weisskopf and E. Wigner, "Berechnung der natürlichen linienbreite auf grund der diracschen lichttheorie", Zeitschrift für Physik A Hadrons and Nuclei **63** (1930).

[4] R. Sprik, B. A. v. Tiggelen, and A. Lagendijk, "Optical emission in periodic dielectrics", en, EPL (Europhysics Letters) **35** (1996).

[5] L. Novotny and B. Hecht, *Principles of nano-optics* (Cambridge university press, 2012).

[6] W. H. Louisell, *Quantum statistical properties of radiation*, Vol. 7 (Wiley New York, 1973).

[7] K. H. Drexhage, "Influence of a dielectric interface on fluorescence decay time", Journal of Luminescence **1–2** (1970).

[8] K. H. Drexhage, "IV interaction of light with monomolecular dye layers", Progress in Optics **12** (1974).

[9] R. G. Hulet, E. S. Hilfer, and D. Kleppner, "Inhibited Spontaneous Emission by a Rydberg Atom", Phys. Rev. Lett. **55** (1985).

[10] X. Zambrana-Puyalto and N. Bonod, "Purcell factor of spherical mie resonators", Phys. Rev. B **91** (2015).

[11] M. S. Eggleston, K. Messer, L. Zhang, E. Yablonovitch, and M. C. Wu, "Optical antenna enhanced spontaneous emission", Proceedings of the National Academy of Sciences **112** (2015).

[12] N. Kumar, "Spontaneous Emission Rate Enhancement Using Optical Antennas", PhD thesis (UC Berkeley, 2013).

[13] E. Yablonovitch, "Inhibited spontaneous emission in solid-state physics and electronics", Phys. Rev. Lett. **58** (1987).

[14] P. Lodahl, A. Floris van Driel, I. S. Nikolaev, A. Irman, K. Overgaag, D. Vanmaekelbergh, and W. L. Vos, "Controlling the dynamics of spontaneous emission from quantum dots by photonic crystals", en, Nature **430** (2004).

[15] S. John and T. Quang, "Localization of Superradiance near a Photonic Band Gap", Phys. Rev. Lett. **74** (1995).

[16] D. Englund, D. Fattal, E. Waks, G. Solomon, B. Zhang, T. Nakaoka, Y. Arakawa, Y. Yamamoto, and J. Vučković, "Controlling the spontaneous emission rate of single quantum dots in a two-dimensional photonic crystal", Phys. Rev. Lett. **95** (2005).

[17] Z. Jacob, I. I. Smolyaninov, and E. E. Narimanov, “Broadband Purcell effect: Radiative decay engineering with metamaterials”, Applied Physics Letters **100** (2012).

[18] E. Schubert, N. Hunt, M Micovic, R. Malik, D. Sivco, A. Cho, G. Zydzik, et al., “Highly efficient light-emitting diodes with microcavities”, Science **265** (1994).

[19] K. Okamoto, I. Niki, A. Shvartser, Y. Narukawa, T. Mukai, and A. Scherer, “Surface-plasmon-enhanced light emitters based on ingan quantum wells”, Nature Materials **3** (2004).

[20] J. B. Khurgin, G. Sun, and R. Soref, “Electroluminescence efficiency enhancement using metal nanoparticles”, Applied Physics Letters **93** (2008).

[21] G. M. Akselrod, C. Argyropoulos, T. B. Hoang, C. Ciracì, C. Fang, J. Huang, D. R. Smith, and M. H. Mikkelsen, “Probing the mechanisms of large purcell enhancement in plasmonic nanoantennas”, Nature Photonics **8** (2014).

[22] T. B. Hoang, G. M. Akselrod, C. Argyropoulos, J. Huang, D. R. Smith, and M. H. Mikkelsen, “Ultrafast spontaneous emission source using plasmonic nanoantennas”, Nature Communications **6** (2015).

[23] M. Arcari, I. Söllner, A. Javadi, S. L. Hansen, S. Mahmoodian, J. Liu, H. Thyrrestrup, E. H. Lee, J. D. Song, S. Stobbe, et al., “Near-unity coupling efficiency of a quantum emitter to a photonic crystal waveguide”, Phys. Rev. Lett. **113** (2014).

[24] M. Pelton, C. Santori, J. Vucković, B. Zhang, G. S. Solomon, J. Plant, and Y. Yamamoto, “Efficient source of single photons: a single quantum dot in a micropost microcavity”, Phys. Rev. Lett. **89** (2002).

[25] C. Santori, M. Pelton, G. Solomon, Y. Dale, and Y. Yamamoto, “Triggered single photons from a quantum dot”, Phys. Rev. Lett. **86** (2001).

[26] M. Born, J. W. Fisher, and D. R. Hartree, *The Mechanics of the Atom* (Frederick Ungar Publishing Co, 1967).

[27] J. P. Dowling, M. O. Scully, and F. DeMartini, “Radiation pattern of a classical dipole in a cavity”, en, Optics Communications **82** (1991).

[28] D. Vion, A Aassime, A. Cottet, P. Joyez, H Pothier, C Urbina, D. Esteve, and M. H. Devoret, “Manipulating the quantum state of an electrical circuit”, Science **296** (2002).

[29] A. Houck, D. Schuster, J. Gambetta, J. Schreier, B. Johnson, J. Chow, L Frunzio, J Majer, M. Devoret, S. Girvin, et al., “Generating single microwave photons in a circuit”, Nature **449** (2007).

[30] Y. Yin, Y. Chen, D. Sank, P. J. J. O’Malley, T. C. White, R. Barends, J. Kelly, E. Lucero, M. Mariantoni, A. Megrant, C. Neill, A. Vainsencher, J. Wenner, A. N. Korotkov, A. N. Cleland, and J. M. Martinis, “Catch and release of microwave photon states”, Phys. Rev. Lett. **110** (2013).

[31] J. P. Dowling, “Spontaneous emission in cavities: How much more classical can you get?”, Found Phys **23** (1993).

[32] J.-J. Greffet, M. Laroche, and F. Marquier, “Impedance of a Nanoantenna and a Single Quantum Emitter”, Phys. Rev. Lett. **105** (2010).

[33] A. E. Krasnok, A. P. Slobozhanyuk, C. R. Simovski, S. A. Tretyakov, A. N. Poddubny, A. E. Miroshnichenko, Y. S. Kivshar, and P. A. Belov, “An antenna model for the Purcell effect”, Scientific Reports **5** (2015).

[34]A. P. Slobozhanyuk, A. N. Poddubny, A. E. Krasnok, and P. A. Belov, “Magnetic purcell factor in wire metamaterials”, Applied Physics Letters **104** (2014).

[35]D. G. Baranov, R. S. Savelev, S. V. Li, A. E. Krasnok, and A. Alù, “Modifying magnetic dipole spontaneous emission with nanophotonic structures”, Laser & Photonics Reviews (2017).

[36]G. Cario and J. Franck, “Über zerlegung von wasserstoffmolekülen durch angeregte quecksilberatome”, Zeitschrift für Physik **11** (1922).

[37]H Beutler and B Josephy, “Resonanz bei stößen zweiter art”, Naturwissenschaften **15** (1927).

[38]J Perrin, “Fluorescence et radiochimie”, Conseil de Chemie, Solvay, 2iém, Paris, Gauthier & Villar, S (1925).

[39]J. Perrin, “Fluorescence et induction moleculaire par resonance”, CR Hebd. Seances Acad. Sci **184** (1927).

[40]F. Perrin, “La fluorescence des solutions-induction moléculaire.–polarisation et durée d’émission.–photochimie”, in Annales de physique, Vol. 10, 12 (EDP Sciences, 1929).

[41]F. Perrin, “Théorie quantique des transferts d’activation entre molécules de même espèce. cas des solutions fluorescentes”, in Annales de physique, Vol. 10, 17 (EDP Sciences, 1932).

[42]F. Perrin, “Interaction entre atomes normal et activé. transferts d’activation. formation d’une molécule activée”, Ann. Institut Poincaré **3** (1933).

[43]A Pietraszewska-Bogiel and T. Gadella, “Fret microscopy: from principle to routine technology in cell biology”, Journal of microscopy **241** (2011).

[44]P. R. Selvin, “The renaissance of fluorescence resonance energy transfer”, Nature Structural & Molecular Biology **7** (2000).

[45]Y. Suzuki, T. Yasunaga, R. Ohkura, T. Wakabayashi, and K. Sutoh, “Swing of the lever arm of a myosin motor at the isomerization and phosphate-release steps”, Nature **396** (1998).

[46]A. A. Deniz, M. Dahan, J. R. Grunwell, T. Ha, A. E. Faulhaber, D. S. Chemla, S. Weiss, and P. G. Schultz, “Single-pair fluorescence resonance energy transfer on freely diffusing molecules: observation of förster distance dependence and subpopulations”, Proceedings of the National Academy of Sciences **96** (1999).

[47]N. Ota, K. Hirano, M. Warashina, A. Andrus, B. Mullah, K. Hatanaka, and K. Taira, “Determination of interactions between structured nucleic acids by fluorescence resonance energy transfer (fret): selection of target sites for functional nucleic acids”, Nucleic acids research **26** (1998).

[48]G. W. Gordon, G. Berry, X. H. Liang, B. Levine, and B. Herman, “Quantitative fluorescence resonance energy transfer measurements using fluorescence microscopy”, Biophysical Journal **74** (1998).

[49]T. W. Gadella, T. M. Jovin, and R. M. Clegg, “Fluorescence lifetime imaging microscopy (flim): spatial resolution of microstructures on the nanosecond time scale”, Biophysical Chemistry **48** (1993).

[50] T. Gadella and T. M. Jovin, “Oligomerization of epidermal growth factor receptors on a431 cells studied by time-resolved fluorescence imaging microscopy. a stereochemical model for tyrosine kinase receptor activation.”, The Journal of cell biology **129** (1995).

[51] P. Andrew and W. L. Barnes, “Förster energy transfer in an optical microcavity”, Science **290** (2000).

[52] T. Nakamura, M. Fujii, K. Imakita, and S. Hayashi, “Modification of energy transfer from si nanocrystals to er 3+ near a au thin film”, Physical Review B **72** (2005).

[53] M. De Dood, J. Knoester, A Tip, and A Polman, “Förster transfer and the local optical density of states in erbium-doped silica”, Physical Review B **71** (2005).

[54] C. Blum, N. Zijlstra, A. Lagendijk, M. Wubs, A. P. Mosk, V. Subramaniam, and W. L. Vos, “Nanophotonic Control of the Förster Resonance Energy Transfer Efficiency”, Phys. Rev. Lett. **109** (2012).

[55] P. Ghenuche, J. de Torres, S. B. Moparthi, V. Grigoriev, and J. Wenger, “Nanophotonic Enhancement of the Förster Resonance Energy-Transfer Rate with Single Nanoapertures”, Nano Lett. **14** (2014).

[56] C. L. Cortes and Z. Jacob, “Super-coulombic atom–atom interactions in hyperbolic media”, Nature Communications **8** (2017).

[57] S.-A. Biehs, V. M. Menon, and G. S. Agarwal, “Long-range dipole-dipole interaction and anomalous Förster energy transfer across a hyperbolic metamaterial”, Phys. Rev. B **93** (2016).

[58] J. Oppenheimer, “Internal conversion in photosynthesis”, Phys. Rev **60** (1941).

[59] R. Hildner, D. Brinks, J. B. Nieder, R. J. Cogdell, and N. F. v. Hulst, “Quantum Coherent Energy Transfer over Varying Pathways in Single Light-Harvesting Complexes”, en, Science **340** (2013).

[60] W. Kuhlbrandt and D. N. Wang, “Three-dimensional structure of plant light-harvesting complex determined by electron crystallography”, Nature **350** (1991).

[61] D. C. Coffey, A. J. Ferguson, N. Kopidakis, and G. Rumbles, “Photovoltaic charge generation in organic semiconductors based on long-range energy transfer”, ACS nano **4** (2010).

[62] J.-S. Huang, T. Goh, X. Li, M. Y. Sfeir, E. A. Bielinski, S. Tomasulo, M. L. Lee, N. Hazari, and A. D. Taylor, “Polymer bulk heterojunction solar cells employing forster resonance energy transfer”, Nature Photonics **7** (2013).

[63] D. J. Farrell and N. J. Ekins-Daukes, “Photovoltaic technology: Relay dye boosts efficiency”, Nature Photonics **3** (2009).

[64] L. Etgar, J. Park, C. Barolo, V. Lesnyak, S. K. Panda, P. Quagliotto, S. G. Hickey, M. K. Nazeeruddin, A. Eychmüller, G. Viscardi, et al., “Enhancing the efficiency of a dye sensitized solar cell due to the energy transfer between cdse quantum dots and a designed squaraine dye”, RSC Advances **2** (2012).

[65] M. D. McGehee, “Paradigm shifts in dye-sensitized solar cells”, Science **334** (2011).

[66] L. Stryer, “Fluorescence energy transfer as a spectroscopic ruler”, Annual Review of Biochemistry **47** (1978).

[67] C. G. Dos Remedios and P. D. Moens, "Fluorescence resonance energy transfer spectroscopy is a reliable" ruler" for measuring structural changes in proteins: dispelling the problem of the unknown orientation factor", Journal of structural biology **115** (1995).

[68] A. Miyawaki, J. Llopis, R. Heim, J. M. McCaffery, et al., "Fluorescent indicators for ca2+ based on green fluorescent proteins and calmodulin", Nature **388** (1997).

[69] S. Weiss, "Measuring conformational dynamics of biomolecules by single molecule fluorescence spectroscopy", Nature Structural & Molecular Biology **7** (2000).

[70] D. R. Smith and D. Schurig, "Electromagnetic wave propagation in media with indefinite permittivity and permeability tensors", Phys. Rev. Lett. **90** (2003).

[71] Z. Jacob, J.-Y. Kim, G. V. Naik, A. Boltasseva, E. E. Narimanov, and V. M. Shalaev, "Engineering photonic density of states using metamaterials", en, Appl. Phys. B **100** (2010).

[72] A. Poddubny, I. Iorsh, P. Belov, and Y. Kivshar, "Hyperbolic metamaterials", en, Nat Photon **7** (2013).

[73] S.-A. Biehs, S. Lang, A. Y. Petrov, M. Eich, and P. Ben-Abdallah, "Blackbody Theory for Hyperbolic Materials", Phys. Rev. Lett. **115** (2015).

[74] A. Tuniz, K. J. Kaltenecker, B. M. Fischer, M. Walther, S. C. Fleming, A. Argyros, and B. T. Kuhlmey, "Metamaterial fibres for subdiffraction imaging and focusing at terahertz frequencies over optically long distances", Nature Communications **4** (2013).

[75] A. Tuniz, D. Ireland, L. Poladian, A. Argyros, C. M. de Sterke, and B. T. Kuhlmey, "Imaging performance of finite uniaxial metamaterials with large anisotropy", Optics Letters **39** (2014).

[76] P. Shekhar, J. Atkinson, and Z. Jacob, "Hyperbolic metamaterials: fundamentals and applications", Nano Convergence **1** (2014).

[77] P. Clemmow, "The theory of electromagnetic waves in a simple anisotropic medium", Proceedings of the Institution of Electrical Engineers **110** (1963).

[78] M. Noginov, Y. A. Barnakov, G Zhu, T Tumkur, H Li, and E. Narimanov, "Bulk photonic metamaterial with hyperbolic dispersion", Applied Physics Letters **94** (2009).

[79] W Dickson, G. Wurtz, P Evans, D O'Connor, R Atkinson, R Pollard, and A. Zayats, "Dielectric-loaded plasmonic nanoantenna arrays: a metamaterial with tuneable optical properties", Phys. Rev. B **76** (2007).

[80] A. Tuniz, R. Lwin, A. Argyros, S. C. Fleming, and B. T. Kuhlmey, "Fabricating metamaterials using the fiber drawing method", Journal of Visualized Experiments: JoVE (2012).

[81] M. S. Habib, A. Tuniz, K. J. Kaltenecker, Q. Chateiller, I. Perrin, S. Atakaramians, S. C. Fleming, A. Argyros, and B. T. Kuhlmey, "Removing image artefacts in wire array metamaterials", Optics Express **24** (2016).

[82] K. J. Kaltenecker, A. Tuniz, S. C. Fleming, A. Argyros, B. T. Kuhlmey, M. Walther, and B. M. Fischer, "Ultrabroadband perfect imaging in terahertz wire media using single-cycle pulses", Optica **3** (2016).

[83] Z. Jacob, L. V. Alekseyev, and E. Narimanov, "Optical hyperlens: far-field imaging beyond the diffraction limit", Optics Express **14** (2006).

[84] P. A. Belov, Y. Zhao, S. Sudhakaran, A. Alomainy, and Y. Hao, “Experimental study of the subwavelength imaging by a wire medium slab”, Applied Physics Letters **89** (2006).

[85] P. Belov, R Marques, S. Maslovski, I. Nefedov, M Silveirinha, C. Simovski, and S. Tretyakov, “Strong spatial dispersion in wire media in the very large wavelength limit”, Phys. Rev. B **67** (2003).

[86] B. Casse, W. Lu, Y. Huang, E Gultepe, L Menon, and S Sridhar, “Super-resolution imaging using a three-dimensional metamaterials nanolens”, Applied Physics Letters **96** (2010).

[87] M. Noginov, H Li, Y. A. Barnakov, D Dryden, G Nataraj, G Zhu, C. Bonner, M Mayy, Z Jacob, and E. Narimanov, “Controlling spontaneous emission with metamaterials”, Optics Letters **35** (2010).

[88] D. Lu, J. J. Kan, E. E. Fullerton, and Z. Liu, “Enhancing spontaneous emission rates of molecules using nanopatterned multilayer hyperbolic metamaterials”, Nature Nanotechnology **9** (2014).

[89] Y. C. Jun, R. Pala, and M. L. Brongersma, “Strong modification of quantum dot spontaneous emission via gap plasmon coupling in metal nanoslits”, J. Phys. Chem. C **114** (2010).

[90] A. P. Slobozhanyuk, P. Ginzburg, D. A. Powell, I. Iorsh, A. S. Shalin, P. Segovia, A. V. Krasavin, G. A. Wurtz, V. A. Podolskiy, P. A. Belov, and A. V. Zayats, “Purcell effect in hyperbolic metamaterial resonators”, Phys. Rev. B **92** (2015).

[91] S. Kosulnikov, D. Filonov, S. Glybovski, P. Belov, S. Tretyakov, and C. Simovski, “Wire-Medium Hyperlens for Enhancing Radiation From Subwavelength Dipole Sources”, IEEE Transactions on Antennas and Propagation **63** (2015).

[92] K. Rustomji, R. Abdeddaim, C. M. de Sterke, B. Kuhlmey, and S. Enoch, “Measurement and simulation of the polarization-dependent purcell factor in a microwave fishnet metamaterial”, Phys. Rev. B **95** (2017).

[93] R. R. Chance, A. Prock, and R. Silbey, “Molecular fluorescence and energy transfer near interfaces”, Adv. Chem. Phys **37** (1978).

[94] J. D. Jackson, *Classical electrodynamics* (John Wiley & Sons, 2007).

[95] C.-T. Tai, *Dyadic green functions in electromagnetic theory* (Institute of Electrical & Electronics Engineers (IEEE), 1994).

[96] R. J. Glauber and M Lewenstein, “Quantum optics of dielectric media”, Phys. Rev. A **43** (1991).

[97] C. Sauvan, J. P. Hugonin, I. S. Maksymov, and P. Lalanne, “Theory of the Spontaneous Optical Emission of Nanosize Photonic and Plasmon Resonators”, Phys. Rev. Lett. **110** (2013).

[98] J. Plemelj, “Ein ergänzungssatz zur cauchyschen integraldarstellung analytischer funktionen, randwerte betreffend”, Monatshefte für Mathematik **19** (1908).

[99] E. T. Jaynes and F. W. Cummings, “Comparison of quantum and semiclassical radiation theories with application to the beam maser”, Proceedings of the IEEE **51** (1963).

[100] R. Loudon, *The quantum theory of light* (OUP Oxford, 2000).

[101] C. Cohen-Tannoudji, J. Dupont-Roc, G. Grynberg, and P. Thickstun, *Atom-photon interactions: basic processes and applications* (Wiley Online Library, 1992).

[102] N. Vats, S. John, and K. Busch, “Theory of fluorescence in photonic crystals”, Phys. Rev. A **65** (2002).

[103] D. Fussell, R. McPhedran, and C. M. de Sterke, “Three-dimensional green’s tensor, local density of states, and spontaneous emission in finite two-dimensional photonic crystals composed of cylinders”, Phys. Rev. E **70** (2004).

[104] C.-A. Guérin, B. Gralak, and A. Tip, “Singularity of the dyadic green’s function for heterogeneous dielectrics”, Phys. Rev. E **75** (2007).

[105] J. Wylie and J. Sipe, “Quantum electrodynamics near an interface. ii”, Phys. Rev. A **32** (1985).

[106] G. S. Agarwal, “Quantum electrodynamics in the presence of dielectrics and conductors. III. Relations among one-photon transition probabilities in stationary and nonstationary fields, density of states, the field-correlation functions, and surface-dependent response functions”, Phys. Rev. A **11** (1975).

[107] S. Scheel, L Knöll, and D.-G. Welsch, “Spontaneous decay of an excited atom in an absorbing dielectric”, Phys. Rev. A **60** (1999).

[108] R. Carminati, J.-J. Greffet, C. Henkel, and J.-M. Vigoureux, “Radiative and non-radiative decay of a single molecule close to a metallic nanoparticle”, Optics Communications **261** (2006).

[109] W. Demtröder, *Atoms, Molecules and Photons* (Springer Berlin Heidelberg, 2010).

[110] J. G. Van Bladel, *Electromagnetic fields*, edited by D. G. Dudley (John Wiley & Sons, Inc., 2007).

[111] C. A. Balanis, *Antenna theory: analysis and design*, 2nd ed. (John Wiley & Sons, 1997).

[112] S. A. Tretyakov, S. Maslovski, and P. A. Belov, “An analytical model of metamaterials based on loaded wire dipoles”, IEEE Transactions on Antennas and Propagation **51** (2003).

[113] K. Joulain, R. Carminati, J.-P. Mulet, and J.-J. Greffet, “Definition and measurement of the local density of electromagnetic states close to an interface”, Phys. Rev. B **68** (2003).

[114] R. Carminati, A. Cazé, D. Cao, F. Peragut, V. Krachmalnicoff, R. Pierrat, and Y. De Wilde, “Electromagnetic density of states in complex plasmonic systems”, Surface Science Reports **70** (2015).

[115] R. J. Collier and A. D. Skinner, *Microwave Measurements* (IET, 2007).

[116] V. Teppati, A. Ferrero, and M. Sayed, *Modern RF and microwave measurement techniques* (Cambridge University Press, 2013).

[117] D. A. Frickey, “Conversions between S, Z, Y, H, ABCD, and T parameters which are valid for complex source and load impedances”, IEEE Transactions on microwave theory and techniques **42** (1994).

[118] S. Enoch, G. Tayeb, P. Sabouroux, N. Guérin, and P. Vincent, “A Metamaterial for Directive Emission”, Phys. Rev. Lett. **89** (2002).

[119] J. B. Pendry, A. J. Holden, D. J. Robbins, and W. J. Stewart, “Low frequency plasmons in thin-wire structures”, en, J. Phys.: Condens. Matter **10** (1998).

[120] G. Guida, D. Maystre, G. Tayeb, and P. Vincent, “Mean-field theory of two-dimensional metallic photonic crystals”, en, Journal of the Optical Society of America B **15** (1998).

[121] D. Felbacq and G. Bouchitté, “Homogenization of a set of parallel fibres”, Waves in Random Media **7** (1997).

[122] C. L. Cortes, W Newman, S Molesky, and Z Jacob, “Quantum nanophotonics using hyperbolic metamaterials”, Journal of Optics **14** (2012).

[123] CST MICROWAVE STUDIO, www.cst.com (2015).

[124] J. E. Storer, “Impedance of thin-wire loop antennas”, AIEE Trans. **75** (1956).

[125] I. S. Nikolaev, W. L. Vos, and A. F. Koenderink, “Accurate calculation of the local density of optical states in inverse-opal photonic crystals”, Journal of the Optical Society of America B **26** (2009).

[126] T. Förster, “Zwischenmolekulare energiewanderung und fluoreszenz”, Annalen der Physik **437** (1948).

[127] D. L. Andrews, “A unified theory of radiative and radiationless molecular energy transfer”, Chemical Physics **135** (1989).

[128] G. S. Agarwal and S. D. Gupta, “Microcavity-induced modification of the dipole-dipole interaction”, Phys. Rev. A **57** (1998).

[129] S. John and T. Quang, “Photon-hopping conduction and collectively induced transparency in a photonic band gap”, Phys. Rev. A **52** (1995).

[130] E. V. Goldstein, P. Pax, and P. Meystre, “Dipole-dipole interaction in three-dimensional optical lattices”, Phys. Rev. A **53** (1996).

[131] G. V. Varada and G. S. Agarwal, “Two-photon resonance induced by the dipole-dipole interaction”, Phys. Rev. A **45** (1992).

[132] H. T. Dung, L. Knöll, and D.-G. Welsch, “Resonant dipole-dipole interaction in the presence of dispersing and absorbing surroundings”, Phys. Rev. A **66** (2002).

[133] H. T. Dung, L. Knöll, and D.-G. Welsch, “Intermolecular energy transfer in the presence of dispersing and absorbing media”, Phys. Rev. A **65** (2002).

[134] B. H. Bransden and C. J. Joachain, *Physics of atoms and molecules* (Pearson Education India, 2003).

[135] W. Demtröder, *Atoms, Molecules and Photons* (Springer Berlin Heidelberg, 2010).

[136] S. Tretyakov, “Maximizing Absorption and Scattering by Dipole Particles”, Plasmonics **9** (2014).

[137] T. Kobayashi, Q. Zheng, and T. Sekiguchi, “Resonance transfer of excitation for molecules between mirrors”, en, Physics Letters A **199** (1995).

[138] T. Kobayashi, Q. Zheng, and T. Sekiguchi, “Resonant dipole-dipole interaction in a cavity”, Phys. Rev. A **52** (1995).

[139] M. Pelton, “Modified spontaneous emission in nanophotonic structures”, Nature Photonics **9** (2015).

[140] F. Marquier and J.-J. Greffet, “Impedance of a nanoantenna”, in *Optical antennas* (2013).

[141] J.-K. Hwang, “Spontaneous emission rate of an electric dipole in a general microcavity”, Phys. Rev. B **60** (1999).